

Clemson University

**TigerPrints**

---

All Dissertations

Dissertations

---

8-2022

## Development of Plasmonic and X-Ray Luminescence Nanoparticles for Bioimaging and Sensing Applications

Meenakshi Ranasinghe

Clemson University, [mrnasi@clemson.edu](mailto:mrnasi@clemson.edu)

Follow this and additional works at: [https://tigerprints.clemson.edu/all\\_dissertations](https://tigerprints.clemson.edu/all_dissertations)



Part of the [Analytical Chemistry Commons](#)

---

### Recommended Citation

Ranasinghe, Meenakshi, "Development of Plasmonic and X-Ray Luminescence Nanoparticles for Bioimaging and Sensing Applications" (2022). *All Dissertations*. 3095.

[https://tigerprints.clemson.edu/all\\_dissertations/3095](https://tigerprints.clemson.edu/all_dissertations/3095)

This Dissertation is brought to you for free and open access by the Dissertations at TigerPrints. It has been accepted for inclusion in All Dissertations by an authorized administrator of TigerPrints. For more information, please contact [kokeefe@clemson.edu](mailto:kokeefe@clemson.edu).

DEVELOPMENT OF PLASMONIC AND X-RAY LUMINESCENCE  
NANOPARTICLES FOR BIOIMAGING AND SENSING APPLICATIONS

---

A Dissertation  
Presented to  
the Graduate School of  
Clemson University

---

In Partial Fulfillment  
of the Requirements for the Degree  
Doctor of Philosophy  
Chemistry

---

by  
Meenakshi Ranasinghe  
August 2022

---

Accepted by:  
Prof. Jeffrey N. Anker, Committee Chair  
Dr. George Chumanov  
Dr. Jason D. McNeill  
Dr. Joseph W. Kolis

## ABSTRACT

This dissertation discusses the development of plasmonic and X-ray luminescence nanoparticles ( $\sim 100$  nm) to use in bioimaging and sensing applications. The nanoparticles have interesting optical properties compared to their atomic levels and bulk materials. The optical properties of nanomaterials can be controlled by changing size, shape, crystal structure, etc. Also, they have a large surface area that can be functionalized with biomolecules. Therefore, the optical properties and biofunctionalized nanomaterials are useful in biomedical applications such as targeted drug delivery, bioimaging, and sensing. The overall theme is to use nanoparticles with interesting optical properties compared to their atomic levels and bulk materials to understand and control size/shape-dependent optical properties and crystallinity. Here, we discuss nanomaterials' optical properties and biofunctionalization in three sections, 1) size/shape-dependent optical properties of plasmonic nanoparticles, which we develop a simple and robust mechanical approach to prepare plasmonic nanoparticle arrays, 2) X-ray optical luminescence of X-ray luminescence nanoparticles which depends on crystal defects and amount of dopants by synthesizing them and enhancing their intensity to use them in high-resolution imaging, 3) biofunctionalization of gold and X-ray luminescence nanoparticles to develop immunoassays.

Chapter two describes the development of a simple, mechanical approach to preparing plasmonic nanoparticle arrays and transferring them onto a thin film. Plasmonic nanoparticles can absorb and scatter visible range light depending on their

size, shape, and environment, and unlike fluorescence dyes, they do not photo-bleach. Plasmonic nanoparticles and array of nanoparticles have many applications including in bioimaging and sensing. The current methods to develop nanoparticle arrays and transfer them onto thin films are complex, time-consuming, and expensive. Here, we report a simple technique to generate patterns of gold and silver nanoparticles with controlled shape and shape-dependent optical properties. The pressure was applied to nanoparticles on a glass slide to convert nanospheres (diameter  $\sim 90$  nm) to nanodiscs (diameter  $\sim 180$  nm). Metal stamps and glucose deposits were placed on nanoparticles before applying pressure to generate patterns. The change in nanoparticle shape causes their localized surface plasmon resonance wavelength to red-shift. Also, we developed a method to remove undeformed nanoparticles using scotch tape and transform nanoparticle patterns into a flexible polymer film.

Like plasmonic nanoparticles, X-ray luminescence nanophosphors can be used as an optical contrast agent in biomedical imaging and optical biosensors. They generate visible light through tissue when irradiated with X-rays. However, the sensitivity of these applications depends on the intensity of emitted visible light, and it is important to investigate methods to enhance its intensity. Herein, we describe the synthesis of X-ray scintillating  $\text{NaGdF}_4\text{:Eu}$  and  $\text{Tb}$  nanophosphors via co-precipitate and hydrothermal methods, enhancing X-ray excited optical luminescence. The brightest particles were obtained using hydrothermal synthesis, and thermal annealing enhanced X-ray luminescence intensity. However, annealing above  $600^\circ\text{C}$  changes the chemical structure to  $\text{NaGd}_9\text{Si}_6\text{O}_{26}\text{:Eu}$ , which results in a shift in the X-ray luminescence spectra.



Further, we demonstrated that the particles generate light through tissue and can be selectively excited using a focused X-ray source for imaging and spectroscopy.

The fourth chapter brings plasmonic and X-ray luminescence particles together to develop immunoassays. Here, we describe a design and development of a gold nanoparticles-based lateral flow assay (LFA) to detect SARS-CoV-2 antibodies in human saliva and a proof of concept to develop an immunoassay using gold nanoparticles and X-ray luminescence nanoparticles. Gold and X-ray luminescence particles were functionalized with receptor binding domain protein and human anti-spike IgG, respectively. Our preliminary studies show the ability to develop the LFA to detect SARS-CoV-2 antibodies in human saliva, an immunoassay using RBD functionalized gold nanoparticles, and anti-spike IgG functionalized Gadolinium oxysulfide microparticles. The X-ray luminescence decreases by a factor of 1.8 due to light absorption when attaching gold nanoparticles to Gadolinium oxysulfide microparticles. This can be developed as an implantable immunoassay to quantify biomarkers *in vivo* locally and continuously.

Chapter five includes a separate study that is not based on nanoparticles-based bioimaging and sensing. However, it discusses a behavioral analysis to discover and understand the X-ray stimulated behavior of *Caenorhabditis elegans*.

Chapter six provides a conclusion and discusses possible future work for each chapter.

## DEDICATION

I dedicate this work to the free education in Sri Lanka, my parents, Sarath Ranasinghe and Ranjanie Abeyrathne, my husband Mohan M. Abeysekera, extended family, and friends for their unconditional love and support throughout this journey.

## ACKNOWLEDGMENTS

I would like to acknowledge the guidance, support, and patience of my Ph.D. advisor, Dr. Jeffrey Anker, throughout my Ph.D. journey. He has always been there to answer my questions, listen to my concerns and help me learn and communicate scientific thoughts. I wish to thank all the people whose assistance was a milestone in completing this project, especially my Ph.D. committee, Drs. George Chumanov, Joseph Kolis, and Jason D. McNeill.

This research would not have been possible without the collaborative support of Drs. Appara Rao, Dept. of Physics, Delphine Dean, Congyu Peng, Dept. of Bioengineering, Clemson University, Mark Bolding University of Alabama at Birmingham, and other group members of Anker lab, and the insightful conversations that we had during the project meetings overall these years. Specifically, Fathima Ameer trained me on the plasmonic nanoparticle deformation project. The *C. elegans* experiments were performed with Kellin Cannon from the University of Alabama at Birmingham, Dr. Congyu Peng, Dept of IIT Ctr Medical Devices/Sensor, for advising and ordering chemicals for developing LFA.

I wish to show my gratitude to the wonderful staff at Clemson Light Imaging Facility (CLIF) and the electron microscope facility (EM Lab) for training me in many light and electron microscopes, Rakesh Sachdeva for training me on several instruments in the chemistry department, Colin McMillen for helping me with powder-XRD, and the physics and bioengineering departments for allowing me to use their instruments.

I wish to acknowledge my family's support and great love; my hard-working parents who strived to provide me and my brother with the best educational opportunities, my brother (Nimesha Ranasinghe) and his family for taking me to visit beautiful places in the USA, my cousins (Prabha Ranasinghe and Sidath Wijesinghe) who came to Clemson University before me helped me to settle in a foreign land, My husband, who always thinks my happiness before his and gives me enormous support throughout this journey.

These research projects were based upon work supported by NIBIB of the National Institutes of Health under award number 1R21EB019709-01A1 and NIGMS of the National Institutes of Health under award number 5P20GM103444-07 outreach activities based on the results were supported by NSF CHE1255535, NSF Track II EPSCoR OIA-1632881 for the synthesis by the NIH NIBIB R01EB026646 for the X-ray luminescence imaging and P30 GM131959 for the electron microscopy, South Carolina COVID fund for lateral flow assay project.

## TABLE OF CONTENTS

	Page
ABSTRACT.....	ii
DEDICATION.....	v
ACKNOWLEDGMENTS.....	vi
TABLE OF CONTENTS.....	viii
LIST OF FIGURES.....	xi
 CHAPTER ONE	
INTRODUCTION.....	1
1.1. Plasmonic Nanoparticles for Imaging and Sensing Applications.....	3
1.2. X-ray Luminescence Nanoparticles for Imaging and Sensing Applications ....	7
1.3. Applications of Plasmonic and X-ray Luminescence particles: Developing immunosensors .....	15
1.4. Radiation-Induced Behavior of <i>Caenorhabditis elegans</i> .....	16
1.5. List of Publications .....	18
1.6. References.....	18
 CHAPTER TWO	
IMPRESSIVELY PRINTING PATTERNS OF GOLD AND SILVER	
NANOPARTICLES .....	29
2.1. Abstract.....	29
2.2. Introduction.....	30
2.3. Methods.....	32
2.3.1. Methods and Instrumentation .....	32
2.3.2. Poly(4-vinylpyridine) functionalization of glass substrate .....	33
2.3.3. AuNPs and AgNPs Synthesis .....	34
2.3.4. Deposition of nanoparticles on PVP functionalized ITO glass slides .....	35
2.3.5. Mechanical deformation of nanoparticles.....	36
2.3.6. Dark field optical imaging .....	36
2.3.7. Hyperspectral darkfield microscopy .....	37
2.3.8. Atomic force microscopy (AFM) .....	37
2.4. Results and Discussion .....	38

2.4.1.	Manual and force-controlled nanoparticle deformation .....	38
2.4.2.	Stamping deformation pattern.....	47
2.5.	Conclusions.....	62
2.6.	Acknowledgment .....	62
2.7.	References.....	63
CHAPTER THREE		

## X-RAY EXCITED LUMINESCENCE SPECTROSCOPY AND IMAGING WITH

NaGdF <sub>4</sub> :Eu AND Tb.....	71
3.1. Abstract.....	71
3.2. Introduction.....	72
3.3. Methods.....	74
3.3.1. NaGdF <sub>4</sub> :Eu and NaGdF <sub>4</sub> :Tb nanoparticle synthesis.....	74
3.3.2. Silica coating NaGdF <sub>4</sub> :Eu and Tb nanoparticles .....	76
3.3.3. Annealing NaGdF <sub>4</sub> :Eu nanoparticles.....	76
3.3.4. Functionalization of NaGdF <sub>4</sub> :Eu@SiO <sub>2</sub> with biotin.....	76
3.3.5. Dark field optical imaging capillaries filled with NaGdF <sub>4</sub> :Eu through tissue 77	
3.3.6. MR imaging of NaGdF <sub>4</sub> :Eu and Tb.....	78
3.3.7. Transmission electron microscopy .....	79
3.3.8. Powder X-ray diffraction (XRD).....	79
3.3.9. X-ray excited optical luminescence (XEOL) spectroscopy.....	79
3.3.10. ICP-OES metal analysis.....	80
3.3.11. Thermal analysis: TGA/DSC .....	80
3.4. Results and Discussion .....	80
3.4.1. NaGdF <sub>4</sub> :Eu and NaGdF <sub>4</sub> :Tb nanoparticle synthesis.....	81
3.4.2. Inductive coupled plasma-optical emission spectroscopy (ICP-OES) metal analysis 87	
3.4.3. Silica-coating NaGdF <sub>4</sub> :Eu and Tb nanophosphors .....	89
3.4.4. Thermal analysis.....	90
3.4.5. Annealing NaGdF <sub>4</sub> :Eu nanophosphors.....	92
3.4.6. Biotin functionalized NaGdF <sub>4</sub> :Eu@SiO <sub>2</sub> .....	96
3.4.7. X-ray excited optical luminescence spectroscopy and imaging of capillaries filled with NaGdF <sub>4</sub> :Eu through tissue.....	97
3.4.8. MR imaging of NaGdF <sub>4</sub> :Eu and Tb.....	101
3.5. Conclusions.....	103
3.6. Acknowledgments.....	103
3.7. References.....	104
CHAPTER FOUR	

## FUNCTIONALIZING RADIODENSE PARTICLES AND DEVELOPING

IMMUNOASSAYS TO DETECT SARS-CoV-2 ANTIBODIES.....	113
4.1. Abstract.....	113
4.2. Introduction.....	114
4.3. Methods.....	116
4.3.1. Designing and developing an LFA to detect SARS-CoV-2 antibodies (Proof of concept) .....	116
4.3.2. Functionalizing gold NPs with SARS-CoV-2 receptor-binding domain (RBD) protein .....	118
4.3.3. Functionalizing Eu doped gadolinium oxysulfide (Gd <sub>2</sub> O <sub>2</sub> S:Eu/ GOS:Eu, 2.5 µm) microparticles with human anti-spike IgG antibodies .....	119
4.3.4. ray excited optical luminescence (XEOL) spectroscopy .....	120
4.4. Results and Discussion .....	121
4.4.1. Designing and developing an LFA to detect SARS-CoV-2 antibodies (Proof of concept) .....	121
4.4.2. Functionalizing gold NPs with SARS-CoV-2 receptor-binding domain (RBD) protein .....	124
4.4.3. Developing an x-ray luminescence immunoassay to detect SARS-CoV-2 antibodies (Proof of concept).....	126
4.5. Conclusions.....	127
4.6. Acknowledgments.....	128
4.7. References.....	128
CHAPTER FIVE	

## X-RAY STIMULATED EGG EJECTION OF *C. ELEGANS* ..... 134

5.1. Abstract.....	134
5.2. Introduction.....	135
5.3. Methods.....	139
5.3.1. Growing, maintaining, and preparing <i>C. elegans</i> plates in the laboratory.....	139
5.3.2. Experiment setup .....	141
5.3.3. Egg ejection experiments.....	142
5.4. Results and discussion .....	143
5.5. Conclusions.....	147
5.6. Acknowledgments.....	147
5.7. Reference .....	147

## CHAPTER SIX

## SUMMARY AND FUTURE WORK..... 150

6.1. Introduction.....	150
6.2. Impressively printing patterns of gold and silver nanoparticles .....	151

6.3.	X-ray excited luminescence spectroscopy and imaging with NaGdF <sub>4</sub> :Eu and Tb	154
6.4.	Functionalizing radiodense particles and developing immunoassays to detect SARS-CoV-2 antibodies.....	160
6.5.	Conclusion .....	161
APPENDICES.....		164

## LIST OF FIGURES

Figure	Page
Figure 1. 1: Size comparison of nanoparticles of interest to some biological components. Modified from ref. 1. ....	2
Figure 1. 2: (A) Schematic diagram illustrating a localized surface plasmon resonance. (B) real and imaginary parts of the dielectric function of silver as a function of wavelength. Taken with permission of ref. 6 (C) Calculated extinction spectra of gold nanorods with varying aspect ratios. Taken with permission of ref. 3 .....	5
Figure 2. 1: Characterization of (A) 97 nm diameter AgNPs, (B) 72 nm diameter AuNPs (B), and (C) 94 nm diameter AuNPs using UV-vis spectroscopy (A1, B1, and C1), and scanning electron microscopy (A2, B2, and C2). The scale bar in each SEM image is 300 nm. Taken with permission of ref 1. ....	39
Figure 2. 2: (A) Photograph of AuNPs on a glass slide being manually deformed with a glass stir rod. A glass substrate coated with AuNPs is placed on a slide holder fixed to the optical bench to hold it steady, and a glass stirring rod rolls over the AuNPs to flatten them. (B) A rolling pin, comprising of a ¼" glass tube with a metal pin through it, is held in a mechanical test system fixture and rolled over particles deposited on a PVP functionalized ITO glass substrate. (C) Dark field microscopy image showing both undeformed AuNP (bottom, green) and deformed AuNPs (top, red) on a PVP functionalized glass substrate. 4X zoom in images of (D) deformed and (E) undeformed AuNPs. Representative dark field single AuNP scattering spectra from (F) deformed and (G) undeformed AuNPs. The squared AuNPs in figures (D) and (E) produced the spectra shown in (F) and (G), respectively. Scale bar is 20 µm. Spectra are offset for clarity. Taken with permission of ref 1. ....	40
Figure 2. 3: Photograph showing the deformation technique employed in this study. The rolling pin was placed on one end of the slide to begin with. A mechanical force was applied by the ESM 303 as the glass tube was rolled over the length of the glass substrate	



10 times. The applied force was varied from 0 to 50 N, and a constant rolling speed of 500  $\mu\text{m/s}$  was used in each experiment. The glass tube was cleaned several times using acetone and distilled water prior to use. Taken with permission of ref 1. .... 41

Figure 2. 4: Dark field microscope image showing both deformed (top-red) and undeformed (bottom-blue) regions of Ag NPs on a glass/ITO slide. Taken with permission of ref 1. .... 42

Figure 2. 5: (Left) SEM images showing effect of applied load (A1) 0 N, (B1) 30 N, and (C1) 50 N on deformation of AuNPs. All images have the same magnification (Scale bar is 300 nm). Histograms on the right of each SEM image show particle diameter distributions for (A2) undeformed and (B2, C2) deformed AuNPs. The sample preparation and SEM imaging procedure are described in the Experimental Section. The inset numbers show estimated mean diameter and uncertainty from a Gaussian fit. (D1) Average dark field single nanoparticle scattering spectra of one hundred undeformed and deformed AuNPs as a function of applied load (0, 1, 3, 5, 8, 10, 30, 50 N). The spectra are scaled to the same maximum intensity. (D2) Experimental data on the evolution of LSPR peak position, before and after deformation, as a function of applied load. Figure 2.6 shows a comparison with our previous AgNP study. Taken with permission of ref 1. .... 44

Figure 2. 6: Average dark field single nanoparticle scattering spectra of un-deformed and deformed (A) AgNPs and (C) AuNPs as a function of applied load. The spectra are scaled to the same maximum intensity. Experimental data on the evolution of LSPR peak position, before and after deformation of (B) AgNPs and (D) AuNPs as a function of applied load. Panels A and B are adapted from reference.<sup>31</sup> Taken with permission of ref 1. .... 45

Figure 2. 7: (A) Dark field microscope image of patterned/deformed Ag NPs by placing TEM grid on NPs and mechanically pressing them. (B) Dark field microscope images (Zoomed in) of location 1,2 and 3 by placing polarizer at 0 (zero) and 90 degrees of angle. NPs marked using yellow color boxes show polarization dependent scattering properties. Some of the NPs at location 3 shows shape and orientation dependent scattering. Taken with permission of ref 1. .... 46

Figure 2. 8: Photographs of glass slide coated with AgNPs, with stamp patterns formed by manually pressing either at TEM grid or VACCO grid onto the slide with a rolling pin. The blue color is a result of light scattering by the undeformed particles, and the red regions represent scattered light by the deformed particles. The stamping and imaging were performed by volunteers during the Upstate EMAG!NE public education outreach event in Greenville, South Carolina. The vertical streaks are the scratched marks caused by the rolling rod on the microscope slide. Taken with permission of ref 1. .... 48

Figure 2. 9: Patterning with TEM grid pattern. (i-iii) Schematic illustration of the principle of the patterning technique. The patterning technique involves three steps: (i) Deposition of nanoparticles on PVP functionalized glass slides, (ii) Patterning of selected nanoparticles via mechanical deformation using a TEM grid as a stamp (not drawn to

scale), and (iii) Lift-off of TEM grid from sample surface, which leaves deformed nanoparticles in shape of the TEM-grid pattern. Images of Au (middle row) and Ag (bottom row) NPs deformed under a copper TEM-grid pattern. (A1, B1) Hyperspectral dark field images and (A2, A3, B2, B3) SEM images. Both undeformed and deformed regions were marked using a dashed line. (A4, B4) Representative average dark field scattering spectrum from un-deformed and deformed Au and Ag NPs regions, respectively. Taken with permission of ref 1. .... 51

Figure 2. 10: (A) SEM image showing both deformed (right to dotted line) and undeformed (left to dotted line) regions of Ag NPs on an ITO slide. The number of particles per unit area is unchanged before and after deformation ( $\sim 10$  particles/ $\mu\text{m}^2$ ). (B1-B2) AFM images of AgNPs deformed under a copper TEM grid pattern. Contact AFM was used to map the profiles of patterned AgNPs on PVP-functionalized ITO glass substrates by applying 50 N load. Partly deformed individual Ag nanoparticles. (C1) 2D and (C2) 3D AFM images showing boundary between deformed and undeformed AgNPs. (C3) Zoom in image showing a single nanoparticle that was partly deformed. Taken with permission of ref 1. .... 52

Figure 2. 11: Histograms of the average AgNPs height (A) before and (B) after deforming using TEM grid. All AFM height measurements were obtained based on more than at least 150 particles. Taken with permission of ref 1. .... 53

Figure 2. 12: (A1) Optical profiler image of VACCO grid showing parallel streaks, (A2) zoom in image of (A1). (A3) 3D AFM image showing surface roughness (ridges and grooves) of VACCO grid. Dark field microscope images of deformed regions of (B1) AuNPs and (C1) AgNPs. Zoom in images of (B2) AuNPs and (C2) AgNPs from B1 and C1 showing printed parallel streaks and surface roughness (green (B2) and blue (C2) areas in deformed regions are due to grooves of VACCO grid). 3D AFM images of (B2) AuNPs and (C2) AgNPs deformed using the hexagonal patterned VACCO grid. Taken with permission of ref 1. .... 54

Figure 2. 13: High resolution AFM images in (A) 2D and (B) 3D. Areas within the white circles show the deformed nanoparticles caused by the ridges in the hexagonal stamp (see Figure 4). Taken with permission of ref 1. .... 55

Figure 2. 14: (A) Hyperspectral dark field image showing protected region of Ag NPs around the glucose deposit and deformed region away from the deposit. (B) Dark field single nanoparticle scattering spectra of undeformed (blue region), partially deformed (green and yellow regions) and deformed (red region) NPs corresponding to image (A). (C) Scanning electron microscopic image of patterned Ag NPs. .... 56

Figure 2. 15: i-iii, Schematic illustration of the removal of undeformed nanoparticles using adhesive tape. (i) Mechanically deformed nanoparticles; (ii) applying adhesive tape on the patterned glass substrate to peel-off undeformed NPs; (iii) pattern of deformed nanoparticles left on the glass slide. (A1-A3) Hyperspectral dark field images of AuNPs deformed with a TEM grid; (B1-B3) hyperspectral dark field images of AgNPs deformed with a TEM grid. (A1, B1) Pattern before removing undeformed particles; (A2, B2)

pattern after removal of undeformed NPs with adhesive tape; (A3, B3) 40X zoom in images of patterned AuNPs and Ag NPs from A2 and C3. Taken with permission of ref 1. .... 57

Figure 2. 16: Transferring AgNPs to flexible polymer films. (A1) First Contact™ clear polymer polymerized into a thin-film on a glass slide. (A2) Peeling off, and (A3) stretching of the clear thin-film. Dark field microscope images (100 x oil, immersion) of (B1) patterned and undeformed Ag NPs on a glass slide, (B2) patterned and undeformed Ag NPs remaining on glass slide after removing NPs using a thin film. Taken with permission of ref 1. .... 59

Figure 2. 17: A i-A iii, Schematic illustration of the transfer of NPs onto a clear polymer-film. (A i) Patterned and undeformed NPs on glass slide; (A ii) applying Clear First Contact polymer, letting it dry and peeling off (NPs transferred onto the polymer-film); (A iii) NPs remained on the glass slide. Dark field microscope images of patterned and undeformed NPs on (B i) glass slide and (B ii) undeformed NPs on polymer-film, (B iii) remaining NPs on the glass slide. Dark field microscope images of patterned and undeformed NPs on (C i) glass slide and (C ii) on polymer-film, (C iii) remaining NPs on the glass slide. Dark field microscope images of patterned NPs on (D i) glass slide after removing undeformed NPs and (D ii) patterned NPs on polymer-film, (D iii) remaining NPs on the glass slide. Taken with permission of ref 1. .... 61

Figure 2. 18: Photograph showing the deformation technique employed in this study. The rolling pin was placed on one end of the slide to begin with. A mechanical force was applied by the ESM 303 as the glass tube was rolled over the length of the glass substrate 10 times. The applied force was varied from 0 to 50 N, and a constant rolling speed of 500  $\mu\text{m/s}$  was used in each experiment. The glass tube was cleaned several times using acetone and distilled water prior to use. A..... 125

Figure 3. 1: (A) Schematic illustration of nanophosphors synthesis according to co-precipitate method. (i) Mixture of  $\text{Gd}(\text{NO}_3)_3$  and  $\text{Eu}(\text{NO}_3)_3$  or  $\text{Tb}(\text{NO}_3)_3$ , (ii)  $\text{Ln}^{3+}$ -citrate $^{3-}$  complex appears as a clear solution, (iii) formation of  $\text{NaGdF}_4:\text{Ln}^{3+}$  nanophosphors. Zoom out TEM images of (B1)  $\text{NaGdF}_4:\text{Eu}$  and (C1)  $\text{NaGdF}_4:\text{Tb}$  nanophosphors. Zoom in TEM images of (B2)  $\text{NaGdF}_4:\text{Eu}$  and (C2)  $\text{NaGdF}_4:\text{Tb}$  nanophosphors. Histograms of the average diameter of (B3)  $\text{NaGdF}_4:\text{Eu}$  and (C3)  $\text{NaGdF}_4:\text{Tb}$ . Powder XRD pattern compared to PDF cards 27-0699 of (B4)  $\text{NaGdF}_4:\text{Eu}$  and (C4)  $\text{NaGdF}_4:\text{Tb}$ . Taken with permission of ref 1. .... 82

Figure 3. 2: TEM images of  $\text{NaGdF}_4$  doped with (i) 0.1%, (ii) 1%, (iii) 15%, (iv) 20%, (v) 100% Eu synthesized using the co-precipitate method. Scale bar is equal to 100 nm. XRD patterns of (A) Eu and (B) Tb-doped  $\text{NaGdF}_4$  (Gd: dopant molar ratio = 1: 0.1, 1, 15, 20, 100%). XRD data were collected using single-crystal XRD as an alternative of powder XRD. PDF card is 27-0699. Taken with permission of ref 1. .... 83

Figure 3. 3: X-ray excited optical luminescence (XEOL) of (A)  $\text{NaGdF}_4:\text{Eu}$  and (B)  $\text{NaGdF}_4:\text{Tb}$  nanophosphors. Eu and Tb dopant fraction (mol% added to reagents vs. Gd) of  $\text{NaGdF}_4$  nanophosphors varied from 0.1% to 100%. X-ray luminescence intensities of

nanophosphors were normalized to the 620 nm peak intensity from commercial GOS:Eu and Tb microposphors. Spectra have been vertically displaced for ease of comparison. Taken with permission of ref 1. .... 85

Figure 3. 4: (A) Schematic illustration of nanophosphors synthesis according to co-precipitate method. (i) Mixture of  $\text{Gd}(\text{NO}_3)_3$  and  $\text{Eu}(\text{NO}_3)_3$  or  $\text{Tb}(\text{NO}_3)_3$ , (ii)  $\text{Ln}^{3+}$ -citrate<sup>3-</sup> complex appears as a clear solution, (iii) formation of  $\text{NaGdF}_4:\text{Ln}^{3+}$  nanophosphors, (iv) hydrothermally treated  $\text{NaGdF}_4:\text{Ln}^{3+}$  nanophosphors. TEM images of hydrothermally treated (B1)  $\text{NaGdF}_4:\text{Eu}$  and (B2)  $\text{NaGdF}_4:\text{Tb}$  nanophosphors. (B3) Powder XRD pattern compared to PDF cards 27-0699 of  $\text{NaGdF}_4:\text{Eu}$  and  $\text{NaGdF}_4:\text{Tb}$ . Taken with permission of ref 1. .... 86

Figure 3. 5: TEM images of  $\text{NaGdF}_4$  doped with (i) 0.1%, (ii) 1%, (iii) 15%, (iv) 20%, (v) 100% Eu synthesized using the hydrothermal method. Scale bar is equal to 100 nm. XRD patterns of (A) Eu- and (B) Tb-doped  $\text{NaGdF}_4$  (Gd: dopant molar ratio= 1: 0.1, 1, 15, 20, 100%). XRD data were collected using single-crystal XRD as an alternative of powder XRD. PDF card is 27-0699. Taken with permission of ref 1. .... 86

Figure 3. 6: XEOL of hydrothermally treated (A)  $\text{NaGdF}_4:\text{Eu}$  and (B)  $\text{NaGdF}_4:\text{Tb}$  nanophosphor. Mol fraction of Eu and Tb dopant vs. Gd in reagent mixture varied from 0.1% to 100%. X-ray luminescence intensities of nanophosphors were normalized to the height of 620 nm peak of commercial GOS:Eu and Tb microparticles. Spectra have been vertically displaced by adding a baseline for ease of comparison. Taken with permission of ref 1. .... 87

Figure 3. 7: Metal composition of nanophosphors calculated using ICP-OES measurements. The graph of percent metal ratio of nanophosphor vs. percent molar fraction of dopant added of  $\text{NaGdF}_4:\text{Eu}$  synthesized by (A1) co-precipitate and (A2) hydrothermal methods and  $\text{NaGdF}_4:\text{Tb}$  synthesized by (B1) co-precipitate and (B2) hydrothermal methods. Note, the amount of Tb in  $\text{NaGdF}_4:0.1\%\text{Tb}$  was not calculated as it is lower than the limit of detection of the instrument. Take with permission of ref 1. . 88

Figure 3. 8: (A) Schematic illustration of nanoparticle coating with silica. (i)  $\text{NaGdF}_4:\text{Ln}^{3+}$  nanophosphors, (ii) silica-coated  $\text{NaGdF}_4:\text{Ln}^{3+}$  nanoparticles. (B1) TEM images of silica-coated  $\text{NaGdF}_4$  nanophosphors Eu-doped. (B2) Histograms of the diameter of silica-coated  $\text{NaGdF}_4:\text{Ln}^{3+}$  nanoparticles. (B1) TEM images of silica-coated  $\text{NaGdF}_4$  nanophosphors Eu-doped. (B2) Histograms of the diameter of silica-coated  $\text{NaGdF}_4:\text{Eu}$ . Take with permission of ref 1. .... 89

Figure 3. 9: XEOL spectra of silica-coated (A)  $\text{NaGdF}_4:\text{Eu}$  and (B)  $\text{NaGdF}_4:\text{Tb}$  compared to  $\text{NaGdF}_4:\text{Eu}$  and  $\text{NaGdF}_4:\text{Tb}$  synthesized using co-precipitate method. Taken with permission of ref 1. .... 90

Figure 3. 10: (A) TGA and (B) DSC of  $\text{NaGdF}_4:\text{Eu}$  and  $\text{NaGdF}_4:\text{Tb}$  nanophosphors synthesized using co-precipitate and hydrothermal methods and  $\text{NaGdF}_4:\text{Eu}@ \text{SiO}_2$ . Taken with permission of ref 1. .... 91

Figure 3. 11: TGA thermograms showing (A) weight loss of synthesized nanophosphors, (B) derivative of weight loss (C) DSC of sodium citrate and PVP. Taken with permission of ref 1.....	92
Figure 3. 12: (A) SEM image and (B) XEOL of NaGdF <sub>4</sub> :Eu annealed at 1000 °C for 6 h compared to NaGdF <sub>4</sub> :Eu nanophosphors synthesized using co-precipitate and hydrothermal methods. Taken with permission of ref 1.....	93
Figure 3. 13: TEM images of NaGdF <sub>4</sub> :Eu@SiO <sub>2</sub> nanophosphors annealed at (A) 400 °C, (B) 600 °C (C) 1000 °C. Taken with permission of ref 1.....	94
Figure 3. 14: (A) XEOL of NaGdF <sub>4</sub> :Eu@SiO <sub>2</sub> annealed at 400 °C, 600 °C and 1000 °C for 6 h. (B) Powder XRD pattern of annealed NaGdF <sub>4</sub> :Eu@SiO <sub>2</sub> at 600 °C and 1000 °C compared to PDF cards 00-056-0184 and 00-027-0699 biotin functionalized NaGdF <sub>4</sub> :Eu@SiO <sub>2</sub> . Taken with permission of ref 1.....	94
Figure 3. 15: X-ray excited optical luminescence (XEOL) spectra of bare synthesized, silica coated, and silica coated annealed Eu-doped NaGdF <sub>4</sub> NPs. Taken with permission of ref 1.....	95
Figure 3. 16: XEOL spectra of NaGdF <sub>4</sub> :Eu@SiO <sub>2</sub> unannealed and annealed at 150, 400, and 1000 °C for 12 hours. Taken with permission of ref 1.....	96
Figure 3. 17: Schematic illustration of (A) silica coated nanophosphors functionalized with biotin (i) silica-coated NaGdF <sub>4</sub> :Eu nanophosphors, (ii) amine-functionalized nanophosphors, (iii) biotin-functionalized nanophosphors. Biotin is connected to amine-functionalized nanophosphors via sulfo-NHS groups, (B) biotin functionalized nanophosphors attach to streptavidin coated silica microbubbles. (i) streptavidin-coated silica microbubbles, (ii) biotin-functionalized nanophosphors attached to streptavidin-coated silica microbubbles. (C) SEM image showing biotin-functionalized nanophosphors attached to streptavidin-coated microbubbles. Taken with permission of ref 1.....	97
Figure 3. 18: Schematic illustration of measuring XEOL of NaGdF <sub>4</sub> :Eu filled in capillaries (A1) without tissue (B1) sandwiched with two 5 mm porcine tissues. XEOL of NaGdF <sub>4</sub> :Eu filled in capillaries (A2) without tissue (B2) sandwiched with two 5 mm porcine tissues. Exposure time was 10 s without tissue and 60 s through tissue. Taken with permission of ref 1.....	99
Figure 3. 19: XELCI images of NaGdF <sub>4</sub> :Eu dispersion in capillaries (A) XELCI images without tissue (i) image of 620 nm intensity (counts) vs. position. (ii) Image of 700 nm intensity (counts) vs. position (iii) XELCI ratio image (intensity ratio of 620 nm and 700 nm). (B) XELCI images of the same capillaries sandwiched between two 5 mm porcine tissue slices (i) 620 nm image (ii) 700 nm image (iii) XELCI ratio image. (iv) Superimposed 620 nm image and X-ray transmittance images. Current was 200 μA without tissue and 600 μA through tissue. 1 mm scale bar is same for all images. Taken with permission of ref 1.....	100

Figure 3. 20: Full-scale XEOL of NaGdF <sub>4</sub> : Eu in capillaries A) without tissue B) sandwiched between 5 mm slices of porcine tissue. Taken with permission of ref 1. ...	101
Figure 3. 21: Magnetic resonance images (MRI) of NaGdF <sub>4</sub> :Eu and NaGdF <sub>4</sub> :Tb nanoparticle suspensions in water. (A) T1 weighted and (B) T2 weighted images with various nanoparticle concentrations. 0 mM = DI water. 1 cm scale bar is for both T1 and T2 weighted images. (C) Longitudinal relaxation rate vs. concentration for nanoparticle suspensions. (D) Transverse relaxation rate vs. concentration. Dashed lines are linear fits to data. Taken with permission of ref 1. ....	102
Figure 4. 1: Design of new lateral flow assay to test anti-spike IgG and IgA in human saliva. ....	122
Figure 4. 2: Schematic illustration of (i) preparing RBD conjugated AuNPs and anti-human IgG conjugated Ulfa tag, (ii) combining RBD conjugated AuNPs, human IgG conjugated Ulfa tag, and biotin-conjugated AuNPs, (iii) dipping the LFA test strip. Images of LFA test strip. Images of LFA test strips after running (B) human anti-spike IgG and (C) human anti-spike IgA. ....	123
Figure 4. 3: (A) Schematic illustration of functionalizing route of RBD functionalized AuNPs. (B) UV-Vis spectra showing $\lambda_{max}$ of bare AuNPs, Au@PEG, Au@PEG:RBD and RBD protein in different buffer solutions. ....	125
Figure 4. 4: (A) Schematic illustration of RBD functionalized AuNPs binding to anti-spike IgG GOS:Eu microparticles. (B) Image showing control and the sample under UV light irradiation. (C) TEM image of RBD functionalized AuNPs bound to anti-spike IgG GOS:Eu microparticles. (D) X-ray excited optical luminescence of control and the sample. ....	127
Figure 5. 1: (A) Sterilizing a spatula by dipping in 70%ETOH and flaming. (B) Taking a 1 cm x 1 cm agar chunk from a NGM agar plate containing <i>C. elegans</i> . (C) transferring agar chunk into a fresh plate with an <i>E. coli</i> lawn. ....	140
Figure 5. 2: (A) A Photograph (B)schematic diagram of the experimental setup. The schematic diagram's right shows an X-ray spot visualized on a Grafchromic film and a worm targeted to X-ray exposure. ....	143
Figure 5. 3: The behavior of Pmyo-3::lite-1 (A1) before X-ray on and (A2) after X-ray on. The behavior of N2 (B1) before X-ray on and (B2) after X-ray on. The purple region corresponds to the worm movement during 10s before or 10s after the X-ray on. Worm shape and location are equivalent to the initial frame before or after the X-ray on. ....	144
Figure 5. 4: MATLAB generated an image of <i>Pmyo-3::lite-1</i> 1s before and after ejecting an egg. The blue circle shows the ejected egg. ....	145
Figure 5. 5: A graph of the number of eggs ejected after X-ray on vs. worm number ( <i>Pmyo-3::lite-1</i> ). ....	146
Figure 6. 1: SEM images of Ag NPs (A) unrolled and (B) rolled AgNPs. (C) SEM image of fused NPs during the deformation process .....	152

Figure 6. 2: Methyl orange color reduction by NaBH <sub>4</sub> using Ag NPs as a catalysts. (Ai-Ci) Negative controls. (Aii) 10 minutes and (Aiii) 15 minutes after adding 200 µL of 1% (v/v) AgNPs. Five minutes after adding (Bii) 200 µL and (Biii) 400 µL of 1% (v/v) AgNPs. Five minutes after adding 100 µL of (Cii) 100 nm and (Biii) 50 nm of 1% (v/v) AgNPs. ....	153
Figure 6. 3: (A) Low resolution and (B) High-resolution XEOL spectra from NaGdF <sub>4</sub> :Eu, Gd <sub>2</sub> O <sub>2</sub> S:Eu and a mixture of both with spectrally distinct peaks. ....	155
Figure 6. 4: Calibration curve of (Ai) 616/626 nm intensity ratio and (Aii) 695/703 intensity ratio vs weight of NaGdF <sub>4</sub> :Eu (mg) of simulated data. Calibration curve of (Bi) 616/626 nm intensity ratio and (Bii) 695/703 intensity ratio vs weight of NaGdF <sub>4</sub> :Eu (mg) of experimented data. ....	157
Figure 6. 5: Calibration curve of (Ai) 626/616 intensity ratio and (Aii) 703/695 intensity ratio vs. weight of NaGdF <sub>4</sub> :Eu (mg) of simulated data. Calibration curve of (Ai) 626/616 intensity ratio and (Aii) 703/695 intensity ratio vs. weight of GOS:Eu (mg) of experimented data. ....	158
Figure 6. 6: (A) Schematic illustration of protein depletion assay. (B) UV-Vis spectra show $\lambda_{\max}$ of AuNPs after bioconjugation, RBD before, and after bioconjugation. ....	160

## CHAPTER ONE

### INTRODUCTION

Materials with at least one dimension in the range of 1-100 nm are known as nanomaterials. Compared to biological structures, the nanoparticle size range lies between the size of DNA and most viruses, and they can be observed under electron microscopes and X-ray crystallography (Figure 1.1- figures were taken from various sources<sup>1,2</sup>). Nanoparticles have unique properties compared to their bulk materials, such as optical properties and a high surface-to-volume ratio necessary for biomedical (bioimaging, sensing) and other industries (catalysis). Nanoparticles such as plasmonic, silicon, quantum dots, and lanthanide-doped nanoparticles have unique optical properties (e.g., generating visible light). The other important feature of nanoparticles is they have a large surface area and internal volume that can be used as a platform for carrying and delivering several different “payloads” to control their optical, X-ray, magnetic, drug release, and other properties. These platforms can be functionalized with biomolecules such as proteins (antibodies, antigens, enzymes, etc.)<sup>3,4</sup> and nucleotides (single-strand DNA, RNA)<sup>5</sup> to target biomarkers *in vitro* and *in vivo*<sup>6</sup>. Due to the nanoparticles' optical properties and surface area are widely used in the biomedical field for bioimaging, sensing, and therapeutic applications<sup>7</sup>.

The size of a nanoparticle plays a vital role in these applications due to size-dependent optical properties and penetration through vascular systems, and retention time in the blood circulation system. Here we are interested in studying the optical properties of plasmonic and X-ray luminescence nanoparticles around 100 nm in size for



bioimaging and sensing applications. Nanoparticles in this range ( $\sim 100$  nm) have prolonged circulation time and tend to accumulate in perivascular spaces of permeable tissues such as liver and spleen, tumor, site of inflammation, and angiogenesis, allowing bicomponent imaging. Also, the nanoparticles smaller than 5-10 nm and  $\sim 70$  nm are removed by fast renal filtration and fenestrae of hepatic sinusoids filtration respectively,<sup>8-10</sup> and larger than  $\sim 200$  nm by endocytosis or phagocytosis (mononuclear phagocyte system (MPS))<sup>8,9,11</sup>, limiting bioimaging. Other than the size of the nanoparticles, shape, hydrophobicity/hydrophilicity, surface charge, and functional groups attached to nanoparticles are important in blood circulation and penetration through tissue<sup>12</sup>.

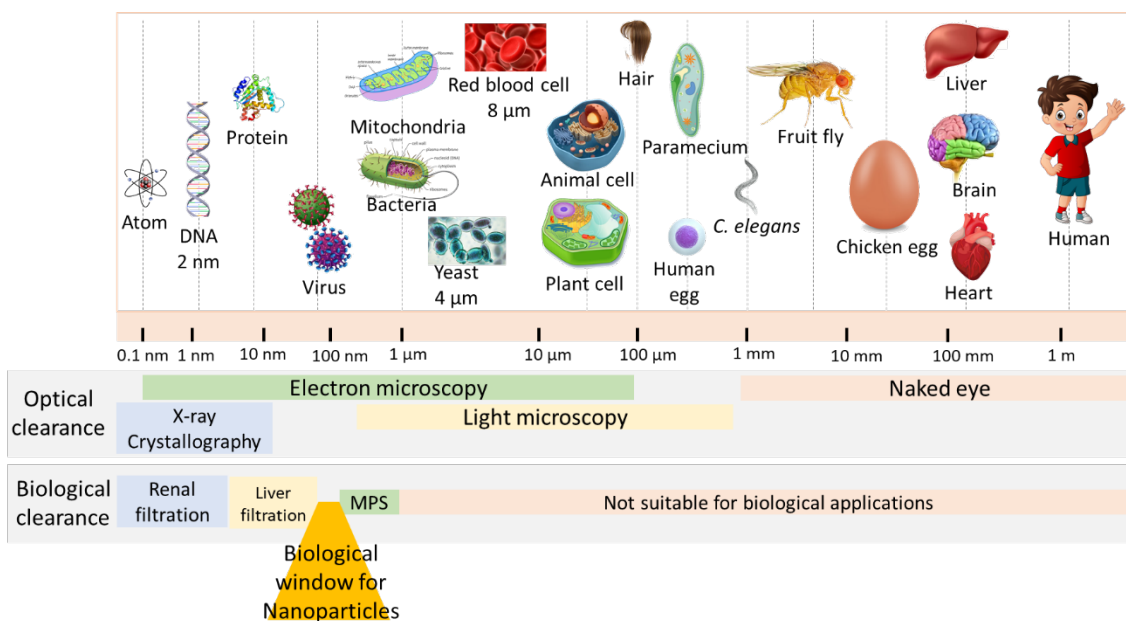


**Figure 1. 1: Size comparison of nanoparticles of interest to some biological components. Modified from ref. 1.**

In this dissertation, we are interested in developing plasmonic and X-ray luminescence nanoparticles for bioimaging and sensing applications. Under this theme,

three different research projects were carried out to understand, alter and enhance the optical properties of these nanoparticles. Also, they were functionalized and used in bioimaging and sensing applications.

The size-dependent optical properties are crucial in biomedical applications, and it is discussed in this chapter for plasmonic and X-ray luminescence nanoparticles (1.1-1.2).

### **1.1. Plasmonic Nanoparticles for Imaging and Sensing Applications**

Plasmonic nanoparticles such as gold (Au) and silver (Ag) have a characteristic optical property called localized surface plasmon resonance (LSPR). As described in the literature, LSPR is when the incident light impinges on a nanoparticle, it generates enhanced electromagnetic fields that are localized at the surface of the nanoparticle (Figure 1.1)<sup>13,14</sup>. When the incident light strikes a nanostructure, it collectively oscillates the conduction band electrons, resulting in absorption and/or a scattering of the wavelength of the incident light by the nanostructure.

For particles much smaller than the wavelength of light, the nanoparticle's electromagnetic behavior can be classically approximated by a dipole response. For ellipsoidal particles, the electric polarization generated in the particle in response to an alternating electromagnetic wave (light) depends on the particle shape, electric permeability, and incident light wavelength and polarization. The extinction can be calculated from the particle's polarization according to the following equation, with the

first term corresponding to absorption and the second term to scattering: (Equation 1.1)<sup>15,16</sup>.

$$Extinction = \frac{8\pi^2(\chi+1)^2 Na^3 \epsilon_m^{3/2}}{3\lambda \ln(10)} \frac{\epsilon_i}{(\epsilon_r + \chi \epsilon_m)^2 + \epsilon_i^2} + \frac{128\pi^5(\chi+1)^2 Na^6 \epsilon_m^2}{27\lambda^4 \ln(10)} \frac{(\epsilon_r - \epsilon_m)^2 + \epsilon_i^2}{(\epsilon_r + \chi \epsilon_m)^2 + \epsilon_i^2} \dots 1.1$$

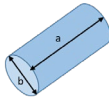
Where N= electron density of the nanoparticle, a= radius of the nanoparticle,  $\epsilon_m$ = dielectric constant of the surrounding medium,  $\epsilon_i$ = imaginary portion of the metallic nanoparticle's dielectric function,  $\epsilon_r$ = real portion of the metallic nanoparticle's dielectric function,  $\chi$ = shape- factor (2 for nanospheres) related to the depolarization factor L as  $1/L - 1$ , and  $\lambda$ = wavelength of incident light. Since the absorption term has an  $a^3$  dependence, while the scattering term has an  $a^6$  dependence, absorption dominates for small particles, while scattering dominates for large particles, the transition is typically around  $\sim 30$  nm.<sup>17</sup> The depolarization factor can explain shape dependence LSPR (Figure 1.1C)<sup>15</sup>, which has three components,  $L_1$ ,  $L_2$ ,  $L_3$ , along each axis (Equations 1.2-1.4)<sup>15,16</sup>. The corresponding LSPR frequencies are different in different directions. For a nanorod with  $a > b = c$ ,

$$L_1 = \frac{1-e^2}{e^2} \left( \frac{1}{2e} \ln \left( \frac{1+e}{1-e} \right) - 1 \right) \dots 1.2$$

$$L_2 = L_3 = \frac{1-L_1}{2} \dots 1.3$$

$$e = \sqrt{1 - \frac{1}{R^2}} \dots 1.4$$

$R^2$ = aspect ratio (a/b)



From equation 1.1, a noble metal nanoparticle's absorption, scattering, and extinction spectra each have a maximum  $\lambda_{\max}$  which occurs when the close to when  $\epsilon_r + \chi \epsilon_m = 0$  and the denominator,  $(\epsilon_r + \chi \epsilon_m)^2 + \epsilon_i^2$ , is minimized. Figure 1.1B shows the

dielectric function of silver. The imaginary part is relatively frequency independent through the visible spectral range, while the real part is rapidly increased to a large negative value with wavelength. Specifically, the real part of the metal dielectric function can be approximately fit to the Drude model,  $\epsilon_r = 1 - \lambda^2/\lambda_p^2$  where  $\lambda_p$  is the plasmon resonance wavelength of the metal. Plugging this into the condition above for resonance, we have  $\epsilon_r + \chi\epsilon_m = 0 \rightarrow 1 - \frac{\lambda_{max}^2}{\lambda_p^2} + \chi\epsilon_m = 0$ . When  $\chi\epsilon_m \gg 1$ , we find  $\lambda_{max} \approx \lambda_p \sqrt{(\chi\epsilon_m)}$ . For media with low absorbance, the square root of the dielectric constant is essentially equal to the refractive index; thus, we have  $\lambda_{max} \approx \lambda_p n \sqrt{\chi}$ . The absorption and scattering of the nanoparticle thus depend on the material composition (especially  $\lambda_p$ ), nanoparticle size (which at very small sizes can affect the metal's dielectric properties and at sizes above around  $\lambda/2\pi$  need a more complex theory than the dipole approximate, to include phase retardation affects and multipole resonance), nanoparticle shape (especially the shape factor), refractive indices of surface-bonded species of nanoparticles, the refractive index of surrounded media, etc<sup>18</sup>

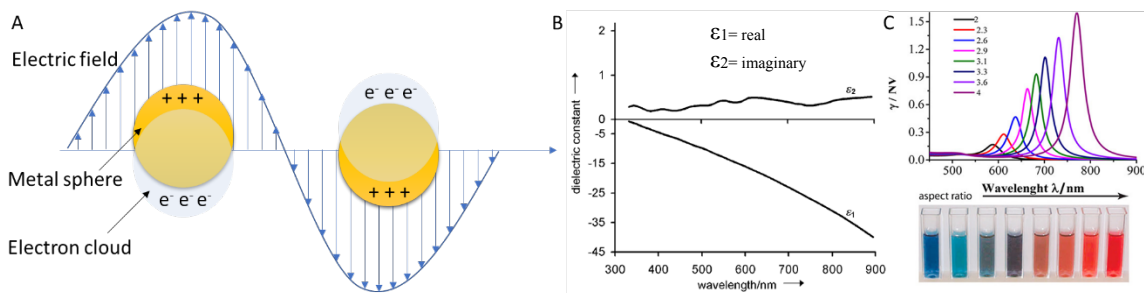


**Figure 1. 2: (A) Schematic diagram illustrating a localized surface plasmon resonance. (B) real and imaginary parts of the dielectric function of silver as a function of wavelength. Taken with permission of ref. 6 (C) Calculated extinction spectra of gold nanorods with varying aspect ratios. Taken with permission of ref. 3**

The size, shape, and medium refractive index tunability of LSPR and associated optical absorption and scattering is useful for developing optoelectronic devices, biosensors, identifying molecules, *in vivo* imaging, etc<sup>14,19,20</sup>. Plasmonic nanoparticle arrays (1,2 and 3D) are widely used in manipulating light and matter interactions at the nanoscale and in diverse applications such as developing biosensors due to photonic and plasmonic attributes. These plasmonic nanoparticle arrays show enhanced electromagnetic fields, high-quality optical responses (enhanced and well-resolved extinction peaks, red or blue-shift in plasmon resonance, and Surface Enhanced Raman Spectroscopy (SERS)<sup>21–23</sup>). Different regions of nanoparticle arrays are also used in multiplex diagnostic systems such as lab-on-a-chip devices to detect multiple biomarkers simultaneously. Therefore, investigating methods to prepare nanoparticle arrays are crucial.

There are several methods to prepare nanoparticle arrays, such as e-beam lithography, chemical vapor deposition, pulsed laser ablation, etc<sup>24</sup>. However, these methods are complex, time-consuming, expensive chemical methods that require trained personnel to perform. In 1996 Stephen Chuo introduced the nanoimprint lithographic technique as a low-cost, high throughput technique alternative to photolithography and e-beam lithography<sup>25</sup>. Most nanoimprint lithographic approaches use contact printing<sup>26</sup>, chemical etching<sup>27</sup>, and reel to reel processes<sup>28</sup>.

Similar to preparing nanoparticle arrays transferring these prepared nanoparticles onto desired substrates (thin-films or flexible polymers) is also important (hybrid

optics<sup>29</sup>). Most common approaches require high temperature, vacuum conditions, sacrificial layers, and surfactant coated nanoparticles<sup>30,31</sup>.

Developing inexpensive, simple, and robust techniques to prepare nanoparticle arrays with controlled shape and transferring them to desired substrates are still challenging and crucial matters. Chapter two describes the development of simple and robust mechanical methods to make nanoparticle arrays and transfer them onto a thin polymer film.

## **1.2. X-ray Luminescence Nanoparticles for Imaging and Sensing Applications**

Like plasmonic nanoparticles, X-ray luminescence nanoparticles (scintillators, nanophosphors) are nanomaterials that have an interesting optical property called X-ray excited optical luminescence (XEOL). X-ray photons can maintain focus through thick tissue, unlike optical photons (which have short mean free-scattering paths in tissue), and thus one can use a narrow X-ray beam only to excite XEOL from nanoscintillators in a specific region. By scanning the X-ray through the tissue and using the known X-ray beam location as a permissible region for optical emission, one can reconstruct high spatial resolution, low background images through thick tissue. Nanophosphors are nanostructured, and insulating materials efficiently emit visible light under X-ray (particle and photon) excitation. During the last few decades, they have been widely studied for applications like sensors<sup>32,33</sup> and medical imaging<sup>34,35</sup>, etc. However, synthesizing nanosized, monodisperse particles with bright luminescence is still

challenging and their properties depend on precursor formation, particle growth, the formation of lattice defects, crystal domain size, and surface modifications<sup>36,37</sup>.

Many different synthesis routes (organic and inorganic) have been developed to synthesize nanophosphors. Co-precipitation, thermal decomposition, and solvothermal synthesis are some examples. Some synthesis routes, such as hydrothermal synthesis and sol-gel process, are performed in aqueous media (inorganic synthesis)<sup>38</sup>.

The co-precipitate method is one of the most accessible and convenient approaches to synthesizing X-ray luminescence nanoparticles because of its mild reaction conditions, low cost, simple protocols, and short reaction time. The co-precipitation process generally shows the following characteristics according to LaMer's model<sup>39</sup>. The products are insoluble species formed under conditions of supersaturation, 1. A large number of seed particles will be created during nucleation, 2. Formation and growth of seed particles decrease reagent concentration below minimum nucleation concentration and existing seeds growth, limited by reagent diffusion or reaction until eventually, reagent concentration reaches equilibrium with particles. 3. The secondary processors such as Ostwald ripening and aggregation affect the particle size, morphology, and properties. The supersaturation conditions necessary to induce precipitation are usually a chemical reaction<sup>40</sup> (e.g.,  $\text{Gd}(\text{NO}_3)_3 + \text{Eu}(\text{NO}_3)_3 + \text{urea} \rightarrow \text{Gd}_2\text{O}(\text{CO}_3)_2 \cdot \text{H}_2\text{O}:\text{Eu}$ )<sup>41</sup>. However, nanoparticles synthesized by this method have low luminescence intensity. Therefore, annealing treatments are required to enhance the luminescence resulting in a phase transition from hexagonal ( $\alpha$ ) to cubic ( $\beta$ ).

In a broader sense, hydrothermal synthesis can be performed from room to high temperatures and low pressure to high-pressure environments<sup>42</sup>. However, the size and morphology of synthesized nanocrystals depend on the solvent's temperature, pressure and dielectric constant, etc. Hydrothermal syntheses are typically performed below 300 °C in an autoclave. As the temperature develops, solvent/water dramatically changes to supercritical conditions. Under supercritical conditions, the dielectric constant remains below 10, and the reaction medium becomes favorable for crystal growing, based on electrostatic theory. Therefore, supercritical solvents give a favorable reaction environment for particle formation by enhancing the reaction rate and creating a significant supersaturation based on the nucleation theory due to lowering the solubility<sup>43</sup>. The hydrothermal method usually gives a relatively high yield of desired products with controlled size, shape, and crystallinity.

One of our key goals was to synthesize the brightest luminescent particles for a given X-ray dose. The X-ray scintillators can serve as optical contrast agents with low background. Their position can be detected at high spatial resolution through tissue using a narrow X-ray beam: the X-ray beam provides a small permissible region for the light generation to excite only particles within the beam. The maximum quantum yield of X-ray scintillators (photons emitted per MeV) is determined by the band gap of the host matrix (Equation 1.5)<sup>44</sup>.

$$Y = \frac{10^6}{2.5E_{gap}} \dots\dots\dots 1.5$$

Where Y= quantum yield (photons per MeV of incident X-ray photon energy),  $E_{gap}$ = band gap (eV). The photons emitted have less energy than  $E_g$ , so the conversion



efficiency between absorbed X-ray energy and emitted optical energy is less than 1/2.5 (<40% energy efficiency); for example, it is around 10-15% in bulk Gd<sub>2</sub>O<sub>2</sub>S:Eu or Gd<sub>2</sub>O<sub>2</sub>S:Tb scintillators.

The X-ray luminescence yield of lanthanide-doped nanoparticles also depends on the nanoparticle's size, host material/ lattice structure, crystallinity, and amount of activator and impurity dopants, especially as these relate to energetic photoelectron and exciton diffusion lengths. High X-ray luminescence intensity can be achieved by choosing the best host materials (e.g., host materials with sulfur and oxygen are better than iodine and bromide, small band gap<sup>44</sup>), increasing crystallinity, and incorporating the right amount of dopants. Luminescence intensity is a key factor in most bioimaging applications (E.g., The quantum yield of bulk Gd<sub>2</sub>O<sub>2</sub>S:Eu is 60 000 photons per MeV.<sup>44</sup>) because it contributes to the sensitivity of the biomarker detection.

For bioimaging and sensing applications, understanding light attenuation and collection through tissue is important. Light attenuation through tissue is one of the fundamental limitations in optical imaging, and it reduces the number of photons emitted by the volume of tissue, leading to low sensitivity. The number of visible photons detected per voxel from a sample is calculated by equation 1.6.<sup>44</sup>

$$n_{visible} = D\Gamma fcVL \dots\dots\dots 1.6$$

Where  $n_{visible}$ = number of visible photons detected per voxel from a sample (signal), D= X-ray dose applied to the tissue (J/kg),  $\Gamma$ = X-ray to luminescence conversion efficiency (photons/J),  $f$ = X-ray absorption by particles/ absorption by tissue,  $c$ = nanoparticle concentration (volume fraction),  $V$ = voxel volume (kg),  $L$ = light collection efficiency

(includes transmission through tissue, capture through the light guide, and photodetector quantum efficiency).

Below, we work through a representative example, explaining trade-offs between dose, particle concentration, spatial resolution, and tissue depth for a given setup and nanophosphor quantum yield.

For example, the number of visible photons detected per voxel from a given sample can be calculated with the following information.

D, X-ray dose applied to the tissue= 0.01 Gray (J/kg)

$\Gamma$ , X-ray to luminescence energy efficiency of nanoparticles.

Assuming a quantum yield= 20 000 ph/MeV (if we consider 30% of bulk Gd<sub>2</sub>O<sub>2</sub>S:Eu), 1

eV=  $1.6 \times 10^{-19}$  J

$$= 20000 \text{ ph} / 1.6 \times 10^{-19} \times 10^6 \text{ eV} = 1.25 \times 10^{17} \text{ ph/J}$$

f, depends on the X-ray energy, but can be as high as ~500 for Gd<sub>2</sub>O<sub>2</sub>S (with scintillator absorbing 500x more than tissue) = 500

c, Nanoparticle concentration (volume fraction) = Volume of nanoparticles/Volume of tissue= Concentration of nanoparticles (g/mL)/ density of the nanoparticle (g/mL).

Assuming a concentration of 0.2 mg/mL, we have:

$$c = 0.2 \times 10^{-3} \text{ g/mL} / 7.43 \text{ g/mL} = 2.69 \times 10^{-5}$$

V, Voxel volume for a 0.5 mm cube= 0.125  $\mu$ L or  $1.31 \times 10^{-7}$  kg

L, Light collection efficiency= light transmittance to skin\* internal reflection at skin\* fraction captured through the light guide\* photodetector (PMT) quantum efficiency

The light transmittance to the skin is calculated using the following equation<sup>44</sup>.

$$I = I_0 e^{-\mu x} \dots\dots\dots 1.7$$

Where I= light transmitted to the skin, I<sub>0</sub>= light generated by the scintillator, μ= effective light attenuation coefficient of tissue, this depends strongly on wavelength and type of tissue, x= travel distance through tissue. Assuming, μ=0.42 mm<sup>-1</sup> (e.g., reported value for arm tissue at 620 nm,<sup>45</sup> and x= 0.6 cm, we get 8% transmittance through the tissue<sup>46</sup>.

To calculate the fraction captured through the light guide, the maximum fiber acceptance angle of 90 degrees for acrylic in air light guide<sup>47</sup>. Our system is fairly efficient with an acrylic light guide, which may collect light at 50 ° with 1-inch collection optics<sup>46</sup>. It was calculated using the following equation. (1-COS(RADIANS (50)))/2 = 17.86%. Note, some light aimed into tissue; naively estimate ½.

The PMT quantum efficiency of 5% at 600 nm was taken from the datasheet of photodetector module P25PC-16, SENS TECH, UK<sup>48</sup>.

Thus, the overall collection efficiency = 8%\* 0.5 \* 17.86%\* 5%= 3.6\*10<sup>-4</sup>

Putting this together, we get:

n<sub>visible</sub>, Number of visible photons detected per voxel from a sample=

$$\frac{0.01 \frac{\text{J}}{\text{kg}} * 1.25 * 10^{17} \text{ ph/J} * 500 * 2.69 * 10^{-5} * 1.31 * 10^{-7} \text{ kg} * 3.6 * 10^{-4}}{1} = 792 \text{ ph}$$

Thus, if 0.2 mg/mL of Gd<sub>2</sub>O<sub>2</sub>S:Eu nanoparticles are inserted 6 mm below the surface (skin) and irradiated with a 0.01 J/kg X-ray dose, with a light collection efficiency of 3.6\*10<sup>-4</sup>, 792 photos are generated per (500 μm<sup>3</sup>) voxel.

The next question is, 792 photons are enough to get a good signal. For that, we have to consider the background signal/ noise. Noise can be found experimentally or

must be higher than the fundamental limit from shot noise, which can be calculated using the following equation (1.8)<sup>49</sup>.

$$n_{eff} = \sqrt{n_D^2 + n_s^2} \dots \dots \dots 1.8$$

Where  $n_{eff}$ = total effective noise,  $n_D$ = shot noise from dark counts (generated from current that flows even when no photons are incident, depending on temperature),  $n_s$ = shot noise from detected photoelectrons.

In this scenario, noise mainly comes as shot noise from dark counts and detected XEOL signal. According to the PMT datasheet, dark counts (counts of photoelectrons) are 1000 s<sup>-1</sup> at 20 °C. Thus for a 1 s exposure,

$$n_{eff} = \sqrt{1000 + 792} = 42.$$

Considering the signal-to-noise ratio, it is 792/42= 18.9, a fair number. This is a representative calculation showing both the feasibility under possible scenarios as well as tradeoffs. In real-world performance, we may use X-ray scintillators with relatively low luminescence yield (e.g., <5%), may want to detect lower concentrations of particles, and need to achieve a small voxel size (e.g., 50 µm length), or image through thicker tissue with more light attenuation. Therefore, the number of photons detected per voxel (signal or signal-to-noise ratio) can be relatively small. However, several factors can be changed to obtain a high signal-to-noise ratio, such as 1) increasing the X-ray dose. For context, while one wants to minimize the dose, 0.01 J/kg could be improved as typical full-body equivalent doses, doses for rodents in µ-CT are 1-100 mJ/kg, and repeated sublethal doses are tolerated up to 3 J/kg, with lower doses tolerated for smaller exposed regions<sup>50</sup>; 2) increasing voxel volume (decreasing spatial resolution); 3) increasing nanoparticle

concentration; 4) improving light collection efficiency (this can be dramatically improved with better light collection optics and higher quantum efficiency photodetectors); or 5) decreasing dark counts by running faster acquisitions or decreasing PMT temperature. Given these variables, a sufficiently intense signal should be detectable through tissue with reasonable particle concentrations, X-ray doses, tissue thickness, and spatial resolution. However, there are tradeoffs with each of these variables, and using bright luminescence particles is key for allowing higher spatial resolution, lower dose, or lower particle concentration measurements.

As explained at the beginning of this section 1.2, we are interested in synthesizing bright X-ray luminescence nanoparticles and enhancing their luminescence intensity. However, our challenge is to obtain bright X-ray luminescence intensity with nanosized particles. Apart from choosing the right lattice structure, dopant amount, and reducing defects, nanoparticle annealing, surface passivation, and coating with inorganic and organic insulating layers<sup>51</sup> are some techniques used to enhance luminescence in X-ray luminescence and upconversion nanoparticles. Chapter three describes the synthesis of bright X-ray luminescence nanoparticles (NaGdF<sub>4</sub>:Eu and NaGdF<sub>4</sub>:Tb), annealing them to improve the X-ray luminescence intensity, and using them in spectroscopy and high-resolution imaging through tissue.

### **1.3. Applications of Plasmonic and X-ray Luminescence particles: Developing immunosensors**

As mentioned in the above sections, plasmonic and X-ray luminescence nanoparticles' optical properties and a surface area to functionalize them with biomolecules to develop biosensors.

To perform most clinical assays requires trained personnel and expensive, complex instruments. Therefore, most clinical assays are not readily available in developing countries and investigating and developing innovative analytical methods to accurately screen and diagnose diseases are important. In recent years, plasmonic and X-ray luminescence NPs have been widely used in developing immunoassays. immunosensors because of their interesting optical properties and increased surface area.

Plasmonic nanoparticles have interesting optical properties such as scattering and absorption of visible range wavelength due to surface plasmon resonance (SPR) to develop naked-eye immunoassays<sup>52-54</sup>, surface-enhanced Raman spectroscopy (SERS) to develop SERS-based immunoassays<sup>55-57</sup>. These properties are useful in the detection and quantification of analytes. Further, they have interesting enzyme mimicking properties important in increasing sensitivity<sup>54,58</sup>. Likewise, X-ray luminescence particles are used in developing X-ray luminescence-based immunoassays<sup>59,60</sup>. Due to the weak scattering and absorption of most biological tissue by X-ray excitation, a low-dose X-ray source can be used to produce intense, scintillating luminescence. Also, the other advantages are narrow and distinct spectral emission peaks, large optical penetration depth, negligible autofluorescence background, photochemical stability, and low toxicity<sup>41</sup>.

Therefore, taking advantage of plasmonic and X-ray luminescence particles, it is important to develop immunoassays/ immunosensors which are timely required. Chapter four describes the design and development of an LFA using gold nanoparticles to detect SARS-CoV-2 antibodies in human saliva and the proof of concept of an implantable immunoassay using gold nanoparticles and X-ray luminescence nanoparticles.

#### **1.4. Radiation-Induced Behavior of *Caenorhabditis elegans***

This section discusses a different concept to the main theme of optical properties of plasmonic and X-ray luminescence nanoparticles and functionalizing them for bioimaging and sensing applications. Here, we discuss the X-ray avoidance behavior of *C. elegans*. However, it can be related to the main theme regarding sensing X-ray radiation.

One of the goals of neuroscience is to understand how the actions of neurons and nerve systems cause behavior. To fulfill this goal, *C. elegans* can be used as a model with a number of unique advantages such as having a highly conserved and compact nervous system containing 302 neurons, simple anatomy, neurochemistry and genetics similar to mammals, optical transparency and small size, etc<sup>61</sup>. *C. elegans* is a tiny, free-living, transparent nematode (roundworm) that lives in a soil environment. The length of an adult worm is about 1-1.5mm (Figure 1.1). They are easy to grow on a petri dish seeded with *Escherichia coli* as a food source. Also, they are fast-growing animals with a short life cycle (3 days). It is difficult to see them with the naked eye because of their small size and transparency. However, dissecting microscopes are used to visualize their

movements, eating habits, developments, and laying eggs; confocal microscopes can be used to see cell development and function at a single-cell resolution. Further, proteins and other cell components can be visualized by fluorescence staining. *C. elegans* is a powerful model for eukaryotic genetic studies. They are the only animal for which the complete atlas of synaptic connectivity has been mapped and the first multicellular organism with a complete genome sequence<sup>62</sup>. *C. elegans* are widely used in studying sensory cues such as mechanical forces, temperature, chemicals, and radiation (especially UV), showing negative phototoxic effects<sup>63</sup>. Chapter five includes the study of X-ray stimulated egg ejection of *C. elegans*. This is the first research carried out to study X egg ejection of *C. elegans* using X-ray as a stimulant.

Chapter six includes the projects' summary and future work of chapters two, three, and four.

In summary, this dissertation focuses on developing plasmonic and X-ray luminescence nanoparticles for bioimaging and sensing applications. The main problems addressed in the dissertation are 1) developing a simple mechanical method to prepare plasmonic nanoparticle arrays and transfer nanoparticle arrays onto thin films, 2) enhancing the intensity of X-ray nanoparticles and imaging through tissue, 3) developing immunoassays using plasmonic and X-ray luminescence particles. Apart from the main topics, this also includes a study to discover and understand the X-ray stimulated behavior of *C. elegans*.



## 1.5. List of Publications

The following chapters in this dissertation are based on these papers.

Chapter two: Ameer, F. S.\*; Ranasinghe, M.\*; Varahagiri, S.\*; Benza, D. W.; Hu, L.; Willett, D. R.; Wen, Y.; Bhattacharya, S.; Chumanov, G.; Rao, A. M.; Anker, J. N. Impressively Printing Patterns of Gold and Silver Nanoparticles. *Nano Select*; 2021, 2 (12), 2407-2418. <https://doi.org/10.1002/nano.202000278>. (\*1st co-author)

Chapter three: Ranasinghe, M.; Arifuzzaman, M.; Rajamanthrilage, A. C.; Dickey, A.; Kolis, J. W.; Bolding, M.; Anker, J. X-Ray Excited Luminescence Spectroscopy and Imaging with NaGdF<sub>4</sub>:Eu and Tb. 2020. *RSC Adv.*, 2021, 11, 31717-31726. <https://doi.org/10.1039/D1RA05451A>.

Chapter four: In progress

Chapter five: Cannon, K. E.; Ranasinghe, M.; Do, A.; Pierce, H. M.; Millhouse, P. W.; Roychowdhury, A.; Foulger, S.; Dobrunz, L.; Anker, J. N.; Bolding, M. LITE-1 Dependent X-Ray Sensitivity in *C. Elegans*. *bioRxiv* 2019, 766568. <https://doi.org/10.1101/766568>. Submitted to *Frontiers in Cellular Neuroscience*

## 1.6. References

- (1) Rachael. Size Matters - The Scale of Biology – Examples and Fun Facts. *Rs' Science*, 2021.
- (2) Reth, M. Matching Cellular Dimensions with Molecular Sizes. *Nat Immunol* **2013**, 14 (8), 765–767. <https://doi.org/10.1038/ni.2621>.

- (3) Karmani, L.; Labar, D.; Valembois, V.; Bouchat, V.; Nagaswaran, P. G.; Bol, A.; Gillart, J.; Levêque, P.; Bouzin, C.; Bonifazi, D.; Michiels, C.; Feron, O.; Grégoire, V.; Lucas, S.; Borghet, T. V.; Gallez, B. Antibody-Functionalized Nanoparticles for Imaging Cancer: Influence of Conjugation to Gold Nanoparticles on the Biodistribution of  $^{89}\text{Zr}$ -Labeled Cetuximab in Mice. *Contrast Media & Molecular Imaging* **2013**, *8* (5), 402–408. <https://doi.org/10.1002/cmml.1539>.
- (4) Chen, J. S.; Chen, J.; Bhattacharjee, S.; Cao, Z.; Wang, H.; Swanson, S. D.; Zong, H.; Baker, J. R.; Wang, S. H. Functionalized Nanoparticles with Targeted Antibody to Enhance Imaging of Breast Cancer in Vivo. *Journal of Nanobiotechnology* **2020**, *18* (1), 135. <https://doi.org/10.1186/s12951-020-00695-2>.
- (5) Wickramathilaka, M. P.; Tao, B. Y. Characterization of Covalent Crosslinking Strategies for Synthesizing DNA-Based Bioconjugates. *Journal of Biological Engineering* **2019**, *13* (1), 63. <https://doi.org/10.1186/s13036-019-0191-2>.
- (6) Sapsford, K. E.; Algar, W. R.; Berti, L.; Gemmill, K. B.; Casey, B. J.; Oh, E.; Stewart, M. H.; Medintz, I. L. Functionalizing Nanoparticles with Biological Molecules: Developing Chemistries That Facilitate Nanotechnology. *Chem. Rev.* **2013**, *113* (3), 1904–2074. <https://doi.org/10.1021/cr300143v>.
- (7) Bogart, L. K.; Pourroy, G.; Murphy, C. J.; Puentes, V.; Pellegrino, T.; Rosenblum, D.; Peer, D.; Lévy, R. Nanoparticles for Imaging, Sensing, and Therapeutic Intervention. *ACS Nano* **2014**, *8* (4), 3107–3122. <https://doi.org/10.1021/nn500962q>.
- (8) Mitragotri, S.; Lahann, J. Physical Approaches to Biomaterial Design. *Nature Mater* **2009**, *8* (1), 15–23. <https://doi.org/10.1038/nmat2344>.

- (9) Stendahl, J. C.; Sinusas, A. J. Nanoparticles for Cardiovascular Imaging and Therapeutic Delivery, Part 1: Compositions and Features. *Journal of Nuclear Medicine* **2015**, *56* (10), 1469–1475. <https://doi.org/10.2967/jnumed.115.160994>.
- (10) Han, X.; Xu, K.; Taratula, O.; Farsad, K. Applications of Nanoparticles in Biomedical Imaging. *Nanoscale* **2019**, *11* (3), 799–819. <https://doi.org/10.1039/c8nr07769j>.
- (11) Rejman, J.; Oberle, V.; Zuhorn, I. S.; Hoekstra, D. Size-Dependent Internalization of Particles via the Pathways of Clathrin- and Caveolae-Mediated Endocytosis. *Biochem J* **2004**, *377* (Pt 1), 159–169. <https://doi.org/10.1042/BJ20031253>.
- (12) Rampado, R.; Crotti, S.; Caliceti, P.; Pucciarelli, S.; Agostini, M. Recent Advances in Understanding the Protein Corona of Nanoparticles and in the Formulation of “Stealthy” Nanomaterials. *Frontiers in Bioengineering and Biotechnology* **2020**, *8*.
- (13) Willets, K. A.; Van Duyne, R. P. Localized Surface Plasmon Resonance Spectroscopy and Sensing. *Annual Review of Physical Chemistry* **2007**, *58* (1), 267–297. <https://doi.org/10.1146/annurev.physchem.58.032806.104607>.
- (14) Long, Y.-T.; Jing, C. *Localized Surface Plasmon Resonance Based Nanobiosensors*; SpringerBriefs in Molecular Science; Springer Berlin Heidelberg: Berlin, Heidelberg, 2014. <https://doi.org/10.1007/978-3-642-54795-9>.
- (15) Peng, Y.; Xiong, B.; Peng, L.; Li, H.; He, Y.; Yeung, E. S. Recent Advances in Optical Imaging with Anisotropic Plasmonic Nanoparticles. *Anal. Chem.* **2015**, *87* (1), 200–215. <https://doi.org/10.1021/ac504061p>.

- (16) Enhanced Molecular Spectroscopy via Localized Surface Plasmon Resonance | IntechOpen <https://www.intechopen.com/chapters/51493> (accessed 2022 -04 -13).
- (17) Evanoff Jr., D. D.; Chumanov, G. Synthesis and Optical Properties of Silver Nanoparticles and Arrays. *ChemPhysChem* **2005**, 6 (7), 1221–1231. <https://doi.org/10.1002/cphc.200500113>.
- (18) *Topics in Fluorescence Spectroscopy*; Lakowicz, J. R., Geddes, C. D., Eds.; Plenum Press: New York, 1991.
- (19) Fratoddi, I. Hydrophobic and Hydrophilic Au and Ag Nanoparticles. Breakthroughs and Perspectives. *Nanomaterials* **2018**, 8 (1), 11. <https://doi.org/10.3390/nano8010011>.
- (20) Browning, L. M.; Huang, T.; Xu, X.-H. N. Real-Time in Vivo Imaging of Size-Dependent Transport and Toxicity of Gold Nanoparticles in Zebrafish Embryos Using Single Nanoparticle Plasmonic Spectroscopy. *Interface Focus* **2013**, 3 (3), 20120098. <https://doi.org/10.1098/rsfs.2012.0098>.
- (21) Hao, E.; Schatz, G. C. Electromagnetic Fields around Silver Nanoparticles and Dimers. *The Journal of Chemical Physics* **2004**, 120 (1), 357–366. <https://doi.org/10.1063/1.1629280>.
- (22) Wang, W.; Ramezani, M.; Väkeväinen, A. I.; Törmä, P.; Rivas, J. G.; Odom, T. W. The Rich Photonic World of Plasmonic Nanoparticle Arrays. *Materials Today* **2018**, 21 (3), 303–314. <https://doi.org/10.1016/j.mattod.2017.09.002>.

- (23) Ross, M. B.; Mirkin, C. A.; Schatz, G. C. Optical Properties of One-, Two-, and Three-Dimensional Arrays of Plasmonic Nanostructures. *J. Phys. Chem. C* **2016**, *120* (2), 816–830. <https://doi.org/10.1021/acs.jpcc.5b10800>.
- (24) Ikumapayi, O. M.; Akinlabi, E. T.; Adeoye, A. O. M.; Fatoba, S. O. Microfabrication and Nanotechnology in Manufacturing System – An Overview. *Materials Today: Proceedings* **2021**, *44*, 1154–1162. <https://doi.org/10.1016/j.matpr.2020.11.233>.
- (25) 77 Chou\_Nanoimprint Lithography\_JVST B\_1996.Pdf.
- (26) Sreenivasan, S. V. Nanoimprint Lithography Steppers for Volume Fabrication of Leading-Edge Semiconductor Integrated Circuits. *Microsyst Nanoeng* **2017**, *3* (1), 1–19. <https://doi.org/10.1038/micronano.2017.75>.
- (27) Braun, G. B.; Friman, T.; Pang, H.-B.; Pallaoro, A.; de Mendoza, T. H.; Willmore, A.-M. A.; Kotamraju, V. R.; Mann, A. P.; She, Z.-G.; Sugahara, K. N.; Reich, N. O.; Teesalu, T.; Ruoslahti, E. Etchable Plasmonic Nanoparticle Probes to Image and Quantify Cellular Internalization. *Nature Mater* **2014**, *13* (9), 904–911. <https://doi.org/10.1038/nmat3982>.
- (28) Lim, H.; Choi, K.-B.; Kim, G.; Park, S.; Ryu, J.; Lee, J. Roller Nanoimprint Lithography for Flexible Electronic Devices of a Sub-Micron Scale. *Microelectronic Engineering* **2011**, *88* (8), 2017–2020. <https://doi.org/10.1016/j.mee.2011.02.018>.
- (29) Shutsko, I.; Böttge, C. M.; Barga, J. von; Henkel, A.; Meudt, M.; Görrn, P. Enhanced Hybrid Optics by Growing Silver Nanoparticles at Local Intensity Hot Spots. *Nanophotonics* **2019**, *8* (9), 1457–1464. <https://doi.org/10.1515/nanoph-2019-0019>.

- (30) Zhou, J.; Ni, J.; Song, Y.; Chen, B.; Li, Y.; Zhang, Y.; Li, F.; Jiao, Y.; Fu, Y. Transfer of Ordered Nanoparticle Array and Its Application in High-Modulus Membrane Fabrication. *J. Mater. Chem. C* **2014**, 2 (31), 6410–6414.  
<https://doi.org/10.1039/C4TC00722K>.
- (31) Ko, H.; Jiang, C.; Tsukruk, V. V. Encapsulating Nanoparticle Arrays into Layer-by-Layer Multilayers by Capillary Transfer Lithography. *Chem. Mater.* **2005**, 17 (22), 5489–5497. <https://doi.org/10.1021/cm050864p>.
- (32) Huang, C.; Wen, T.; Shi, F.-J.; Zeng, X.-Y.; Jiao, Y.-J. Rapid Detection of IgM Antibodies against the SARS-CoV-2 Virus via Colloidal Gold Nanoparticle-Based Lateral-Flow Assay. *ACS Omega* **2020**, 5 (21), 12550–12556.  
<https://doi.org/10.1021/acsomega.0c01554>.
- (33) Uzair, U.; Johnson, C.; Beladi-Behbahani, S.; Rajamanthrilage, A. C.; Raval, Y. S.; Benza, D.; Ranasinghe, M.; Schober, G.; Tzeng, T.-R. J.; Anker, J. N. Conformal Coating of Orthopedic Plates with X-Ray Scintillators and PH Indicators for X-Ray Excited Luminescence Chemical Imaging through Tissue. *ACS Appl. Mater. Interfaces* **2020**, 12 (47), 52343–52353. <https://doi.org/10.1021/acsami.0c13707>.
- (34) Liang, G.; Ronald, J.; Chen, Y.; Ye, D.; Pandit, P.; Ma, M. L.; Rutt, B.; Rao, J. Controlled Self-Assembling of Gadolinium Nanoparticles as Smart Molecular Magnetic Resonance Imaging Contrast Agents. *Angewandte Chemie International Edition* **2011**, 50 (28), 6283–6286. <https://doi.org/10.1002/anie.201007018>.

- (35) *Radiation Detectors for Medical Applications*; Tavernier, S., North Atlantic Treaty Organization, Eds.; NATO security through science series; Springer: Dordrecht, 2006.
- (36) González-Mancebo, D.; Becerro, A. I.; Corral, A.; Balcerzyk, M.; Ocaña, M. Luminescence and X-Ray Absorption Properties of Uniform  $\text{Eu}^{3+}:(\text{H}_3\text{O})\text{Lu}_3\text{F}_{10}$  Nanoprobes. *Nanomaterials* **2019**, 9 (8), 1153. <https://doi.org/10.3390/nano9081153>.
- (37) Homayoni, H.; Sahi, S.; Ma, L.; Zhang, J.; Mohapatra, J.; Liu, P.; Sotelo, A. P.; Macaluso, R. T.; Davis, T.; Chen, W. X-Ray Excited Luminescence and Persistent Luminescence of  $\text{Sr}_2\text{MgSi}_2\text{O}_7:\text{Eu}^{2+}$ ,  $\text{Dy}^{3+}$  and Their Associations with Synthesis Conditions. *Journal of Luminescence* **2018**, 198, 132–137. <https://doi.org/10.1016/j.jlumin.2018.02.042>.
- (38) A review of synthetic methods for the production of upconverting lanthanide nanoparticles <https://www.worldscientific.com/doi/epdf/10.1142/S1793545813300073> (accessed 2022 -03 -04). <https://doi.org/10.1142/S1793545813300073>.
- (39) Vreeland, E. C.; Watt, J.; Schober, G. B.; Hance, B. G.; Austin, M. J.; Price, A. D.; Fellows, B. D.; Monson, T. C.; Hudak, N. S.; Maldonado-Camargo, L.; Bohorquez, A. C.; Rinaldi, C.; Huber, D. L. Enhanced Nanoparticle Size Control by Extending LaMer's Mechanism. *Chem. Mater.* **2015**, 27 (17), 6059–6066. <https://doi.org/10.1021/acs.chemmater.5b02510>.
- (40) Kolthoff, I. M. Theory of Coprecipitation. The Formation and Properties of Crystalline Precipitates. *J. Phys. Chem.* **1932**, 36 (3), 860–881. <https://doi.org/10.1021/j150333a008>.

- (41) Chen, H.; Qi, B.; Moore, T.; Colvin, D. C.; Crawford, T.; Gore, J. C.; Alexis, F.; Mefford, O. T.; Anker, J. N. Synthesis of Brightly PEGylated Luminescent Magnetic Upconversion Nanophosphors for Deep Tissue and Dual MRI Imaging. *Small* **2014**, *10* (1), 160–168. <https://doi.org/10.1002/sml.201300828>.
- (42) Gan, Y. X.; Jayatissa, A. H.; Yu, Z.; Chen, X.; Li, M. Hydrothermal Synthesis of Nanomaterials. *Journal of Nanomaterials* **2020**, *2020*, e8917013. <https://doi.org/10.1155/2020/8917013>.
- (43) Hayashi, H.; Hakuta, Y. Hydrothermal Synthesis of Metal Oxide Nanoparticles in Supercritical Water. *Materials (Basel)* **2010**, *3* (7), 3794–3817. <https://doi.org/10.3390/ma3073794>.
- (44) Chen, H.; Rogalski, M. M.; Anker, J. N. Advances in Functional X-Ray Imaging Techniques and Contrast Agents. *Phys Chem Chem Phys* **2012**, *14* (39), 13469–13486. <https://doi.org/10.1039/c2cp41858d>.
- (45) Taroni, P.; Pifferi, A.; Torricelli, A.; Comelli, D.; Cubeddu, R. In Vivo Absorption and Scattering Spectroscopy of Biological Tissues. *Photochem. Photobiol. Sci.* **2003**, *2* (2), 124–129. <https://doi.org/10.1039/B209651J>.
- (46) Uzair, U. A PH Sensor for Non-Invasive Detection and Monitoring of PH Changes During Implant-Associated Infection Using X-Ray Excited Luminescence Chemical Imaging. *All Dissertations* **2020**.
- (47) Vinding, S. Light Pipe Design: How TIR & Refraction Come into Play. *VCC*, **2020**.



- (48) photomultiplier modules <https://www.sens-tech.com/index.php/products/photomultiplier-modules> (accessed 2022 -04 -24).
- (49) Camera Noise and Temperature Tutorial [https://www.thorlabs.com/newgrouppage9.cfm?objectgroup\\_id=10773](https://www.thorlabs.com/newgrouppage9.cfm?objectgroup_id=10773) (accessed 2022 -04 -24).
- (50) Badea, C. T.; Drangova, M.; Holdsworth, D. W.; Johnson, G. A. In Vivo Small-Animal Imaging Using Micro-CT and Digital Subtraction Angiography. *Phys Med Biol* **2008**, *53* (19), R319-350. <https://doi.org/10.1088/0031-9155/53/19/R01>.
- (51) Liu, Y.; Chen, W.; Wang, S.; Joly, A. G.; Westcott, S.; Woo, B. K. X-Ray Luminescence of LaF<sub>3</sub>:Tb<sup>3+</sup> and LaF<sub>3</sub>:Ce<sup>3+</sup>, Tb<sup>3+</sup> Water-Soluble Nanoparticles. *Journal of Applied Physics* **2008**, *103* (6), 063105. <https://doi.org/10.1063/1.2890148>.
- (52) Yang, Y.-C.; Tseng, W.-L. 1,4-Benzenediboronic-Acid-Induced Aggregation of Gold Nanoparticles: Application to Hydrogen Peroxide Detection and Biotin–Avidin-Mediated Immunoassay with Naked-Eye Detection. *Anal. Chem.* **2016**, *88* (10), 5355–5362. <https://doi.org/10.1021/acs.analchem.6b00668>.
- (53) Ma, X.; Chen, Z.; Kannan, P.; Lin, Z.; Qiu, B.; Guo, L. Gold Nanorods as Colorful Chromogenic Substrates for Semiquantitative Detection of Nucleic Acids, Proteins, and Small Molecules with the Naked Eye. *Anal. Chem.* **2016**, *88* (6), 3227–3234. <https://doi.org/10.1021/acs.analchem.5b04621>.
- (54) Mohamad, A.; Teo, H.; Keasberry, N. A.; Ahmed, M. U. Recent Developments in Colorimetric Immunoassays Using Nanozymes and Plasmonic Nanoparticles. *Critical*

*Reviews in Biotechnology* **2019**, 39 (1), 50–66.

<https://doi.org/10.1080/07388551.2018.1496063>.

- (55) Zengin, A.; Tamer, U.; Caykara, T. A SERS-Based Sandwich Assay for Ultrasensitive and Selective Detection of Alzheimer's Tau Protein. *Biomacromolecules* **2013**, 14 (9), 3001–3009. <https://doi.org/10.1021/bm400968x>.
- (56) Ni, J.; Lipert, R. J.; Dawson, G. B.; Porter, M. D. Immunoassay Readout Method Using Extrinsic Raman Labels Adsorbed on Immunogold Colloids. *Anal. Chem.* **1999**, 71 (21), 4903–4908. <https://doi.org/10.1021/ac990616a>.
- (57) Smolsky, J.; Kaur, S.; Hayashi, C.; Batra, S. K.; Krasnoslobodtsev, A. V. Surface-Enhanced Raman Scattering-Based Immunoassay Technologies for Detection of Disease Biomarkers. *Biosensors (Basel)* **2017**, 7 (1), 7. <https://doi.org/10.3390/bios7010007>.
- (58) Liu, L.; Hao, Y.; Deng, D.; Xia, N. Nanomaterials-Based Colorimetric Immunoassays. *Nanomaterials* **2019**, 9 (3), 316. <https://doi.org/10.3390/nano9030316>.
- (59) Ou, X.-Y.; Guo, T.; Song, L.; Liang, H.-Y.; Zhang, Q.-Z.; Liao, J.-Q.; Li, J.-Y.; Li, J.; Yang, H.-H. Autofluorescence-Free Immunoassay Using X-Ray Scintillating Nanotags. *Anal. Chem.* **2018**, 90 (11), 6992–6997. <https://doi.org/10.1021/acs.analchem.8b01315>.
- (60) Kim, K. R.; Han, Y. D.; Chun, H. J.; Lee, K. W.; Hong, D.-K.; Lee, K.-N.; C. Yoon, H. Encapsulation-Stabilized, Europium Containing Nanoparticle as a Probe for Time-Resolved Luminescence Detection of Cardiac Troponin I. *Biosensors* **2017**, 7 (4), 48. <https://doi.org/10.3390/bios7040048>.

- (61) Fang-Yen, C.; Alkema, M. J.; Samuel, A. D. T. Illuminating Neural Circuits and Behaviour in *Caenorhabditis Elegans* with Optogenetics. *Phil. Trans. R. Soc. B* **2015**, *370* (1677), 20140212. <https://doi.org/10.1098/rstb.2014.0212>.
- (62) Corsi, A. K. A Transparent Window into Biology: A Primer on *Caenorhabditis Elegans*. *WormBook* **2015**, 1–31. <https://doi.org/10.1895/wormbook.1.177.1>.
- (63) Liu, J.; Ward, A.; Gao, J.; Dong, Y.; Nishio, N.; Inada, H.; Kang, L.; Yu, Y.; Ma, D.; Xu, T.; Mori, I.; Xie, Z.; Xu, X. Z. S. C. *Elegans* Phototransduction Requires a G Protein–Dependent CGMP Pathway and a Taste Receptor Homolog. *Nat Neurosci* **2010**, *13* (6), 715–722. <https://doi.org/10.1038/nn.2540>.

## CHAPTER TWO

### IMPRESSIVELY PRINTING PATTERNS OF GOLD AND SILVER NANOPARTICLES

*Much of the material in this chapter was published as a journal article: Ameer, F. S.; Ranasinghe, M.; Varahagiri, S.; Benza, D. W.; Hu, L.; Willett, D. R.; Wen, Y.; Bhattacharya, S.; Chumanov, G.; Rao, A. M.; Anker, J. N. Impressively Printing Patterns of Gold and Silver Nanoparticles. Nano Select 2021, 2 (12), 2407–2418. <https://doi.org/10.1002/nano.202000278>.*

#### 2.1. Abstract

The optical and chemical properties of gold and silver nanoparticles make them useful for many applications, including surface-enhanced spectroscopy-based biosensors, photostable colorants, enhanced photovoltaic, and nanoscale optical elements. We report a simple technique to generate patterns of gold and silver nanoparticles with controlled shape and shape-dependent optical properties using metal stamps and glucose deposit to impress them onto a glass substrate. The pressure flattens the nanoparticles, converting initially spherical nanoparticles into discs with reduced height and increased diameter. This deformation causes their localized surface plasmon resonance wavelength to red-shift. Nanoparticles were characterized by electron microscopy, atomic force microscopy, and darkfield optical scattering spectroscopy. The deformed nanoparticle patterns had a lateral resolution limited by the nanoparticle diameter (single particles are partly flattened, only where they contact the stamp). The method also transfers the stamp's topography, with smooth stamps generating flattened nanoparticles with uniform height, and small changes in stamp height are evident in the nanoparticle height and scattering wavelength. Patterning with glucose deposits generated circle patterns, and

nanoparticle height decreased when they go away from the glucose deposit. The height changes are evident in darkfield and atomic force microscopy images. Also, the method allows facile removal of undeformed nanoparticles using scotch tape, and patterns of deformed nanoparticles can be transferred to a flexible polymer film. The patterning process is simple and inexpensive. It can be performed by hand for demonstrations or artistic applications, with a controlled force for plasmonics research, and potentially automated on reel-to-reel presses for large-scale production.

## **2.2. Introduction**

Light irradiating plasmonic gold and silver nanoparticles (AuNPs and AgNPs) are strongly absorbed and scattered at wavelengths that depend upon the nanoparticle's size, shape, and the refractive index of its surroundings. These optical properties arise from optically-driven resonant oscillations of conduction electrons in the nanoparticle, termed as the localized surface plasmon resonance (LSPR). The shape and refractive index dependent properties are explained briefly in Chapter 1, section 1.1 of this Dissertation. Plasmonic nanoparticles are used in a variety of applications, including as labels in immunoassays,<sup>2-3</sup> agents for photothermal therapy,<sup>4,5</sup> lithographic fabrication,<sup>6-8</sup> photostable colorants for printing,<sup>9,10</sup> staining glass windows,<sup>11,12</sup> coloring coins,<sup>11,12</sup> making anti-counterfeit labels,<sup>13,14</sup> components in nano-optical switches and waveguides,<sup>15,16</sup> meta-materials with negative refractive indices, catalysis,<sup>17,18</sup> and biosensors and labels based on surface-enhanced spectroscopies.<sup>19-24</sup> While considerable effort has been directed towards the synthesis of noble metal nanoparticles with

controlled size and shape, printing patterns of metal nanoparticles with different shapes on a solid substrate remains challenging.

To form plasmonic nanoparticle patterns, top-down lithographic approaches are commonly used. For example, ion beam etching can be used to etch away a film into arrays of nanoparticles with a precisely controlled shape and pattern.<sup>25</sup> Once a master pattern is formed using slow lithographic approaches, it can then be used to make sub-masters, which can be used as stamps in nanoimprint lithography via contact printing<sup>26</sup> or chemical etching.<sup>27</sup> Such nanoimprint lithography can be made compatible with reel-to-reel processes for rapid reproduction over large areas.<sup>28</sup> However, generating the master stamp is slow and expensive, and the remaining processes require multiple steps such as heating the substrate to an appropriate temperature, performing photolithography exposure/baking/development steps, and/or vapor depositing gold or silver. Several other techniques have been developed to pattern nanoparticles using pulsed laser writing,<sup>29</sup> nanosphere lithography (also called colloidal lithograph)<sup>30</sup>, and others. However, these are still relatively slow and require processes such as vapor deposition, which are rarely available outside of academic or industrial laboratories. Although these techniques allow a careful control over nanoparticle height and aspect ratio through the vapor deposition thickness, they are ill-suited for studying the effects of nanoparticle shape while conserving volume or for applications in low-resource lab settings.

In our previous study, we described a simple technique to alter the shape of AgNPs by rolling a glass tube over them with a controlled force to compress them mechanically. The resulting shape change induces a red-shift in the LSPR scattering

spectrum and exposes new surface areas.<sup>31</sup> Herein, we report an expansion of our previous work that shows the versatility of the deformation technique by using a stamp to create complex and high-fidelity patterns. We also show that gold nanoparticles and silver nanoparticles can be deformed using a rolling pin and/or stamp. This is important for long-term applications because gold, unlike silver, does not oxidize. Additionally, we show that the approach is simple enough to be performed by hand for minting, printing, crafting applications, and educational activities such as the scientific outreach programs. To provide more uniformity, mechanical systems with fixed force are used. Finally, we show how to isolate the pattern on a glass slide and transfer the nanoparticles to flexible substrates.

## **2.3. Methods**

### *2.3.1. Methods and Instrumentation*

All chemical reagents were obtained from Sigma Aldrich and used as received. All aqueous solutions were prepared using deionized (DI) water (18.2 M $\Omega$  cm). Poly(4-vinylpyridine) (PVP) (Mw = 60,000 Da) was prepared by dissolving a weighed quantity of PVP into ethanol. Indium–tin oxide (ITO) coated glass (100  $\Omega$  cm<sup>-1</sup>) was purchased from Delta Technologies, Limited. Samples were characterized using an enhanced darkfield transmission optical microscope (Olympus BX41) equipped with a hyperspectral imaging spectrophotometer (CytoViva Hyperspectral Imaging System (HSI), Auburn, AL). Scanning electron microscopy (SEM) images were collected using a Hitachi SEM-4800 field emission (Hitachi, Japan) electron microscope operating at an

accelerating voltage of 15 kV and an average working distance of 8.4 mm. The average nanoparticle size and particle size distribution were obtained using the ImageJ software. Alteration of the height of particles was measured using a AIST-NT SmartSPM in non-contact mode with HQ:NSC14/AL BS cantilevers from Mikro-Masch with spring constant of ca. 5.0 N m<sup>-1</sup>. Absorbance spectra were collected using a Shimadzu UV-2501 PC spectrometer.

### 2.3.2. *Poly(4-vinylpyridine) functionalization of glass substrate*

Both ITO-coated and normal glass substrates were cleaned by sonication in nanopure water for 15 minutes followed by drying inside a desiccators and plasma treating for 10 minutes (Harrick Plasma Cleaner PDC – 32G). The cleaned glass substrates were poly(4-vinylpyridine) (PVP) functionalized according to a previously reported method.<sup>32</sup> After modification with PVP, substrates were thoroughly rinsed in reagent ethanol to remove all weakly bound polymer molecules leaving only a monolayer directly adhered to the surface. Next, the PVP modified substrates were annealed at 120°C under ambient atmosphere for a few hours. For the experiments, both ITO-coated and normal glass substrates were used. No significant impact on experimental results was found with either because the NPs are deformed by the pressure exerted by the rolling pin, which is independent of the nature of the substrate. However, ITO-coated glass substrates were mostly used for scanning electron microscopy due to their electrical conductivity.



### 2.3.3. *AuNPs and AgNPs Synthesis*

AuNPs were prepared using the seeded growth method.<sup>33</sup> Briefly, a solution of 2.2 mM sodium citrate in 150 mL of nanopure water was heated in a three-necked round-bottom flask attached to a condenser for 15 minutes under vigorous stirring. After boiling had commenced, 1.0 mL of 25.0 mM HAuCl<sub>4</sub> was injected. After appearance of a deep red color, which indicates the formation of gold seeds, the mixture was boiled and stirred for another 10 minutes. Next, the mixture was cooled to 90°C and 1.0 mL of 25.0 mM HAuCl<sub>4</sub> was injected. After another 30 minutes the reaction was completed. This process was repeated twice. Then, the sample was diluted by extracting 55 mL of sample and adding 53 mL of nanopure water and 2.0 mL of 60.0 mM sodium citrate. This solution was then used as a seed solution and the process was repeated until the AuNPs had grown to the desired size. The AuNPs with average diameter of ~94 nm exhibited a maximum extinction wavelength of 561 nm (Figure 2.1). We also used commercially purchased AuNPs (EM.GC100, BBI Solutions, Anaheim, CA, USA) with average diameter of ~72 nm that exhibited a maximum extinction wavelength of 520 nm (Figure 2.1).

AgNPs were synthesized using the hydrogen reduction method developed by Evanoff and Chumanov<sup>33</sup> Briefly, Ag<sub>2</sub>O was added to deionized water in a ratio of 1.0 gL<sup>-1</sup> in a quartz reaction vessel. Next, 1.0 mM sodium silicate was added to promote stabilization of the resulting AgNPs. The mixture was then shaken well before connecting to the condenser and a hydrogen line. A heating mantle was placed under the vessel and its contents heated and maintained at 70°C with constant stirring. Once the temperature equilibrated, the vessel was flushed with H<sub>2</sub> (99.9% purity) and pressurized to

10 psi. Hazard: over pressurizing or using a defective vessel may result in explosion and cause severe injuries. Within 10–15 seconds of the initial pressurization, the contents of the vessel turned faint yellow in color indicating the formation of metallic silver particles 10–15 nm in diameter. As the reaction progresses, aliquots can be taken through the spout. Removing the aliquots from the reducing environment stops further growth of the particles. Likewise, the reaction can be stopped at any time simply by releasing the gas from the vessel. In this way, control of the particle diameter is purely a function of total reaction time. AgNPs with 97 nm average diameter had a maximum extinction wavelength of 502 nm (Figure 2.1).

#### *2.3.4. Deposition of nanoparticles on PVP functionalized ITO glass slides*

To prepare the samples for deformation, both colloidal AuNPs (72 nm and 94 nm) and AgNPs (97 nm) were diluted with deionized water to an optical density (O.D.) of 1 (using wavelength at dipole maximum and 1 cm path length). This absorbance corresponds to  $\sim 2.3 \times 10^{12}$  particles per mL for 97 nm AgNPs and  $\sim 2.6 \times 10^{10}$  particles per mL for 72 nm AuNPs and  $\sim 8.3 \times 10^9$  particles per mL for 94 nm AuNPs based upon a previous study counting the number of particles absorbed onto a surface with well-known dimensions and measuring decrease in optical density of nanoparticle solution.<sup>32</sup> PVP coated glass substrates were immersed in the diluted aqueous suspension of colloidal either AuNPs or AgNPs overnight at room temperature to form a monolayer of nanoparticles, then rinsed with reagent ethanol and dried overnight at room temperature in a desiccator connected to a vacuum pump. This leads to a well-dispersed configuration of colloidal either AuNPs or AgNPs on the substrate surface.

### *2.3.5. Mechanical deformation of nanoparticles*

Nanoparticles deposited on a glass slide can be manually deformed by rolling a simple glass stirring rod over them while applying downward pressure (Figure 1). The pressure was be more easily applied by replacing the stirring rod with a simple rolling pin (a ¼ inch diameter glass tube with a metal rod through it). For controllable and uniform deformation, the rolling pin was attached to an ESM 303 mechanical test stand equipped with a 1000 N Mark-10 Force gauge with computer-applied force. Nanoparticles immobilized on a PVP functionalized ITO glass substrate were then clamped to a linear motorized stage LTS 300 (Thorlabs, City State). The rolling pin was placed on one end of the slide to begin with. Mechanical force was applied by the ESM 303 and the stage was moved forward and back to roll the glass tube over the length of the glass substrate 10 times (Figure 2.3). Our previous study showed a similar effect with a single roll.<sup>34</sup> However, single rolled deformed particles appear to have sharper edges compared to the particles deformed by rolling the glass rolling pin 10 times.<sup>34</sup> The applied force was varied from 0 to 50 N with the number of times the slide was rolled and rolling speed (500  $\mu\text{m s}^{-1}$ ) were kept consistent for each experiment. The glass tubes were cleaned several times using acetone and distilled water prior to use.

### *2.3.6. Dark field optical imaging*

Optical scattering from patterned AuNPs and AgNPs was observed with a Nikon TE2000 microscope in a transmission dark field imaging configuration using a 0.95-0.8 numerical aperture (NA) condenser and 100X oil immersion objective with a variable aperture stopped down to just below 0.8 NA. Images were acquired on a Nikon D90

camera; all parameters of the camera were controlled by Camera Control Pro2 software (Nikon Instruments Inc., Melville, NY, USA).

#### *2.3.7. Hyperspectral darkfield microscopy*

Both undeformed and deformed AuNPs and AgNPs on PVP-functionalized glass substrates were examined using enhanced dark field transmission optical microscope (Olympus BX41) equipped with hyperspectral imaging spectrophotometer (CytoViva Hyperspectral Imaging System (HSI), Auburn, AL). The concentric imaging spectrophotometer was used to record optical scattering spectra from visible and near infrared wavelengths (400-1000 nm) at a spectral resolution of 1.5 nm with 10 nm scan size and pixel size 25 nm. The customized hyperspectral imager (mounted on a microscope and controlled by Environment for Visualization software) was extracted with complete spectral information from single or multiple pixels. All images were acquired using a 40X oil with iris objective at identical gain (gain = 5) and exposure time (0.1 ms).

#### *2.3.8. Atomic force microscopy (AFM)*

AFM images were collected for patterned AuNPs and AgNPs adsorbed on PVP functionalized ITO glass substrates using an AIST-NT SmartSPM in non-contact mode with HQ:NSC14/AL BS cantilevers from Mikro-Masch with spring constant of ca. 5.0 N m<sup>-1</sup>. These cantilevers had an uncoated tip radius of about 8 nm with a 40° full tip cone angle. AFM image processing was carried out with AIST-NT SPM Control Software. Polynomial background subtraction and line fit corrections were employed in some AFM

images. Histograms of undeformed and deformed NPs sizes were based on statistical analysis of ~100 nanoparticles to calculate average size with standard deviation.

## **2.4. Results and Discussion**

### *2.4.1. Manual and force-controlled nanoparticle deformation*

Gold and silver nanoparticles can be deformed by applying pressure to them. We had previously demonstrated this with silver nanoparticles using a constant pressure device. Here, we extended to more chemically inert gold nanoparticles and showed that this could be done by hand. Spherical AuNPs of diameters 72 and 94 nm, and AgNPs of diameter 97 nm were used for preparing patterned nanoparticle surfaces (Figure 2.1).

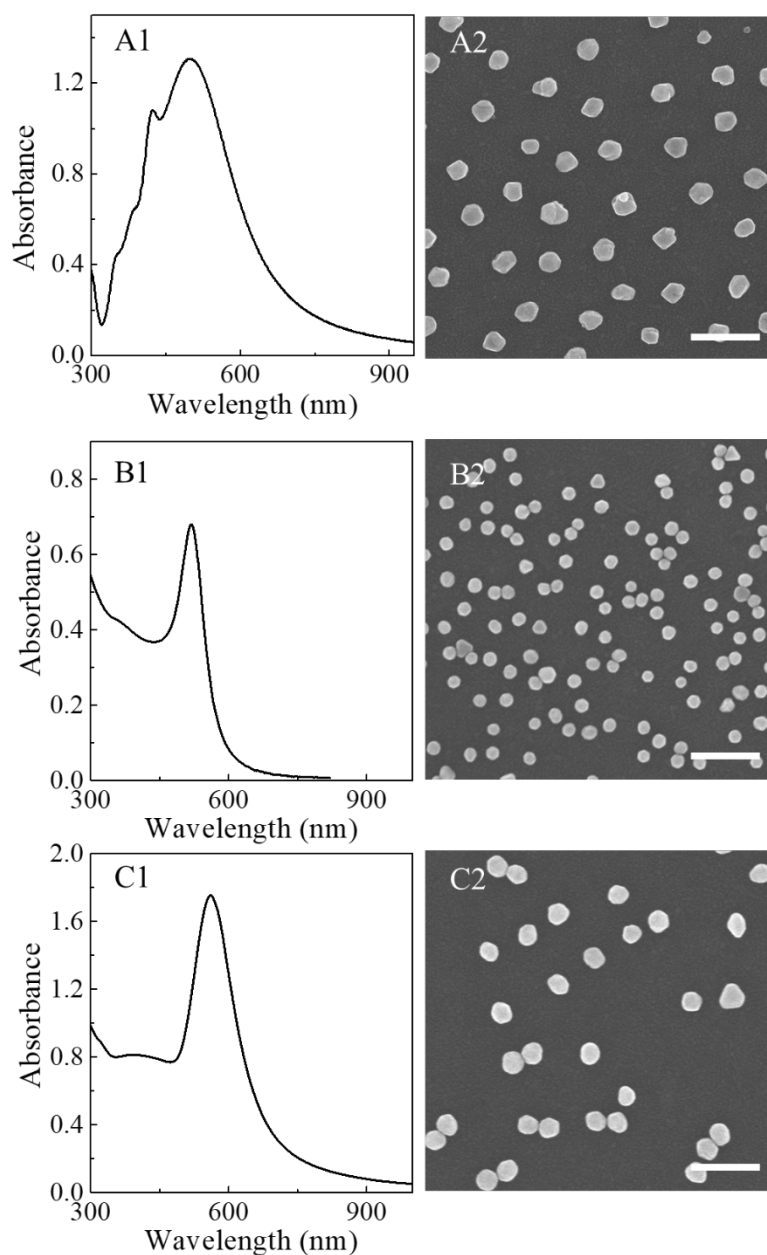


**Figure 2. 1: Characterization of (A) 97 nm diameter AgNPs, (B) 72 nm diameter AuNPs (B), and (C) 94 nm diameter AuNPs using UV-vis spectroscopy (A1, B1, and C1), and scanning electron microscopy (A2, B2, and C2). The scale bar in each SEM image is 300 nm. Taken with permission of ref 1.**

Initially, a colloidal AuNP suspension was deposited onto a PVP functionalized glass substrate, and the nanoparticles were deformed by manually rolling a glass rod over them (Figure 2.2A). When these AuNPs (before deformation) were illuminated with white light, they appeared as bright green diffraction-limited points under a dark field microscope. After deformation, however, these nanoparticles appeared red-colored in the dark field image because their shape had changed from approximately spherical to flattened discs, which altered the conditions for localized surface plasmon resonance.

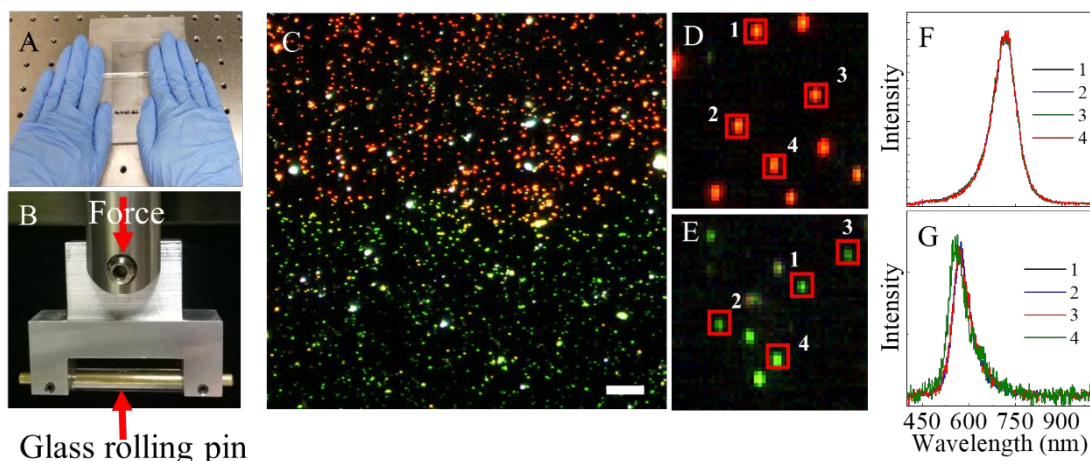


**Figure 2. 2:** (A) Photograph of AuNPs on a glass slide being manually deformed with a glass stir rod. A glass substrate coated with AuNPs is placed on a slide holder fixed to the optical bench to hold it steady, and a glass stirring rod rolls over the AuNPs to flatten them. (B) A rolling pin, comprising of a 1/4" glass tube with a metal pin through it, is held in a mechanical test system fixture and rolled over particles deposited on a PVP functionalized ITO glass substrate. (C) Dark field microscopy image showing both undeformed AuNP (bottom, green) and deformed AuNPs (top, red) on a PVP functionalized glass substrate. 4X zoom in images of (D) deformed and (E) undeformed AuNPs. Representative dark field single AuNP scattering spectra from (F) deformed and (G) undeformed AuNPs. The squared AuNPs in figures (D) and (E) produced the spectra shown in (F) and (G), respectively. Scale bar is 20  $\mu$ m. Spectra are offset for clarity. Taken with permission of ref 1.

Although nanoparticles can be easily deformed manually, this method suffers from two major drawbacks: (i) the compressive force exerted on the nanoparticles may not be uniform when the glass rod is manually rolled over the nanoparticles, and (ii) if the

glass rod is not held properly, it could slide across the surface instead of rolling over it. To apply a consistent and controllable compressive force to deform the nanoparticles, we used a material testing stand (Model ESM 303, Mark-10 Corporation, Copiague NY, USA) which pressed a glass "rolling pin" (a  $\frac{1}{4}$  inch glass tube with a metal pin through it, Figure 2.2B) against a nanoparticle-coated sample attached to a computer-controlled stage.<sup>31</sup> We deposited AuNPs onto a PVP functionalized glass substrate and mechanically deformed them using the rolling pin (Figure 2.3).



**Figure 2. 3: Photograph showing the deformation technique employed in this study. The rolling pin was placed on one end of the slide to begin with. A mechanical force was applied by the ESM 303 as the glass tube was rolled over the length of the glass substrate 10 times. The applied force was varied from 0 to 50 N, and a constant rolling speed of 500  $\mu\text{m/s}$  was used in each experiment. The glass tube was cleaned several times using acetone and distilled water prior to use. Taken with permission of ref 1.**



The colloidal AuNPs ( $\sim 72$  nm diameter as determined by SEM) dispersion used in this experiment exhibited a strong extinction peak at around 520 nm (Figure 2.1). A glass slide with undeformed and deformed AuNPs regions was imaged using dark field microscopy; the undeformed particles at the bottom of the slide appeared as bright green diffraction-limited spots, while the deformed particles at the top of the slide appeared red as shown in Figure 2.2C. Dark field hyperspectral images showed single nanoparticles as diffraction-limited spots for both the deformed (Figure 2.2D) and undeformed (Figure 2.2E) AuNPs. In Figures 2.2D and E, four representative particles are labeled 1–4, and their corresponding single-particle scattering spectra are shown in Figures 2.2F and G, respectively. These results indicate that individual nanoparticles in the ensemble have similar spectra to each other and that deformation causes a significant red-shift from  $\sim 565$  nm to  $\sim 760$  nm. Our previous work showed similar results with AgNPs; Figure 2.4 shows a comparison.<sup>31</sup>

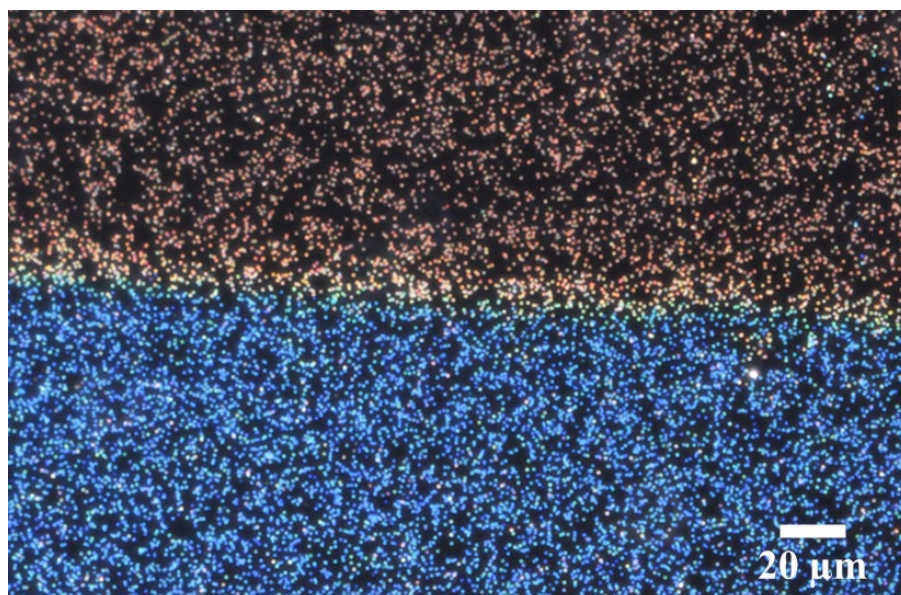


**Figure 2. 4: Dark field microscope image showing both deformed (top-red) and undeformed (bottom-blue) regions of Ag NPs on a glass/ITO slide. Taken with permission of ref 1.**

The undeformed (Figure 2.5A1) and deformed AuNPs (Figures 2.5B1 and C1) were imaged using SEM. Figures 2.5A2, B2 and C2 show the corresponding histograms, which revealed the effective nanoparticle diameter for the undeformed and deformed AuNPs (calculated from the area of each particle assuming a disc shape). The SEM images revealed that the AuNPs diameter and shapes varied as the applied load increased. The unmodified AuNPs had a roughly spherical shape with a mean diameter of 72 nm and a 6.9% of the coefficient of variation (CV), Figure 2.5A. Rolling over the particles caused them to deform from spheres into discs and their mean diameters to increase in a load-dependent manner, increasing to 173 nm (CV-5.8%) with a 30 N load and 183 nm (CV-13%) with a 50 N load.

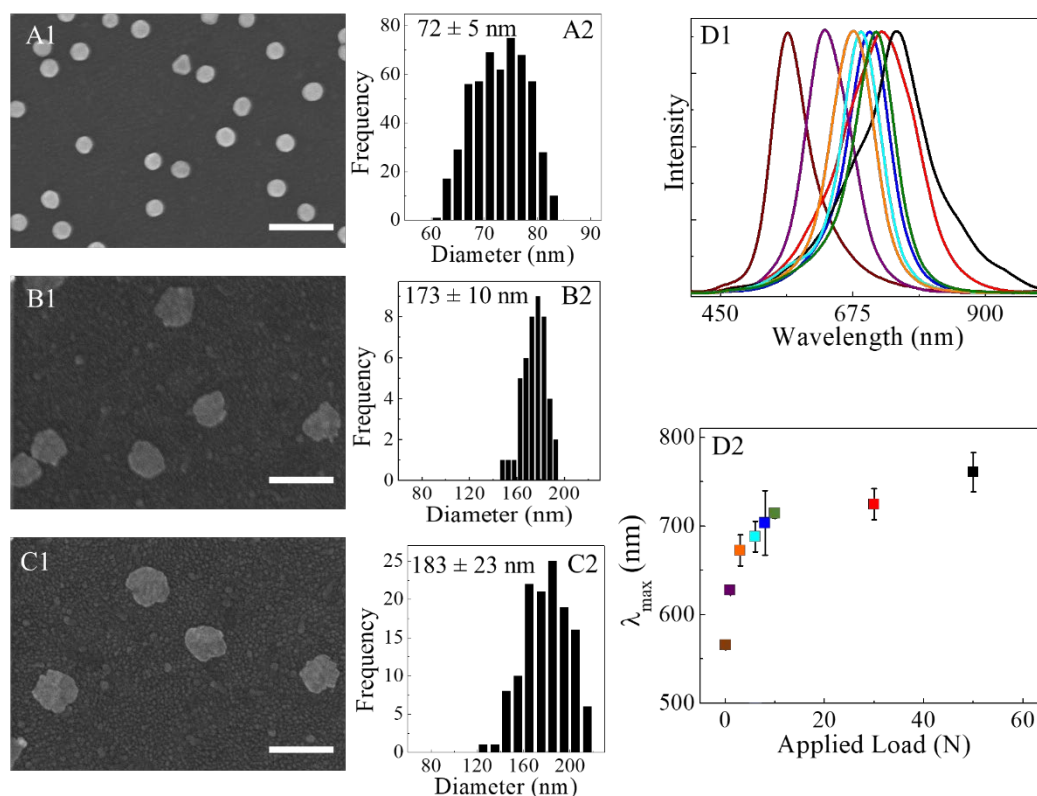


**Figure 2. 5: (Left) SEM images showing effect of applied load (A1) 0 N, (B1) 30 N, and (C1) 50 N on deformation of AuNPs. All images have the same magnification (Scale bar is 300 nm). Histograms on the right of each SEM image show particle diameter distributions for (A2) undeformed and (B2, C2) deformed AuNPs. The sample preparation and SEM imaging procedure are described in the Experimental Section. The inset numbers show estimated mean diameter and uncertainty from a Gaussian fit. (D1) Average dark field single nanoparticle scattering spectra of one hundred undeformed and deformed AuNPs as a function of applied load (0, 1, 3, 5, 8, 10, 30, 50 N). The spectra are scaled to the same maximum intensity. (D2) Experimental data on the evolution of LSPR peak position, before and after deformation, as a function of applied load. Figure 2.6 shows a comparison with our previous AgNP study. Taken with permission of ref 1.**

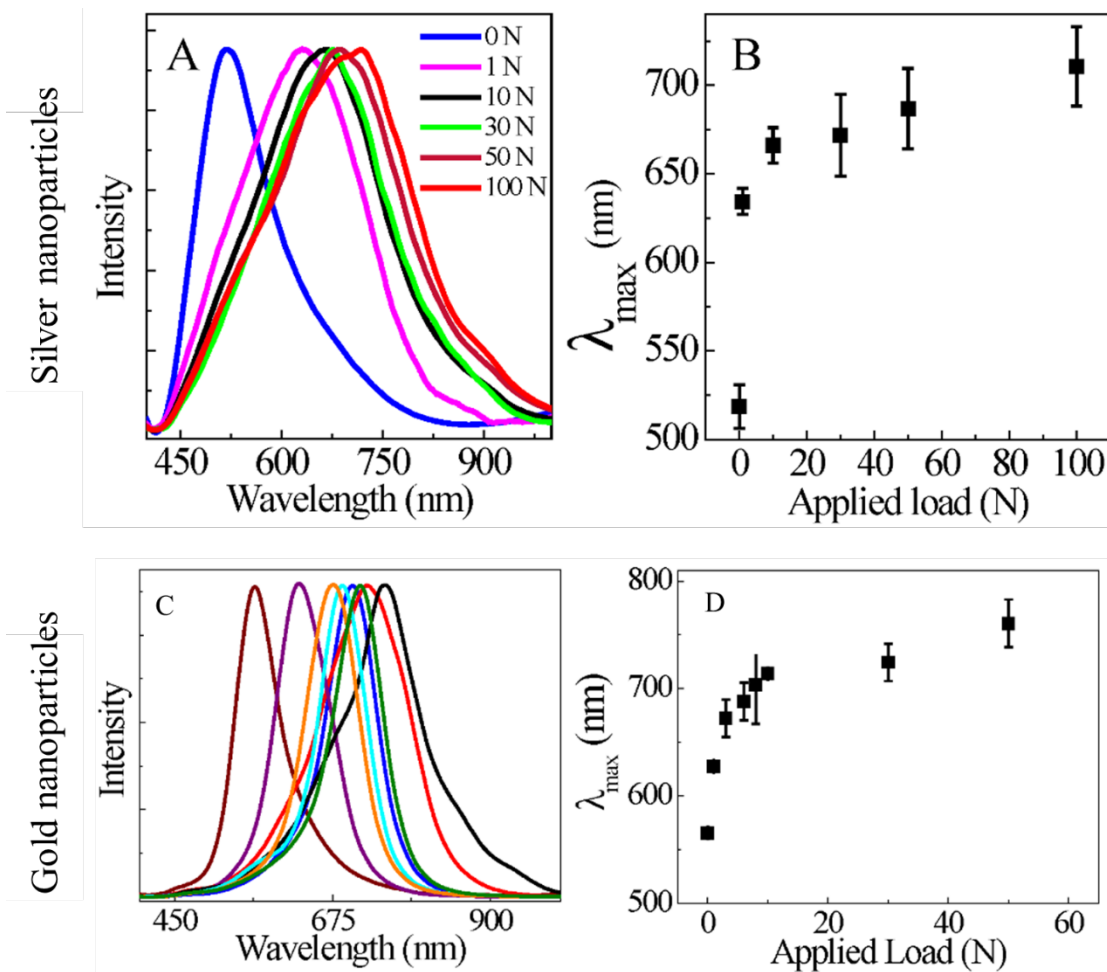


**Figure 2. 6: Average dark field single nanoparticle scattering spectra of un-deformed and deformed (A) AgNPs and (C) AuNPs as a function of applied load. The spectra are scaled to the same maximum intensity. Experimental data on the evolution of LSPR peak position, before and after deformation of (B) AgNPs and (D) AuNPs as a function of applied load. Panels A and B are adapted from reference.<sup>31</sup> Taken with permission of ref 1.**

In our previous study, the deformation of AgNPs produced mostly ellipse-shaped nanodiscs<sup>35</sup> with some sharp features, while the deformed AuNPs produced in this study were more circular nanodiscs according to the SEM images. This difference in shapes is attributed to the high crystallinity nature of AgNPs<sup>35</sup>, which may have resulted in different deformation along different crystalline axes.<sup>36</sup> In contrast, the AuNPs exhibited smaller crystal domain sizes with no preferred deformation axes. Further, at lower

particle concentrations where individual particles could be resolved, the ellipse-shaped silver nanodiscs produced show polarization-dependent scattering properties (Figure 2.7). The random orientation and polarization dependence, along with random nanoparticle positioning and color, are important for making unique irreproducible patterns for anti-counterfeiting/tamper-proof applications for uncirculated mint coins and electronic components legal documents, etc.<sup>37–39</sup> For these applications, stamp patterning is helpful for rapidly identifying a region of interest with the nanoparticles on it. After deformation, both Ag and AuNPs remain well-separated (except at higher concentrations where particles begin to touch).

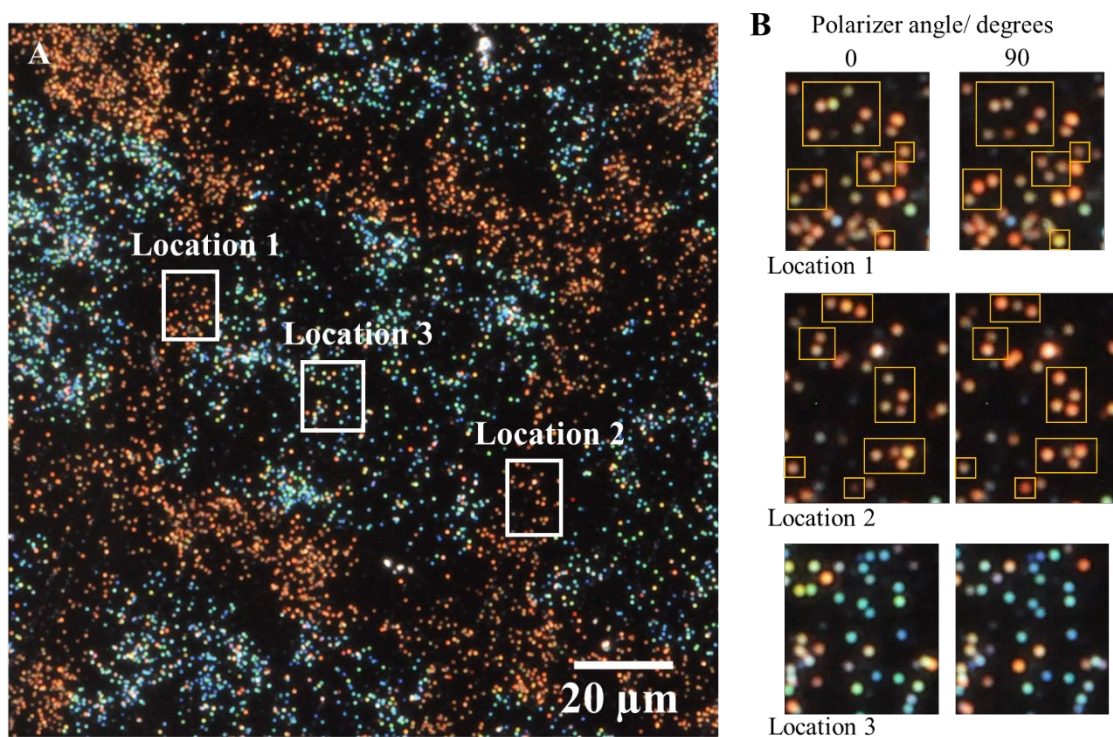


**Figure 2. 7:** (A) Dark field microscope image of patterned/deformed Ag NPs by placing TEM grid on NPs and mechanically pressing them. (B) Dark field microscope images (Zoomed in) of location 1,2 and 3 by placing polarizer at 0 (zero) and 90 degrees of angle. NPs marked using yellow color boxes show polarization dependent scattering properties. Some of the NPs at location 3 shows shape and orientation dependent scattering. Taken with permission of ref 1.

We next studied the LSPR properties of the undeformed and deformed AuNPs by recording the dark field single nanoparticle scattering spectra for undeformed and deformed AuNPs on the glass substrate, as shown in Figure 2.5D1. The LSPR peak red-shifts and broadens with increasing applied load due to the increasing AuNP diameter and associated change in the aspect ratio (diameter/height). An overall LSPR shift of  $\sim 195$  nm was observed when the applied load increased from 0 to 50 N, implying that the LSPR could be systematically red-shifted with increasing force and shape change. The data in Figure 2.5D2 illustrate the correlation between the maximum LSPR wavelength of undeformed and deformed AuNPs and applied load. The maximum LSPR wavelength increases rapidly with load for applied loads below between 0 and 10 N, after which the rate of red-shift decreases when the applied load is varied from 10 to 50 N. This is in part due to a slower increase in the nanoparticle diameter relative to the initial NP diameter. Similarly, the glass rolling pin deforms slightly (on a  $< 100$  nm scale) with pressure, increasing the contact area with adjacent particles and glass substrate, thus exerting less force on each particle.<sup>31</sup> In addition to the deformation not scaling with force, the spectral shift is not expected to scale with force either because the phase of the incident light varies across the AuNPs, requiring consideration of dynamic depolarization and retardation effects.<sup>40–44</sup> Similar to preparing nanodiscs, nanorods can be prepared. A preliminary study carried out to prepare nanorods is described in chapter 6.

#### *2.4.2. Stamping deformation pattern*

To rapidly generate patterns of deformed plasmonic nanoparticles, a stamp can be placed between the rolling pin and nanoparticles. To show this principle, we used TEM



grids (SPI supplies, Crosby, TX) and VACCO grids (precision etched parts, South El Monte, CA) as stamps. TEM grids have a grid pattern on which samples are typically deposited prior to imaging, with the grid designed to select sample areas rapidly; these grids have uniform heights and precise boundaries, are relatively inexpensive, and can be bought in large quantities. VACCO grids are designed as demo pieces to show the capability to etch patterned metal substrates for a wide range of applications, from physical filters to fluid control products (regulators and valves). The VACCO grids were larger than the TEM grids, had a rougher surface, and were reused several times in our experiments. We first performed the experiment by manually rolling a glass stir bar over either TEM or VACCO grids to press it into the silver nanoparticle covered glass slide. For the relatively large VACCO grid, the deformation pattern can be observed clearly by eye (Figure 2.8). The sample in Figure 2.8 was made and photographed during a public outreach event, Upstate !MAGINE Greenville, South Carolina, which exemplifies the simplicity of the technique and its potential applicability to science demos and potentially for printing and artistic applications.

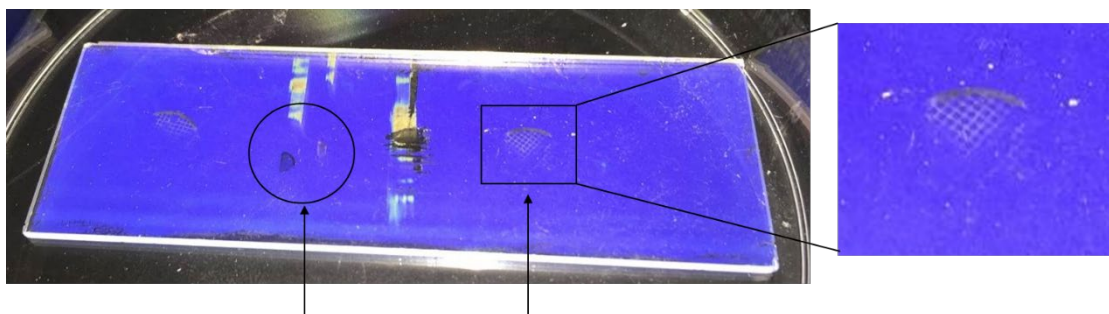


**Figure 2. 8: Photographs of glass slide coated with AgNPs, with stamp patterns formed by manually pressing either at TEM grid or VACCO grid onto the slide with a rolling pin. The blue color is a result of light scattering by the undeformed particles, and the red regions represent scattered light by the deformed particles. The stamping and imaging were performed by volunteers during the Upstate EMAG!NE public education outreach event in Greenville, South Carolina. The vertical streaks are the scratched marks caused by the rolling rod on the microscope slide. Taken with permission of ref 1.**

For more precise work, the mechanical test system was used to apply a uniform force. Figure 2.9 shows how deformed and undeformed areas can be easily distinguished by dark field microscopy, SEM (Figure 2.10A), and AFM (Figure 2.10B1 and B2). Nanoparticles in the deformed regions were disc-shaped and had a larger diameter and smaller height than the undeformed, approximately spherical (or polygonal) nanoparticles. The boundary between deformed and undeformed nanoparticles was very close to a straight line; occasionally, a nanoparticle was found on the boundary itself and was deformed only where the grid was in contact with a region of the particle that remained unflattened (e.g., Figures 2.9B3). These observations were confirmed by AFM topographic scanning (Figure 2.10C1-C3) using AgNPs. The zoom-out AFM image ( $20 \times 20$  microns) shows that under the mechanical force, the original polygonal AgNPs ( $\sim 97$  nm) were uniformly deformed into flattened particles ( $\sim 24$  nm height, Figure 2.11). Interestingly, AgNPs located at the border between original AgNPs and deformed AgNPs were partially deformed, with one part of the particle essentially unchanged, while the part under pressure was flattened (larger diameter and reduced height)





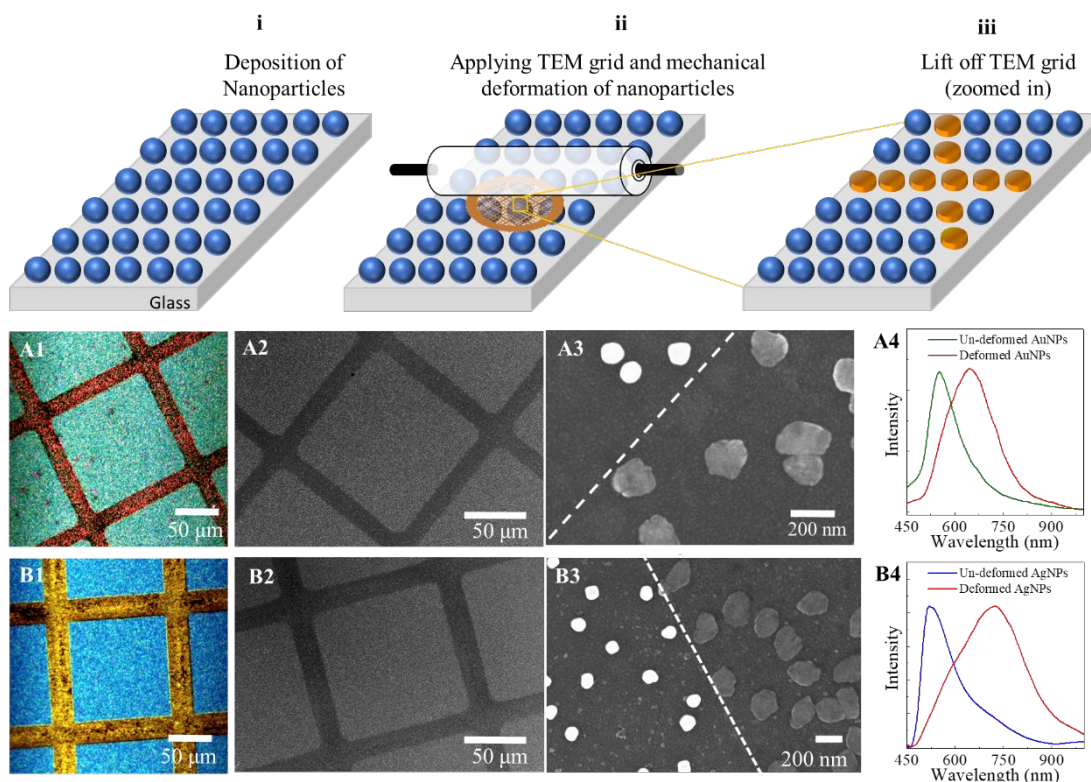


**Figure 2. 9: Patterning with TEM grid pattern. (i-iii) Schematic illustration of the principle of the patterning technique. The patterning technique involves three steps: (i) Deposition of nanoparticles on PVP functionalized glass slides, (ii) Patterning of selected nanoparticles via mechanical deformation using a TEM grid as a stamp (not drawn to scale), and (iii) Lift-off of TEM grid from sample surface, which leaves deformed nanoparticles in shape of the TEM-grid pattern. Images of Au (middle row) and Ag (bottom row) NPs deformed under a copper TEM-grid pattern. (A1, B1) Hyperspectral dark field images and (A2, A3, B2, B3) SEM images. Both undeformed and deformed regions were marked using a dashed line. (A4, B4) Representative average dark field scattering spectrum from un-deformed and deformed Au and Ag NPs regions, respectively. Taken with permission of ref 1.**

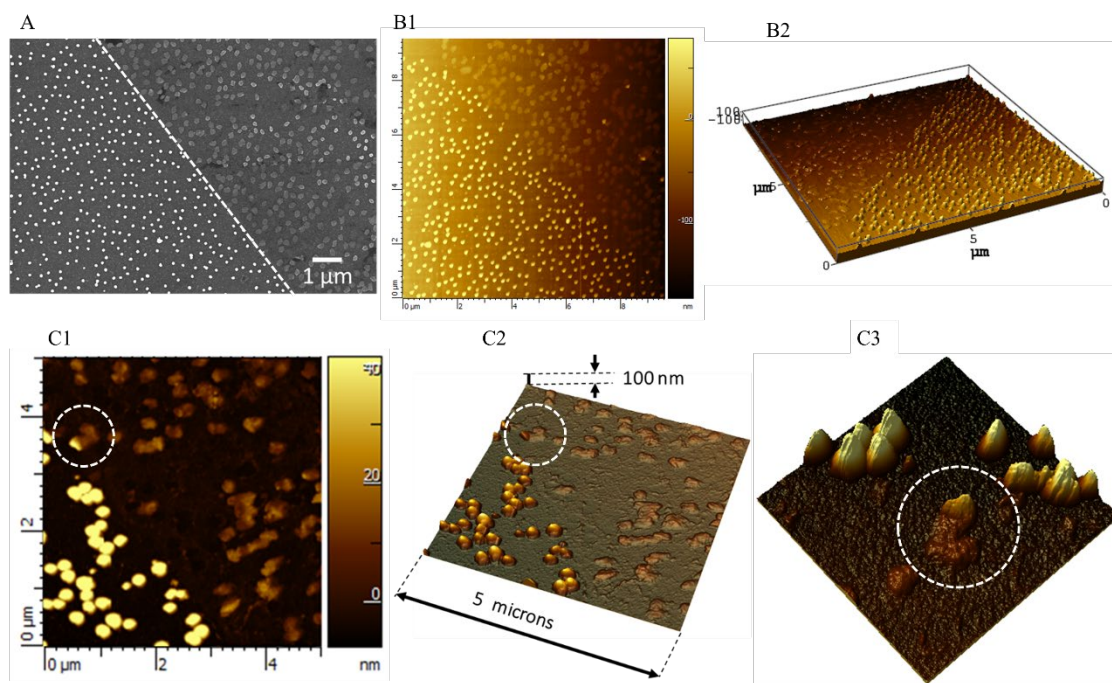


**Figure 2. 10: (A) SEM image showing both deformed (right to dotted line) and undeformed (left to dotted line) regions of Ag NPs on an ITO slide. The number of particles per unit area is unchanged before and after deformation ( $\sim 10$  particles/ $\mu\text{m}^2$ ). (B1-B2) AFM images of AgNPs deformed under a copper TEM grid pattern. Contact AFM was used to map the profiles of patterned AgNPs on PVP-functionalized ITO glass substrates by applying 50 N load. Partly deformed individual Ag nanoparticles. (C1) 2D and (C2) 3D AFM images showing boundary between deformed and undeformed AgNPs. (C3) Zoom in image showing a single nanoparticle that was partly deformed. Taken with permission of ref 1.**

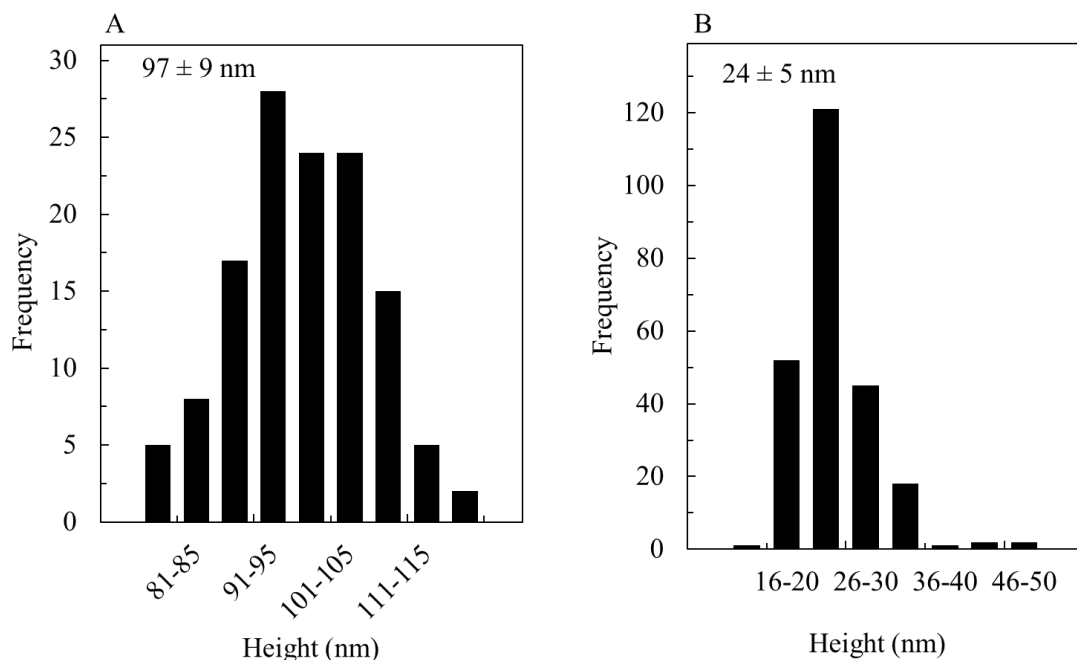


**Figure 2. 11: Histograms of the average AgNPs height (A) before and (B) after deforming using TEM grid. All AFM height measurements were obtained based on more than at least 150 particles. Taken with permission of ref 1.**

The pattern was controlled by the stamp shape. If the stamp surface was uneven, the pattern reproduced some of the stamp features on the nanoparticle deformation pattern. For example, in place of a smooth copper TEM grid, a hexagonal patterned metal grid from VACCO was used as a stamp to deform  $\sim 100$  nm silver nanoparticles. The stamp finishing produced an uneven finish with clear streaks along one axis (Figure 2.12A1), causing  $\sim 200$  nm height variation along  $20\ \mu\text{m}$  laterally, as shown in Figure 4A2. This caused similar features in the deformation (Figures 2.12B1 and B2) of Au and (Figures 2.12C1 and C2) AgNPs. This experiment demonstrates that stamps with smooth surfaces are needed to generate uniformly deformed nanoparticles and that the

surface height changes present in the stamp can be transferred to the deformed nanoparticle pattern, which can be visualized both optically and using AFM.

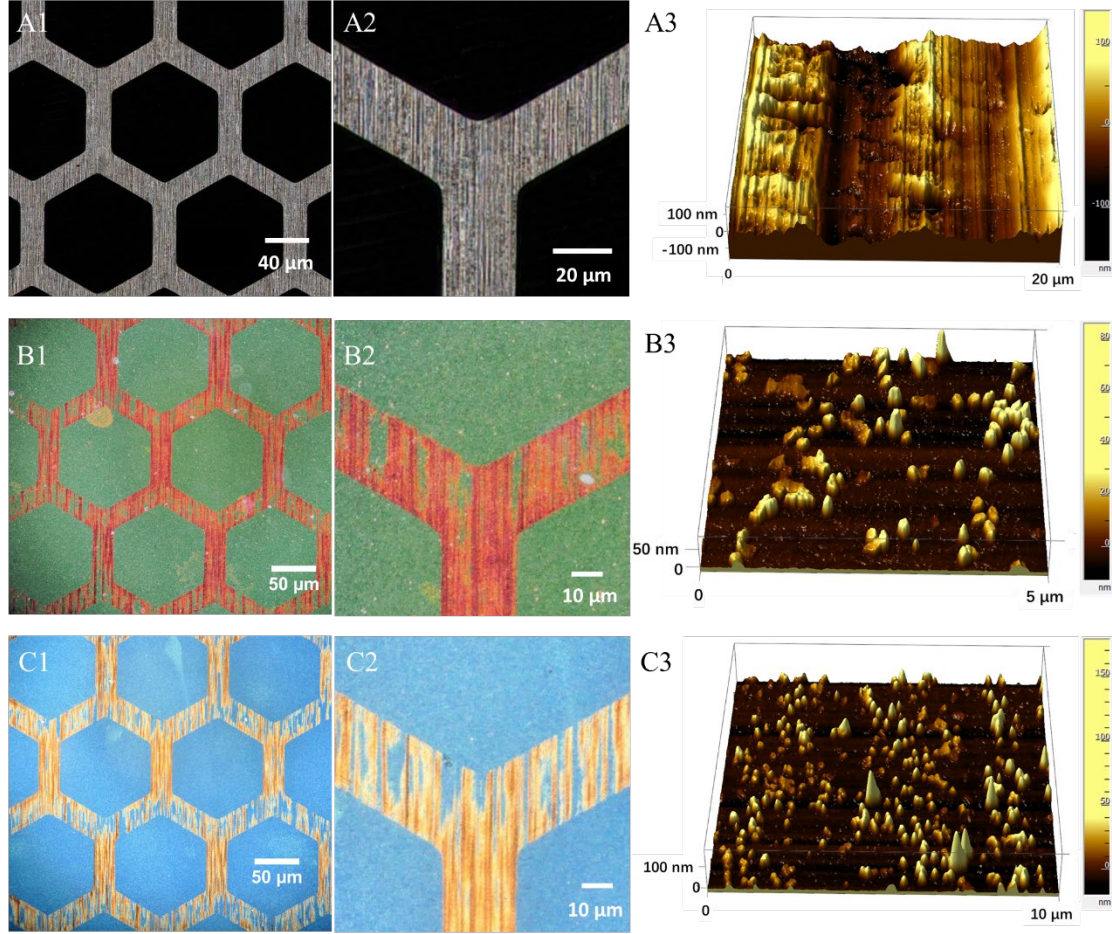


**Figure 2. 12:** (A1) Optical profiler image of VACCO grid showing parallel streaks, (A2) zoom in image of (A1). (A3) 3D AFM image showing surface roughness (ridges and grooves) of VACCO grid. Dark field microscope images of deformed regions of (B1) AuNPs and (C1) AgNPs. Zoom in images of (B2) AuNPs and (C2) AgNPs from B1 and C1 showing printed parallel streaks and surface roughness (green (B2) and blue (C2) areas in deformed regions are due to grooves of VACCO grid). 3D AFM images of (B2) AuNPs and (C2) AgNPs deformed using the hexagonal patterned VACCO grid. Taken with permission of ref 1.

Individual nanoparticles with rougher features imprinted on them may be useful in applications such as sensors and catalysis and other applications that could benefit from the relatively larger surface area when compared to that of the nanoparticle with



smoother features (Figure 2.13). A preliminary study carried out to identify potential catalysis applications is described in chapter 6.

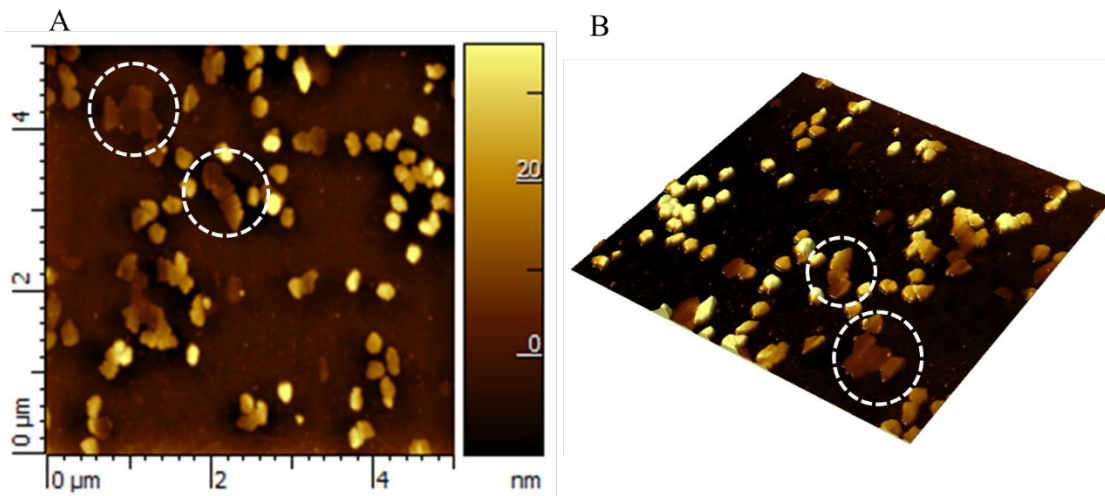


**Figure 2. 13: High resolution AFM images in (A) 2D and (B) 3D. Areas within the white circles show the deformed nanoparticles caused by the ridges in the hexagonal stamp (see Figure 4). Taken with permission of ref 1.**

AuNPs were also patterned by depositing glucose crystals to create circular points of undeformed NPs regions. Glucose crystals were deposited by dusting over AuNPs coated glass slide and then blowing off excess crystals. Then, the patterns were generated by rolling a glass rolling pin attached to the Mark-10 force gauge (Figure 2.14). Patterns were observed under dark field microscope; the glucose crystals were honored at the center of the circular undeformed NPs region, which appears blue. AuNPs away from the glucose appears red due to the complete deformation of NPs, and at the boundary of blue and red areas, there are two circles in green and yellow colors due to partial deformation of NPs. When it goes away from the glucose deposit  $\lambda_{\text{max}}$  of the dark field, single nanoparticle scattering spectra shift to the red region of the wavelength (Figure 2.14B).

Further, the SEM image showed the increase in NPs diameter when it goes away from the glucose deposit (Figure 2.14C).

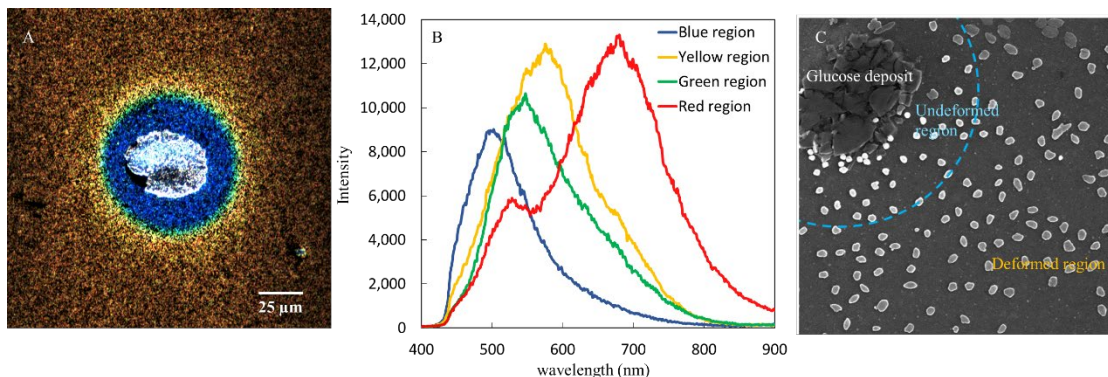


**Figure 2. 14: (A) Hyperspectral dark field image showing protected region of Ag NPs around the glucose deposit and deformed region away from the deposit. (B) Dark field single nanoparticle scattering spectra of undeformed (blue region), partially deformed (green and yellow regions) and deformed (red region) NPs corresponding to image (A). (C) Scanning electron microscopic image of patterned Ag NPs.**

For some applications, such as printing non-bleaching colorants, it would be useful to generate patterns of only deformed particles with dark nanoparticle-free regions. We found that simple adhesive tape could remove undeformed particles from the substrate. Figures 2.15(i, ii, iii) illustrate the principle of this method schematically. Figures 5A1 and B1 show hyperspectral dark field images of AuNPs and AgNPs deformed under a copper TEM-grid pattern, respectively. The deformed and undeformed areas can be clearly distinguished in these images. Figures 2.15A2, A3, and B2, B3 show the hyperspectral dark field images of patterned AuNPs and AgNPs after removing undeformed NPs using adhesive tape, respectively. This figure further confirms that this method is an effective way to remove undeformed nanoparticles from the surfaces and make patterned nanoparticle substrates. Furthermore, the approach also generated clear patterns without residues between lines (Figure 2.15B3). The preferential removal of

undeformed spherical particles was likely due to the small contact area between the spheres and surface compared to the much larger contact area after deformation.

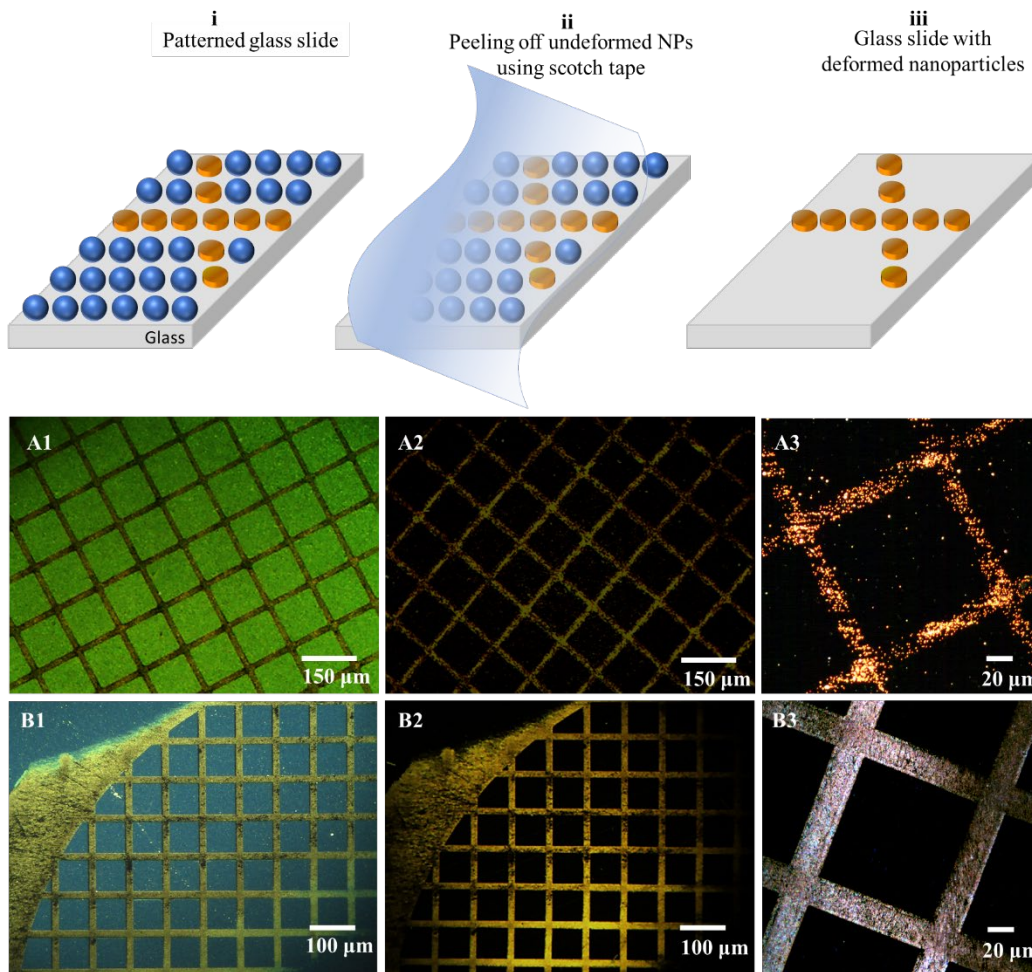


**Figure 2. 15:** i-iii, Schematic illustration of the removal of undeformed nanoparticles using adhesive tape. (i) Mechanically deformed nanoparticles; (ii) applying adhesive tape on the patterned glass substrate to peel-off undeformed NPs; (iii) pattern of deformed nanoparticles left on the glass slide. (A1-A3) Hyperspectral dark field images of AuNPs deformed with a TEM grid; (B1-B3) hyperspectral dark field images of AgNPs deformed with a TEM grid. (A1, B1) Pattern before removing undeformed particles; (A2, B2) pattern after removal of undeformed NPs with adhesive tape; (A3, B3) 40X zoom in images of patterned AuNPs and Ag NPs from A2 and B2. Taken with permission of ref 1.

Scotch tape has previously been used to capture NPs such as Ag, Au, Cu and Pd onto a flexible surface<sup>45</sup> for numerous applications, including point of care detection of



bacterial infections and to detect pesticides on fruits and vegetables using Surface Enhanced Raman Spectroscopy (SERS).<sup>45,46</sup> Although the scotch can provide a background signal in these sensing applications; the analyte can be distinguished and detected. There was no noticeable residue from the tape in the dark field images or electron microscopy and AFM images; however, it is possible that a thin residue could be left behind, which could provide a background signal in sensing applications that would require either chemical removal (e.g., alcohol washing) or plasma treatment.

Patterned nanoparticle arrays could also be transferred to a flexible polymer surface. We used First Contact Polymer (Platteville, WI) which is generally used to remove dust, fingerprints, residues and contaminants from precision surfaces such as lenses. Clear First Contact Polymer is a colorless solution that dries into a flexible thin-film at room temperature, and can be peeled off easily. Moreover, it can be either stretched or bent, and after the force is removed its original shape and size are restored (Figure 2.16A1-A3).

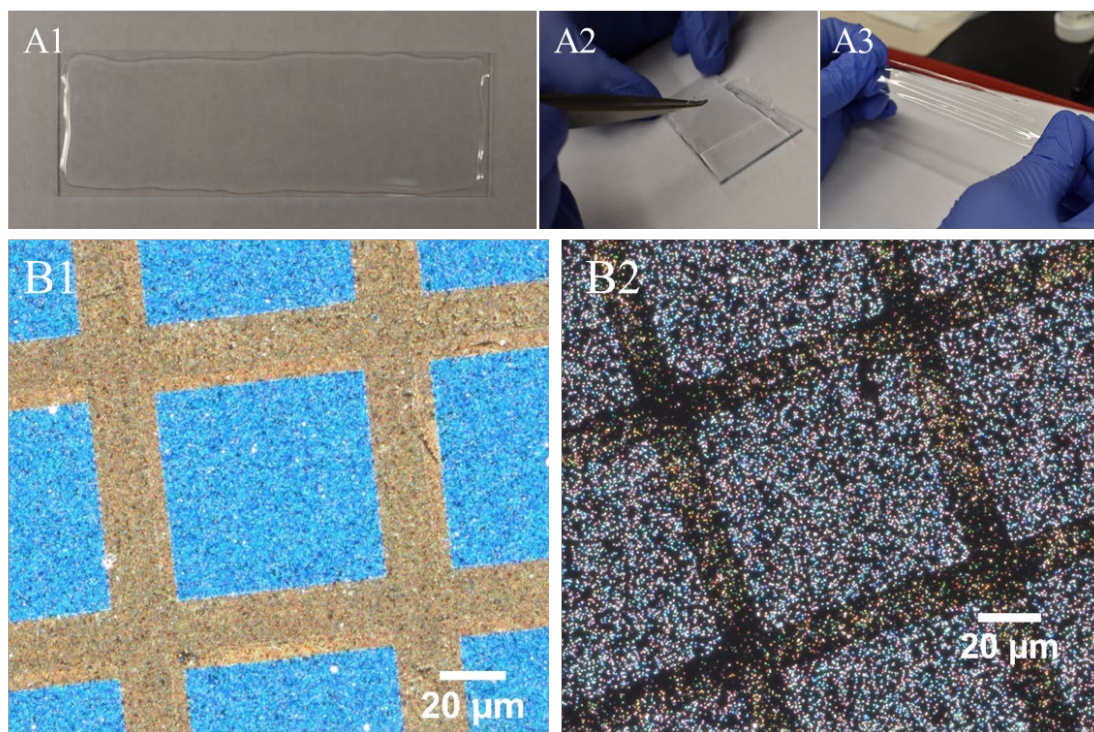


**Figure 2. 16: Transferring AgNPs to flexible polymer films. (A1) First Contact™ clear polymer polymerized into a thin-film on a glass slide. (A2) Peeling off, and (A3) stretching of the clear thin-film. Dark field microscope images (100 x oil, immersion) of (B1) patterned and undeformed Ag NPs on a glass slide, (B2) patterned and undeformed Ag NPs remaining on glass slide after removing NPs using a thin film. Taken with permission of ref 1.**

By applying liquid polymer onto the patterned region and allowing it to dry, the NPs can be transferred onto the polymer surface. When the polymer solution is dried fast (within 5 minutes) on a NPs coated glass slide, the undeformed NPs are transferred onto the thin film, leaving deformed NPs on the glass slide (Figure 2.17B i-iii). When the polymer solution is dried slowly (dried within 30 minutes), both undeformed and deformed NPs are transferred onto the thin film (Figure 2.17C i-iii). The slower evaporation results in uniform, resilient and good quality thin film that is in contact with the top and sides of the NPs, including any overhang. Before transferring NPs onto thin

film, about 10 particles per  $\mu\text{m}^2$  were present (forming continuous colored regions in the diffraction-limited dark field images but countable in SEM images); after transferring the NPs the remaining particles on the glass slide could be clearly distinguished and counted in dark field imaging and had a concentration of  $\sim 0.6$  particles per  $\mu\text{m}^2$  (Figure 2.16B1-2). After removing undeformed NPs using a scotch tape, the deformed nanoparticles in the patterned region can also be transferred onto a polymer surface (Figure 2.17D i-iii). Both clear and red First Contact Polymer can be used to remove nanoparticles.

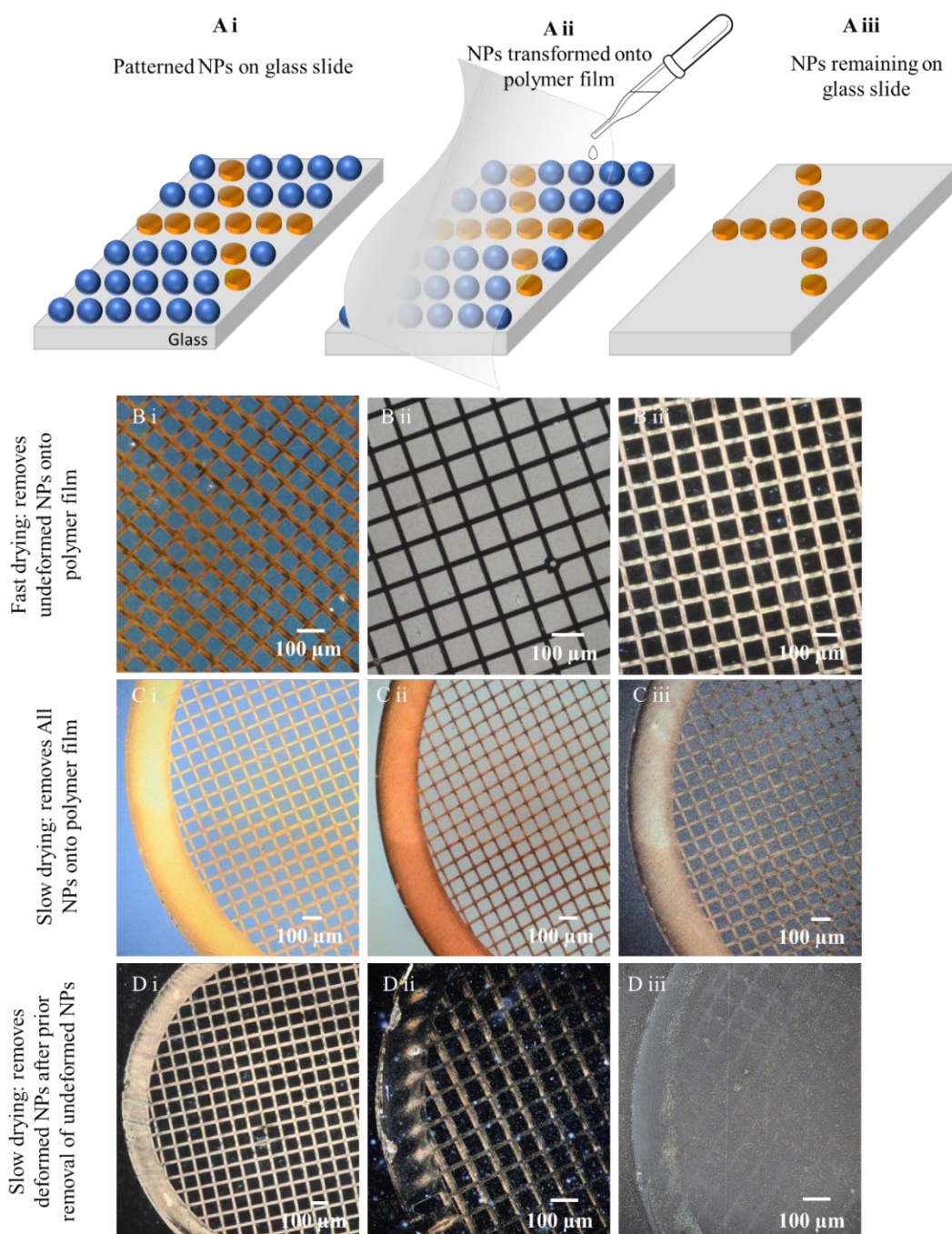


**Figure 2. 17:** A i-A iii, Schematic illustration of the transfer of NPs onto a clear polymer-film. (A i) Patterned and undeformed NPs on glass slide; (A ii) applying Clear First Contact polymer, letting it dry and peeling off (NPs transferred onto the polymer-film); (A iii) NPs remained on the glass slide. Dark field microscope images of patterned and undeformed NPs on (B i) glass slide and (B ii) undeformed NPs on polymer-film, (B iii) remaining NPs on the glass slide. Dark field microscope images of patterned and undeformed NPs on (C i) glass slide and (C ii) on polymer-film, (C iii) remaining NPs on the glass slide. Dark field microscope images of patterned NPs on (D i) glass slide after removing undeformed NPs and (D ii) patterned NPs on polymer-film, (D iii) remaining NPs on the glass slide. Taken with permission of ref 1.

## **2.5. Conclusions**

We demonstrated a simple method to pattern gold and silver nanoparticles and controlled their shapes by pressing a stamp onto the coating of the particles on a glass substrate. The resulting nanoparticle shape change induces a red-shift in the localized surface plasmon resonance, while regions untouched by the stamp remain unchanged. Using this method, we demonstrated that a single nanoparticle can be partially patterned or deformed. Furthermore, (i) regions with only deformed nanoparticles present on the glass substrate can be prepared by removing undeformed nanoparticles with a tape, and (ii) patterns of both deformed and undeformed nanoparticles can be transferred onto a thin polymer film. This is a simple, inexpensive, and yet effective technique to control the size and shape via patterning to tune the optical properties of nanoparticles. Future work will involve studying how changes in the nanoparticle surface roughness influence the catalytic and sensing properties of AuNPs and AgNPs.

## **2.6. Acknowledgment**

The material is based upon work supported by NIBIB of the National Institutes of Health under award number 1R21EB019709-01A1 and NIGMS of the National Institutes of Health under award number 5P20GM103444-07 outreach activities based on the results were supported by NSF CHE1255535. We thank the Clemson Light Imaging Facility (CLIF) for using their hyperspectral imaging microscope and the electron microscopy facility (EM Lab) for the use of their electron microscopes.

## 2.7. References

- (1) Ameer, F. S.; Ranasinghe, M.; Varahagiri, S.; Benza, D. W.; Hu, L.; Willett, D. R.; Wen, Y.; Bhattacharya, S.; Chumanov, G.; Rao, A. M.; Anker, J. N. Impressively Printing Patterns of Gold and Silver Nanoparticles. *Nano Select* **2021**, 2 (12), 2407–2418. <https://doi.org/10.1002/nano.202000278>.
- (2) Yguerabide, J.; Yguerabide, E. E. Light-Scattering Submicroscopic Particles as Highly Fluorescent Analogs and Their Use as Tracer Labels in Clinical and Biological Applications: II. Experimental Characterization. *Analytical Biochemistry* **1998**, 262 (2), 157–176. <https://doi.org/10.1006/abio.1998.2760>., Schultz, S.; Smith, D. R.; Mock, J. J.; Schultz, D. A. Single-Target Molecule Detection with Nonbleaching Multicolor Optical Immunolabels. *PNAS* **2000**, 97 (3), 996–1001. <https://doi.org/10.1073/pnas.97.3.996>.
- (3) Nanoparticle-Based Bio-Bar Codes for the Ultrasensitive Detection of Proteins <https://www.science.org/doi/10.1126/science.1088755> (accessed 2021 -12 -15).
- (4) Jaque, D.; Maestro, L. M.; Rosal, B. del; Haro-Gonzalez, P.; Benayas, A.; L. Plaza, J.; Rodríguez, E. M.; Solé, J. G. Nanoparticles for Photothermal Therapies. *Nanoscale* **2014**, 6 (16), 9494–9530. <https://doi.org/10.1039/C4NR00708E>.
- (5) Oligonucleotide-Modified Gold Nanoparticles for Intracellular Gene Regulation <https://www.science.org/doi/10.1126/science.1125559> (accessed 2021 -12 -15).
- (6) Srituravanich, W.; Fang, N.; Sun, C.; Luo, Q.; Zhang, X. Plasmonic Nanolithography. *Nano Lett.* **2004**, 4 (6), 1085–1088. <https://doi.org/10.1021/nl049573q>.

- (7) Kik, P. G.; Maier, S. A.; Atwater, H. A. Image Resolution of Surface-Plasmon-Mediated near-Field Focusing with Planar Metal Films in Three Dimensions Using Finite-Linewidth Dipole Sources. *Phys. Rev. B* **2004**, *69* (4), 045418.  
<https://doi.org/10.1103/PhysRevB.69.045418>.
- (8) Sundaramurthy, A.; Schuck, P. J.; Conley, N. R.; Fromm, D. P.; Kino, G. S.; Moerner, W. E. Toward Nanometer-Scale Optical Photolithography: Utilizing the Near-Field of Bowtie Optical Nanoantennas. *Nano Lett.* **2006**, *6* (3), 355–360.  
<https://doi.org/10.1021/nl052322c>.
- (9) Tan, S. J.; Zhang, L.; Zhu, D.; Goh, X. M.; Wang, Y. M.; Kumar, K.; Qiu, C.-W.; Yang, J. K. W. Plasmonic Color Palettes for Photorealistic Printing with Aluminum Nanostructures. *Nano Lett.* **2014**, *14* (7), 4023–4029.  
<https://doi.org/10.1021/nl501460x>.
- (10) Cheng, F.; Gao, J.; Luk, T. S.; Yang, X. Structural Color Printing Based on Plasmonic Metasurfaces of Perfect Light Absorption. *Sci Rep* **2015**, *5* (1), 11045.  
<https://doi.org/10.1038/srep11045>.
- (11) Capobianco, N.; Hunault, M. O. J. Y.; Balcon-Berry, S.; Galois, L.; Sandron, D.; Calas, G. The Grande Rose of the Reims Cathedral: An Eight-Century Perspective on the Colour Management of Medieval Stained Glass. *Sci Rep* **2019**, *9* (1), 3287.  
<https://doi.org/10.1038/s41598-019-39740-y>.
- (12) Guay, J.-M.; Calà Lesina, A.; Côté, G.; Charron, M.; Poitras, D.; Ramunno, L.; Berini, P.; Weck, A. Laser-Induced Plasmonic Colours on Metals. *Nat Commun* **2017**, *8* (1), 16095. <https://doi.org/10.1038/ncomms16095>.



- (13) Duan, X.; Kamin, S.; Liu, N. Dynamic Plasmonic Colour Display. *Nat Commun* **2017**, *8* (1), 14606. <https://doi.org/10.1038/ncomms14606>.
- (14) Arppe-Tabbara, R.; Tabbara, M.; Sørensen, T. J. Versatile and Validated Optical Authentication System Based on Physical Unclonable Functions. *ACS Appl. Mater. Interfaces* **2019**, *11* (6), 6475–6482. <https://doi.org/10.1021/acsami.8b17403>.
- (15) Mulvaney, P.; Pérez-Juste, J.; Giersig, M.; Liz-Marzán, L. M.; Pecharromán, C. Drastic Surface Plasmon Mode Shifts in Gold Nanorods Due to Electron Charging. *Plasmonics* **2006**, *1* (1), 61–66. <https://doi.org/10.1007/s11468-005-9005-0>.
- (16) Boltasseva, A.; Shalaev, V. M. All That Glitters Need Not Be Gold. *Science* **2015**, *347* (6228), 1308–1310. <https://doi.org/10.1126/science.aaa8282>.
- (17) Ansar, S. M.; Kitchens, C. L. Impact of Gold Nanoparticle Stabilizing Ligands on the Colloidal Catalytic Reduction of 4-Nitrophenol. *ACS Catal.* **2016**, *6* (8), 5553–5560. <https://doi.org/10.1021/acscatal.6b00635>.
- (18) Yang, F.; Deng, D.; Pan, X.; Fu, Q.; Bao, X. Understanding Nano Effects in Catalysis. *National Science Review* **2015**, *2* (2), 183–201. <https://doi.org/10.1093/nsr/nwv024>.
- (19) Jeanmaire, D. L.; Van Duyne, R. P. Surface Raman Spectroelectrochemistry: Part I. Heterocyclic, Aromatic, and Aliphatic Amines Adsorbed on the Anodized Silver Electrode. *Journal of Electroanalytical Chemistry and Interfacial Electrochemistry* **1977**, *84* (1), 1–20. [https://doi.org/10.1016/S0022-0728\(77\)80224-6](https://doi.org/10.1016/S0022-0728(77)80224-6).



- (20) Nie, S.; Emory, S. R. Probing Single Molecules and Single Nanoparticles by Surface-Enhanced Raman Scattering. *Science* **1997**, 275 (5303), 1102–1106.  
<https://doi.org/10.1126/science.275.5303.1102>.
- (21) Willets, K. A.; Van Duyne, R. P. Localized Surface Plasmon Resonance Spectroscopy and Sensing. *Annual Review of Physical Chemistry* **2007**, 58 (1), 267–297. <https://doi.org/10.1146/annurev.physchem.58.032806.104607>.
- (22) Anker, J. N.; Hall, W. P.; Lyandres, O.; Shah, N. C.; Zhao, J.; Van Duyne, R. P. Biosensing with Plasmonic Nanosensors. In *Nanoscience and Technology*; Co-Published with Macmillan Publishers Ltd, UK, 2009; pp 308–319.  
[https://doi.org/10.1142/9789814287005\\_0032](https://doi.org/10.1142/9789814287005_0032).
- (23) Zhang, J.; Fu, Y.; Chowdhury, M. H.; Lakowicz, J. R. Metal-Enhanced Single-Molecule Fluorescence on Silver Particle Monomer and Dimer: Coupling Effect between Metal Particles. *Nano Lett.* **2007**, 7 (7), 2101–2107.  
<https://doi.org/10.1021/nl071084d>.
- (24) Zhang, Y.; Zhen, Y.-R.; Neumann, O.; Day, J. K.; Nordlander, P.; Halas, N. J. Coherent Anti-Stokes Raman Scattering with Single-Molecule Sensitivity Using a Plasmonic Fano Resonance. *Nat Commun* **2014**, 5 (1), 4424.  
<https://doi.org/10.1038/ncomms5424>.
- (25) Lian, J.; Wang, L.; Sun, X.; Yu, Q.; Ewing, R. C. Patterning Metallic Nanostructures by Ion-Beam-Induced Dewetting and Rayleigh Instability. *Nano Lett.* **2006**, 6 (5), 1047–1052. <https://doi.org/10.1021/nl060492z>.

- (26) Sreenivasan, S. V. Nanoimprint Lithography Steppers for Volume Fabrication of Leading-Edge Semiconductor Integrated Circuits. *Microsyst Nanoeng* **2017**, *3* (1), 1–19. <https://doi.org/10.1038/micronano.2017.75>.
- (27) Braun, G. B.; Friman, T.; Pang, H.-B.; Pallaoro, A.; de Mendoza, T. H.; Willmore, A.-M. A.; Kotamraju, V. R.; Mann, A. P.; She, Z.-G.; Sugahara, K. N.; Reich, N. O.; Teesalu, T.; Ruoslahti, E. Etchable Plasmonic Nanoparticle Probes to Image and Quantify Cellular Internalization. *Nature Mater* **2014**, *13* (9), 904–911. <https://doi.org/10.1038/nmat3982>.
- (28) Lim, H.; Choi, K.-B.; Kim, G.; Park, S.; Ryu, J.; Lee, J. Roller Nanoimprint Lithography for Flexible Electronic Devices of a Sub-Micron Scale. *Microelectronic Engineering* **2011**, *88* (8), 2017–2020. <https://doi.org/10.1016/j.mee.2011.02.018>.
- (29) Patel, A.; Svirko, Y.; Durfee, C.; Kazansky, P. G. Direct Writing with Tilted-Front Femtosecond Pulses. *Sci Rep* **2017**, *7* (1), 12928. <https://doi.org/10.1038/s41598-017-13403-2>.
- (30) Zhang, X.; Yonzon, C. R.; Van Duyne, R. P. Nanosphere Lithography Fabricated Plasmonic Materials and Their Applications. *Journal of Materials Research* **2006**, *21* (5), 1083–1092. <https://doi.org/10.1557/jmr.2006.0136>.
- (31) Ameer, F. S.; Varahagiri, S.; Benza, D. W.; Willett, D. R.; Wen, Y.; Wang, F.; Chumanov, G.; Anker, J. N. Tuning Localized Surface Plasmon Resonance Wavelengths of Silver Nanoparticles by Mechanical Deformation. *J. Phys. Chem. C* **2016**, *120* (37), 20886–20895. <https://doi.org/10.1021/acs.jpcc.6b02169>.

- (32) Malynych, S.; Luzinov, I.; Chumanov, G. Poly(Vinyl Pyridine) as a Universal Surface Modifier for Immobilization of Nanoparticles. *J. Phys. Chem. B* **2002**, *106* (6), 1280–1285. <https://doi.org/10.1021/jp013236d>.
- (33) Evanoff, D. D.; Chumanov, G. Size-Controlled Synthesis of Nanoparticles. 2. Measurement of Extinction, Scattering, and Absorption Cross Sections. *J. Phys. Chem. B* **2004**, *108* (37), 13957–13962. <https://doi.org/10.1021/jp0475640>.
- (34) Ziegler, C.; Eychmüller, A. Seeded Growth Synthesis of Uniform Gold Nanoparticles with Diameters of 15–300 Nm. *J. Phys. Chem. C* **2011**, *115* (11), 4502–4506. <https://doi.org/10.1021/jp1106982>.
- (35) Mohsin, M.; Jawad, M.; Yameen, M. A.; Waseem, A.; Shah, S. H.; Shaikh, A. J. An Insight into the Coating Behavior of Bimetallic Silver and Gold Core-Shell Nanoparticles. *Plasmonics* **2020**, *15* (6), 1599–1612. <https://doi.org/10.1007/s11468-020-01166-y>.
- (36) Ogata, S.; Li, J.; Hirosaki, N.; Shibutani, Y.; Yip, S. Ideal Shear Strain of Metals and Ceramics. *Phys. Rev. B* **2004**, *70* (10), 104104. <https://doi.org/10.1103/PhysRevB.70.104104>.
- (37) Li, Q.; Chen, F.; Kang, J.; Su, J.; Huang, F.; Wang, P.; Yang, X.; Hou, Y. Physical Unclonable Anticounterfeiting Electrodes Enabled by Spontaneously Formed Plasmonic Core–Shell Nanoparticles for Traceable Electronics. *Advanced Functional Materials* *n/a* (n/a), 2010537. <https://doi.org/10.1002/adfm.202010537>.
- (38) Chen, F.; Li, Q.; Li, M.; Huang, F.; Zhang, H.; Kang, J.; Wang, P. Unclonable Fluorescence Behaviors of Perovskite Quantum Dots/Chaotic Metasurfaces Hybrid

Nanostructures for Versatile Security Primitive. *Chemical Engineering Journal* **2021**, *411*, 128350. <https://doi.org/10.1016/j.cej.2020.128350>.

- (39) Kalytchuk, S.; Wang, Y.; Poláková, K.; Zbořil, R. Carbon Dot Fluorescence-Lifetime-Encoded Anti-Counterfeiting. *ACS Appl. Mater. Interfaces* **2018**, *10* (35), 29902–29908. <https://doi.org/10.1021/acsami.8b11663>.
- (40) Kelly, K. L.; Coronado, E.; Zhao, L. L.; Schatz, G. C. The Optical Properties of Metal Nanoparticles: The Influence of Size, Shape, and Dielectric Environment. *J. Phys. Chem. B* **2003**, *107* (3), 668–677. <https://doi.org/10.1021/jp026731y>.
- (41) Myroshnychenko, V.; Rodríguez-Fernández, J.; Pastoriza-Santos, I.; M. Funston, A.; Novo, C.; Mulvaney, P.; M. Liz-Marzán, L.; Abajo, F. J. G. de. Modelling the Optical Response of Gold Nanoparticles. *Chemical Society Reviews* **2008**, *37* (9), 1792–1805. <https://doi.org/10.1039/B711486A>.
- (42) Wokaun, A.; Gordon, J. P.; Liao, P. F. Radiation Damping in Surface-Enhanced Raman Scattering. *Phys. Rev. Lett.* **1982**, *48* (14), 957–960. <https://doi.org/10.1103/PhysRevLett.48.957>.
- (43) Meier, M.; Wokaun, A. Enhanced Fields on Large Metal Particles: Dynamic Depolarization. *Opt. Lett., OL* **1983**, *8* (11), 581–583. <https://doi.org/10.1364/OL.8.000581>.
- (44) Noguez, C. Optical Properties of Isolated and Supported Metal Nanoparticles. *Optical Materials* **2005**, *27* (7), 1204–1211. <https://doi.org/10.1016/j.optmat.2004.11.012>.

- (45) Baytekin, H. T.; Baytekin, B.; Huda, S.; Yavuz, Z.; Grzybowski, B. A.  
Mechanochemical Activation and Patterning of an Adhesive Surface toward  
Nanoparticle Deposition. *J. Am. Chem. Soc.* **2015**, *137* (5), 1726–1729.  
<https://doi.org/10.1021/ja507983x>.
- (46) Chen, J.; Huang, Y.; Kannan, P.; Zhang, L.; Lin, Z.; Zhang, J.; Chen, T.; Guo, L.  
Flexible and Adhesive Surface Enhance Raman Scattering Active Tape for Rapid  
Detection of Pesticide Residues in Fruits and Vegetables. *Anal. Chem.* **2016**, *88* (4),  
2149–2155. <https://doi.org/10.1021/acs.analchem.5b03735>.

## CHAPTER THREE

### X-RAY EXCITED LUMINESCENCE SPECTROSCOPY AND IMAGING WITH NaGdF<sub>4</sub>:Eu AND Tb

*Much of the material in this chapter was published as a journal article: Ranasinghe, M.; Arifuzzaman, M.; Rajamanthrilage, A. C.; Dickey, A.; Kolis, J. W.; Bolding, M.; Anker, J. X-Ray Excited Luminescence Spectroscopy and Imaging with NaGdF<sub>4</sub>:Eu and Tb. 2020. RSC Adv., 2021, 11, 31717-31726. <https://doi.org/10.1039/D1RA05451A>.*

#### 3.1. Abstract

Like plasmonic nanoparticles, X-ray luminescence nanoparticles also have interesting optical properties (in this case X-ray excited optical luminescence) and can be functionalized with biomolecules to use in bioimaging and sensing applications. The intensity of optical X-ray excited optical luminescence is dependent on the nanoparticle size, host matrix, crystallinity, activator and impurity concentrations, etc. X-ray excited optical luminescence from nanophosphors can be used to selectively generate light in tissue for imaging and stimulating light-responsive materials and cells. Herein, we synthesized X-ray scintillating NaGdF<sub>4</sub>:Eu and Tb nanophosphors via co-precipitate and hydrothermal methods, encapsulated with silica, functionalized with biotin, and characterized by X-ray excited optical luminescence spectroscopy and imaging. The nanophosphors synthesized by the co-precipitate method were ~90 and ~106 nm in diameter, respectively, with hydrothermally synthesized particles showing the highest luminescence intensity. More importantly, we investigated the effect of thermal annealing/calcination on the X-ray excited luminescence spectra and intensity. At above 1000 °C, the luminescence intensity increased, but particles fused together. Coating with a 15 nm thick silica shell prevented particle fusion and enabled silane-based chemical

functionalization, although luminescence decreased largely due to the increased mass of non-luminescent material. We observed an increase in luminescence intensity with temperature until 400 °C. At above 600 °C, NaGdF<sub>4</sub>:Eu@SiO<sub>2</sub> converts to NaGd<sub>9</sub>Si<sub>6</sub>O<sub>26</sub>:Eu, an X-ray scintillator brighter than annealed NPs at 400 °C and dimmer than NPs synthesized using the hydrothermal method. The particles generate light through tissue and can be selectively excited using a focused X-ray source for imaging and light generation applications. The particles also act as MRI contrast agents for multi-modal localization.

### **3.2. Introduction**

Light can be a powerful tool for studying biochemistry in cells and tissue and for stimulating responses from genetically engineered light-sensitive neurons (optogenetics) or photo-released drugs. The challenge for delivering or retrieving light from deep tissue is that scattering in the tissue prevents light from traveling ballistically, and the point spread function is typically >1 cm through 1 cm of tissue; also, the light is attenuated by the tissue.<sup>1,2</sup> One approach that circumvents these problems is to use selectively generate light using focused X-ray beams to generate visible luminescence from scintillators implanted or injected in the tissue. Since X-rays are far less scattered than visible and near-infrared light, the X-ray beam focus can be maintained through the tissue and generate visible light locally after absorption by scintillator particles. Scintillators are luminescent materials that absorb high-energy radiation ( $\gamma$ - and X-ray photons, high energy ions, neutrons, or other subatomic particles) and emit UV, visible and/or NIR

light.<sup>1,2</sup> These materials are widely used in radiation detection<sup>3</sup> and imaging applications,<sup>4-6</sup> and occasionally in external power-free light generation applications (e.g., old luminescent watches, emergency lighting, and gun sites).<sup>7</sup> Recently, researchers have been developing scintillator nanophosphors for improved X-ray luminescence imaging,<sup>8-10</sup> radiation imaging,<sup>9,11,12</sup> and as a potential light source for photochemistry and photobiology (e.g., X-ray excited optogenetics<sup>13</sup>).

Rare-earth doped materials (NaGdF<sub>4</sub>:Eu<sup>14,15</sup> and Tb,<sup>16</sup> Gd<sub>2</sub>O<sub>2</sub>S:Eu and Tb,<sup>10</sup> YAG:Nd, LuAG:Tm, Lu<sub>2</sub>SiO<sub>5</sub>:Ce<sup>17</sup>) have interesting properties, including narrow and distinct spectral emission peaks, large optical penetration depth, negligible autofluorescence background, photochemical stability, and low toxicity.<sup>6</sup> Among them, rare-earth fluorides (NaGdF<sub>4</sub>) are considered excellent host matrices for luminescent rare earth elements (e.g., Eu and Tb). They usually have high refractive indices and low phonon energies, which cause a low probability of nonradiative decay and higher luminescent quantum yields compared to oxide hosts and other inorganic matrices.<sup>18</sup>

Herein, we synthesize 100 nm diameter NaGdF<sub>4</sub>:Eu and NaGdF<sub>4</sub>:Tb nanophosphors for X-ray excited luminescence. This diameter is in a good range for long circulation as nanoparticles smaller than ~5.5 nm undergo relatively fast blood clearance by renal filtration, nanoparticles smaller than ~70 nm filter through fenestrae of hepatic sinusoids,<sup>19-21</sup> while nanoparticles between 200–500 nm are endocytosed by phagocytic or non-phagocytic cells and nanoparticles larger than 500 nm are likely to remove from cells by phagocytosis.<sup>19-22</sup> Thus, nanoparticles with 100 nm diameter have shown the minimum effect on blood clearance mechanisms (e.g., renal, liver filtration) and



prolonged circulation time.<sup>20,21</sup> These intermediate-size nanoparticles tend to accumulate in perivascular spaces of permeable tissues (e.g., liver and spleen, tumor, site of inflammation and angiogenesis)<sup>19,20</sup> allowing bicomponent imaging.

We also compared X-ray excited optical luminescence (XEOL) spectra from hydrothermal and co-precipitation synthesis methods and the effect of thermal annealing. Nanoparticle annealing at high temperature is a widespread method in upconversion nanophosphors to enhance luminescence<sup>10,23,24</sup> by reducing crystal defect, increasing crystal domain size, and removing trapped water and carbon dioxide. However, enhancing luminescence of X-ray excited nanophosphors using annealing techniques is still under investigation. Here, we synthesized both NaGdF<sub>4</sub>:Tb and NaGdF<sub>4</sub>:Eu, which have distinct spectra. The nanophosphors were functionalized with biotin and attached to streptavidin in vitro. They could be selectively excited in a solution using a focused X-ray source to obtain XEOL spectroscopy and image through tissue; here, we focused on the NaGdF<sub>4</sub>:Eu because their red emission has deeper penetration through tissue than the largely green-emitting NaGdF<sub>4</sub>:Tb.<sup>25,26</sup> Additionally, the particles serve as T<sub>1</sub> and T<sub>2</sub> MRI contrast agents, useful for multi-modal imaging applications.

### **3.3. Methods**

#### *3.3.1. NaGdF<sub>4</sub>:Eu and NaGdF<sub>4</sub>:Tb nanoparticle synthesis*

We synthesized particles using either the co-precipitation or hydrothermal synthesis methods.

**Co-precipitate synthesis method.** NaGdF<sub>4</sub>:Eu and Tb nanophosphors were synthesized by the citrate method with slight modifications.<sup>14,27</sup> Sodium citrate (12 mL of 0.2 M) was added to a clear aqueous solution containing 4 mL of Gd(NO<sub>3</sub>)<sub>3</sub> (0.2 M) and Tb(NO<sub>3</sub>)<sub>3</sub>/Eu(NO<sub>3</sub>)<sub>3</sub> (X mol%) and stirred vigorously for 30 min at room temperature. Then, 16 mL of sodium fluoride (1 M) solution was combined with the above mixture and stirred vigorously for another 2 hours which result in a white solution. The synthesized nanophosphors were centrifuged and washed three times before further experiments. (Tb(NO<sub>3</sub>)<sub>3</sub>/Eu(NO<sub>3</sub>)<sub>3</sub> X mol% = 0.1%, 1%, 15% 20%, 100% of Gd<sup>3+</sup> moles).

**Hydrothermal synthesis method.** NaGdF<sub>4</sub>:Eu and Tb nanophosphors were synthesized by the citrate method with slight modifications.<sup>14,15,27</sup> Sodium citrate (12 mL of 0.2 M) was added to a clear aqueous solution containing 4 mL of GdNO<sub>3</sub> (0.2 M) and Tb(NO<sub>3</sub>)<sub>3</sub>/Eu(NO<sub>3</sub>)<sub>3</sub> (X mol%) and stirred for 30 min. Then, 16 mL of sodium fluoride (1 M) solution was combined with the above mixture and stirred vigorously for another 15 minutes which result in a white solution. This solution was transferred to a Teflon-lined autoclave and heated at 180 °C for 6 hours. The synthesized nanophosphors were centrifuged and washed three times before further experiments. The synthesized nanophosphors were stored in either DI water or 0.1% citrate solution. (Tb(NO<sub>3</sub>)<sub>3</sub>/Eu(NO<sub>3</sub>)<sub>3</sub> X mol% = 0.1%, 1%, 15% 20%, 100% of Gd<sup>3+</sup> moles).

### 3.3.2. *Silica coating NaGdF<sub>4</sub>:Eu and Tb nanoparticles*

Synthesized nanophosphors were coated with silica using previously described methods<sup>28–30</sup> with slight modifications (certain reagents were scaled up). Eu doped and Tb doped NaGdF<sub>4</sub> nanoparticles prepared at room temperature were resuspended in 8 mL of water and combined with 200 mL ethanol solution containing PVP (1.2 g) and ammonium hydroxide (6 mL). Then, TEOS (160  $\mu$ L) was added after the solution was stirred for 20 min. The particles were aged another 3 hours before centrifuged and washed using DI water.

### 3.3.3. *Annealing NaGdF<sub>4</sub>:Eu nanoparticles*

NaGdF<sub>4</sub>:Eu nanoparticles prepared using the co-precipitate method were dried at 80 °C to form a white powder. It was transferred to a crucible and heated (10 °C min<sup>-1</sup>) at 1000 °C for 6 hours in a muffle furnace which results in a solid, aggregated structure. After cooling down to room temperature, it was crushed into a fine powder using mortar and pestle.

NaGdF<sub>4</sub>:Eu@SiO<sub>2</sub> nanophosphors were dried at 80 °C to form a white powder and divide into three portions and transferred to crucibles. The samples were heated at 400 °C, 600 °C and 1000 °C for 6 hours to anneal them.

### 3.3.4. *Functionalization of NaGdF<sub>4</sub>:Eu@SiO<sub>2</sub> with biotin*

NaGdF<sub>4</sub>:Eu@SiO<sub>2</sub> nanophosphors were resuspended in ethanol (100 mL) with APTES (300  $\mu$ L) and stirred for 3.5 h. The amine-functionalized nanophosphors were collected and washed three times using DI water.

98 mL of MES buffer (0.1 M, pH 6.0) was taken in a 500 mL round bottom flask. ~100 mg of water-soluble carbodiimide (EDC) and sulfo-NHS was added to it and stirred for 15 minutes at room temperature.  $\text{H}_2\text{PO}_4\text{-PEG-COOH}$  (5000 Da) (500  $\mu\text{L}$ , 10  $\text{mg mL}^{-1}$ ) and biotin-PEG-COOH (1000 Da) (250  $\mu\text{L}$ , 10  $\text{mg mL}^{-1}$ ) was added to the above solution and stirred for 1 hour at room temperature to activate COOH groups. Then, the solution pH was adjusted to pH 7.4 using PBS buffer. Previously prepared  $\text{NH}_2$  functionalized  $\text{NaGdF}_4\text{:Eu@SiO}_2$  nanoparticles were added to the mixture and it could react for 12 h at room temperature with continuous stirring. Lastly, biotin-conjugated NPs were washed with PBS three times and stored in DI water.

Biotin functionalized aqueous nanophosphors suspension (10  $\text{mg mL}^{-1}$ , 20  $\mu\text{L}$ ) was transferred into a centrifuge tube contained PBS (10 $\times$ , 380  $\mu\text{L}$ ) solution. Streptavidin-coated microbubbles (100  $\mu\text{L}$ ) were mixed with the previous solution and vortexed to allow particle adhesion on the surface of the microbubble. After waiting a 10–15 minutes, suspended microbubbles were pipetted out and washed three times with DI water.<sup>31,32</sup>

### 3.3.5. *Dark field optical imaging capillaries filled with $\text{NaGdF}_4\text{:Eu}$ through tissue*

A series of concentration of  $\text{NaGdF}_4\text{:Eu}$  (100, 50 and 0  $\text{mg mL}^{-1}$ ) was prepared and filled in 1 mm (inner diameter) capillaries.

X-ray excited optical luminescence of all the samples in capillaries were measured by irradiating with a Mini-X Ag-target X-ray source at 40 kV and 99  $\mu\text{A}$ .

Spectral data of capillaries were obtained at 10 s exposure time and capillaries sandwiched in between 4 mm porcine tissue were obtained at 60 s exposure time.

X-ray excited luminescence chemical imaging (XELCI) of these capillaries was done without tissue and with 5 mm porcine tissue. The capillaries were scanned with 250  $\mu\text{m}$  step size and 1 mm  $\text{s}^{-1}$  for a high-resolution scan. For imaging without tissue, the X-ray source was set to 50 kV and 200  $\mu\text{A}$ ; 50 kV and 600  $\mu\text{A}$  was used for imaging with porcine tissue. Data were analyzed and plotted using custom MATLAB scripts.

### 3.3.6. MR imaging of $\text{NaGdF}_4\text{:Eu}$ and $\text{Tb}$

Solutions of  $\text{NaGdF}_4\text{:Eu}$  and  $\text{Tb}$  nanophosphors at a series of concentrations from 0 to 0.4 mM were prepared by dissolving in DI water. MR imaging and relaxometry was done on a 3T Siemens MAGNATOM Prisma MRI instrument (Siemens Healthineers, Erlangen, Germany).  $T_1$ -weighted images were acquired using a 2D spin echo sequence with repetition time (TR) 25 ms and echo time (TE) 5.9 ms.  $T_2$ -weighted images were acquired using a turbo spin echo sequence with TR = 3200 ms and TE = 29 ms.  $T_1$  was measured with an inversion recovery experiment using a spin echo pulse sequence. Inversion times (TI) were 25, 50, 400, 1100, and 2500 ms. To calculate  $T_1$ , the model from ref. <sup>33</sup> was fit to MR signal magnitude vs. TI using the qMRLab package for MATLAB.<sup>34</sup>  $T_2$  was measured with a multi-echo spin echo sequence using 32 TEs ranging from 15 to 960 ms. To calculate  $T_2$ , a monoexponential model  $S(TE) = M_0 \exp\left(-\frac{TE}{T_2}\right)$  was fit to MR signal magnitude vs. TE. Relaxivities were calculated by linear regression of  $R_1 = 1/T_1$ ,  $R_2 = 1/T_2$  vs. nanoparticle concentration.

### 3.3.7. *Transmission electron microscopy*

The synthesized, silica-coated and annealed nanoparticles were deposited on a formvar/carbon-coated copper grids from a water solution and dried before taking the transmission electron micrographs from Hitachi HT7800 operating at 20–120 keV and 8  $\mu$ A.

### 3.3.8. *Powder X-ray diffraction (XRD)*

The phases of the NaGdF<sub>4</sub>:Eu powders, nanoparticles, and annealed nanoparticles were characterized by Rigaku Ultima IV powder diffractometer, using Cu K $\alpha$  radiation. Powdered samples were spread on a low background glass slide and data are collected in 0.02° increments at a rate of 0.5–1° per minute from 10° to 70° at room temperature. Annealed particles were measured at 0.2–0.5° per minute.

### 3.3.9. *X-ray excited optical luminescence (XEOL) spectroscopy*

X-ray luminescence of all the nanoparticles was measured by irradiating with an X-ray beam. A 96 well plate containing dried and powdered nanoparticles was placed on the stage of an inverted microscope (Leica microscope) and irradiated with an X-ray beam generated using a Mini-X (Ag) X-ray source (Amptek, Bedford, MA) set at 40 kV and 99  $\mu$ A. The emission of nanoparticles was collected by 5x objective and focused to a spectrograph (DNS 300, DeltaNu, Laramie, WY, USA), equipped with a cooled CCD camera (iDUS-420BV, Andor, South Windsor, CT, United States).

#### *3.3.10. ICP-OES metal analysis*

The percentage of metals (Gd, Eu and Tb) in the final systems were measured using iCAP 7200 MSC ICP-OES analyzer. Nanophosphors were dissolved in 2% HNO<sub>3</sub> to prepare nitrates of the metals. The standard metal solutions were prepared from 0.1 to 100 ppm range. The samples and the standards were injected to ICP-OES and quantified the amount of metal using instrument software (Qtegra ISDS software). The wavelengths of the corresponding spectrometric lines that used for the analysis were Gd: 335 nm, Eu: 381 nm, Tb: 350 nm. The metal percentages (Eu/Gd and Tb/Gd) from the dissolved samples were calculated using standard curves.

#### *3.3.11. Thermal analysis: TGA/DSC*

TGA and DSC measurements were carried out on a SDT Q600 V20.9 Build 20 thermal gravimetric by TA instruments. Nanophosphor samples in alumina crucibles were heated up to 700 °C at a rate of 20 °C minute<sup>-1</sup> under N<sub>2</sub> gas flow. At 700 °C samples were kept under isothermal conditions and flushed with air. TGA and DSC measurements were collected simultaneously.

### **3.4. Results and Discussion**

We synthesized NaGdF<sub>4</sub>:Eu and NaGdF<sub>4</sub>:Tb nanophosphors via co-precipitation and hydrothermal methods and studied the effect of dopant concentration on their optical spectra and crystal diffraction patterns. Next, we encapsulated the nanophosphors in silica to prevent thermal sintering and studied the effect of thermal treatment. We functionalized the nanophosphors with biotin and showed that we could excite colloidal

suspensions of particles with a focused X-ray beam to image the luminescence through tissue. Finally, we explored the possibility of multimodal imaging based on spectrally distinct features of the nanophosphors and MRI contrast.

#### *3.4.1. NaGdF<sub>4</sub>:Eu and NaGdF<sub>4</sub>:Tb nanoparticle synthesis*

In the NaGdF<sub>4</sub> nanophosphor synthesis, citrate acts as a complexing and dispersing agent that forms a La<sup>3+</sup>–Cit<sup>3–</sup> complex and disperses in deionized (DI) water. Upon addition of excess NaF, La<sup>3+</sup> released from the complex reacts with Na<sup>+</sup> and F<sup>–</sup> to form NaGdF<sub>4</sub> nuclei. After forming NaGdF<sub>4</sub>:Eu and Tb, the citrate serves as a surfactant that controls nanoparticle growth and prevents aggregation.<sup>15,35</sup>

**Co-precipitate synthesis method.** The co-precipitate synthesis process is presented in Figure 3.1A. The nanophosphors synthesized using the co-precipitate method at room temperature were approximately spherical in shape (Figure 3.1B1 and C1). The Eu-doped and Tb-doped nanophosphors respectively had average diameters of ~90 nm (Figure 3.1A2) and 106 nm (Figure 3.1C2), respectively. The powder X-ray diffraction (powder-XRD) peaks displayed the presence of cubic (β-phase) NaGdF<sub>4</sub> (Figure 3.1B3 and C3) indexed to the standard data (JCPDS 00-027-0699), with relatively large peak with indicating small crystal domain sizes (~55 Å NaGdF<sub>4</sub>:Eu and ~53 Å NaGdF<sub>4</sub>:Tb according to the Scherrer equation based on peak at 16.8 degrees).



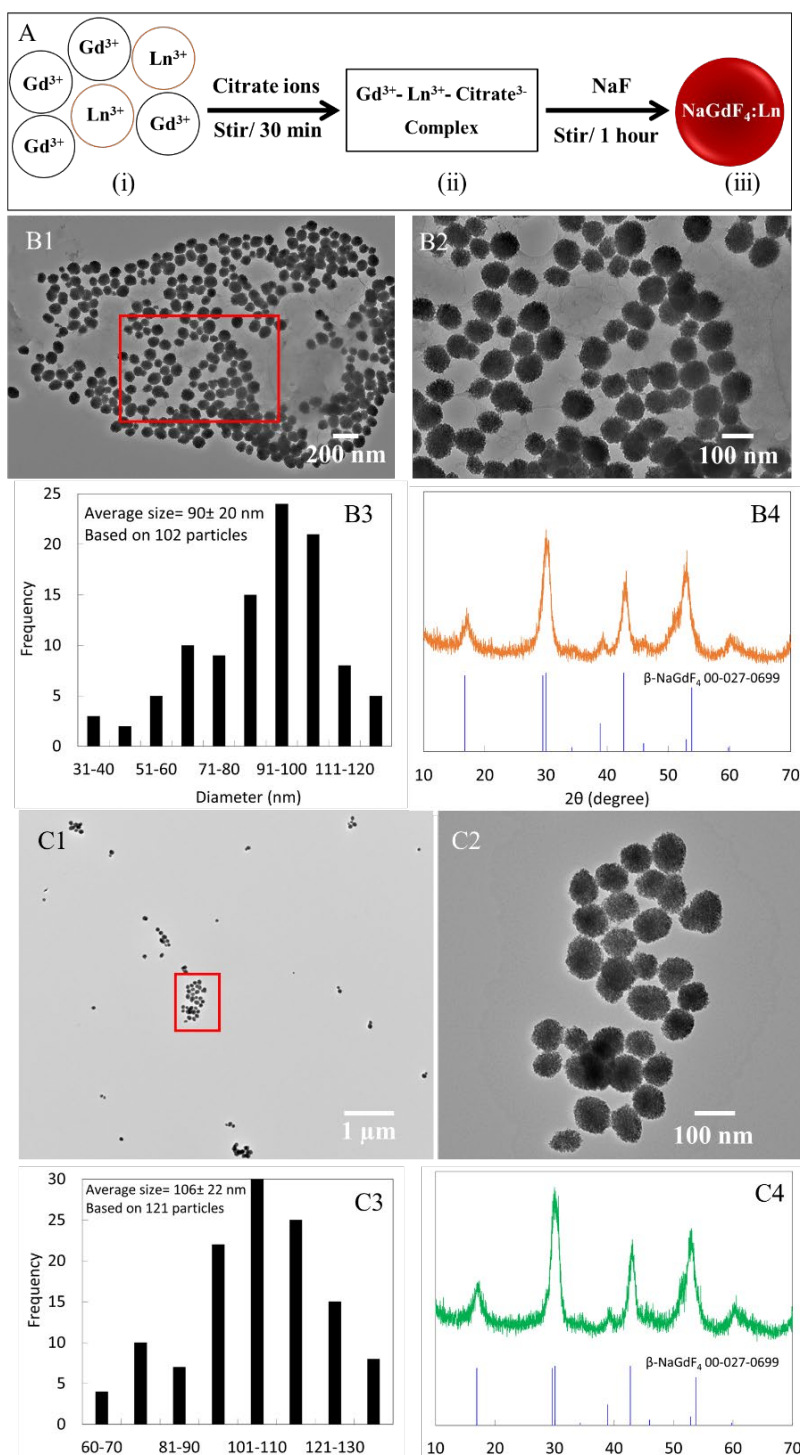


**Figure 3. 1: (A) Schematic illustration of nanophosphors synthesis according to co-precipitate method. (i) Mixture of  $Gd(NO_3)_3$  and  $Eu(NO_3)_3$  or  $Tb(NO_3)_3$ , (ii)  $Ln^{3+}$ -citrate $^{3-}$  complex appears as a clear solution, (iii) formation of  $NaGdF_4:Ln^{3+}$  nanophosphors. Zoom out TEM images of (B1)  $NaGdF_4:Eu$  and (C1)  $NaGdF_4:Tb$  nanophosphors. Zoom in TEM images of (B2)  $NaGdF_4:Eu$  and (C2)  $NaGdF_4:Tb$  nanophosphors. Histograms of the average diameter of (B3)  $NaGdF_4:Eu$  and (C3)  $NaGdF_4:Tb$ . Powder XRD pattern compared to PDF cards 27-0699 of (B4)  $NaGdF_4:Eu$  and (C4)  $NaGdF_4:Tb$ . Taken with permission of ref 1.**

TEM images and powder-XRD patterns of Eu- and Tb-doped NaGdF<sub>4</sub> (0.1, 1, 15, 20 and 100%) are included in figure 3.2.

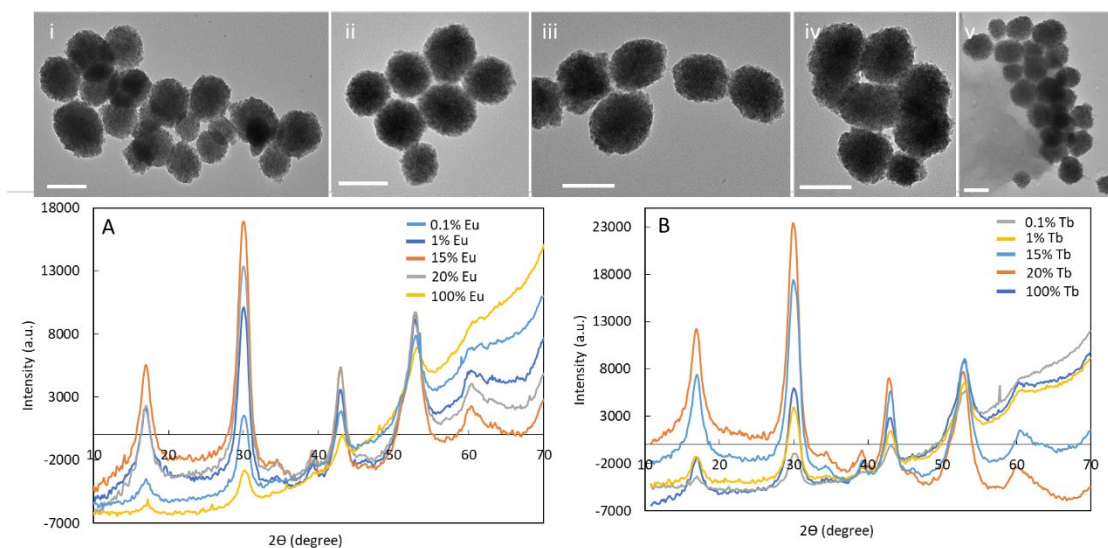


**Figure 3. 2:** TEM images of NaGdF<sub>4</sub> doped with (i) 0.1%, (ii) 1%, (iii) 15%, (iv) 20%, (v) 100% Eu synthesized using the co-precipitate method. Scale bar is equal to 100 nm. XRD patterns of (A) Eu and (B) Tb-doped NaGdF<sub>4</sub> (Gd: dopant molar ratio= 1: 0.1, 1, 15, 20, 100%). XRD data were collected using single-crystal XRD as an alternative of powder XRD. PDF card is 27-0699. Taken with permission of ref 1.

The synthesized nanophosphors show powder-XRD peak shift compared to standard peak positions (e.g., peaks at around 53° in Figure 3.1). This observation is common in most powder-XRD patterns due to changes in stoichiometric composition by doping (size and amount of dopant), microstructure parameters (crystallite size and lattice strain).<sup>36</sup> X-ray luminescence nanophosphors with low emission intensity are used in X-ray luminescence computer tomography (XLCT) and focused X-ray luminescence tomography (FXLT).<sup>11</sup>

The optical properties of rare-earth-doped nanophosphors depend upon the doping ions and crystalline matrix. Figure 3.3 shows the X-ray excited optical luminescence spectrum of NaGdF<sub>4</sub>:Eu. There are three characteristic peaks in the visible range of the

electromagnetic spectrum, at around 589 nm, 615 nm, and 691 nm, that correspond to  $^5D_0 \rightarrow ^7F_1$ ,  $^5D_0 \rightarrow ^7F_2$ ,  $^5D_0 \rightarrow ^7F_4$  transitions.<sup>10,14</sup> Tb doped NaGdF<sub>4</sub> has four characteristic peaks in the visible range, at around 489 nm, 543 nm, 585 nm, and 620 nm corresponding to  $^5D_4 \rightarrow ^7F_6$ ,  $^5D_4 \rightarrow ^7F_5$ ,  $^5D_4 \rightarrow ^7F_4$ ,  $^5D_4 \rightarrow ^7F_3$  transitions.<sup>10,37</sup> Since the luminescence intensity depends upon dopant concentration,<sup>38,39</sup> we varied the amount of Eu and Tb compared to Gd<sup>3+</sup> in the reaction mixture. Figures 3.3A and B show the luminescence spectra for Eu- and Tb-doped nanophosphors, respectively. The dopant:Gd molar concentration ratios in the NaGdF<sub>4</sub> synthesis reaction were 0.1% (bottom), 1%, 15%, 20% and 100% (top). A base value has been added to each spectrum to avoid spectral overlapping. At low and high molar ratios of both Eu and Tb doped NaGdF<sub>4</sub> nanophosphors showed low luminescence intensity due to lack of luminescence centers and self-quenching (cross-relaxation between two neighboring Eu<sup>3+</sup>),<sup>38</sup> respectively. Intermediate concentrations, 1%, 15%, and 20% in Eu-doped NaGdF<sub>4</sub> showed the highest although similar luminescence intensities. In Tb-doped NaGdF<sub>4</sub> 20% showed the highest intensity.

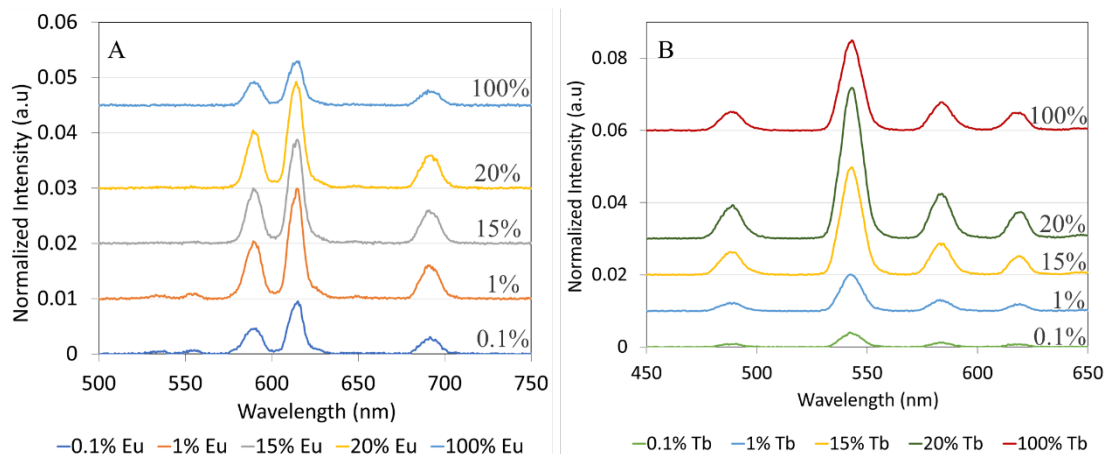


**Figure 3. 3: X-ray excited optical luminescence (XEOL) of (A) NaGdF<sub>4</sub>:Eu and (B) NaGdF<sub>4</sub>:Tb nanophosphors. Eu and Tb dopant fraction (mol% added to reagents vs. Gd) of NaGdF<sub>4</sub> nanophosphors varied from 0.1% to 100%. X-ray luminescence intensities of nanophosphors were normalized to the 620 nm peak intensity from commercial GOS:Eu and Tb microphosphors. Spectra have been vertically displaced for ease of comparison. Taken with permission of ref 1.**

**Hydrothermal synthesis method.** The hydrothermal synthesis process is presented in Figure 3.4A. The crystallinity of inorganic crystals plays an important role in X-ray luminescence intensity, where a large crystal domain size results in high luminescence intensity.<sup>10</sup> During the hydrothermal process, nanophosphors recrystallize to rearrange the crystal structure. The nanophosphors synthesized using the co-precipitate method at room temperature were hydrothermally treated to increase the crystallinity and enhance the X-ray luminescence intensity. The hydrothermally treated nanophosphors were irregularly shaped (Figure 3.4B1 and B2) as nanophosphors are starting to aggregate and fuse at high temperature. However, narrow peaks in the powder XRD pattern (Figure 3.4B3) confirmed the increased crystallinity compared to nanophosphors synthesized at room temperature. ( $\sim 179$  Å NaGdF<sub>4</sub>:Eu and  $\sim 128$  Å NaGdF<sub>4</sub>:Tb according to the Scherrer equation based on the peak at 17 degrees).

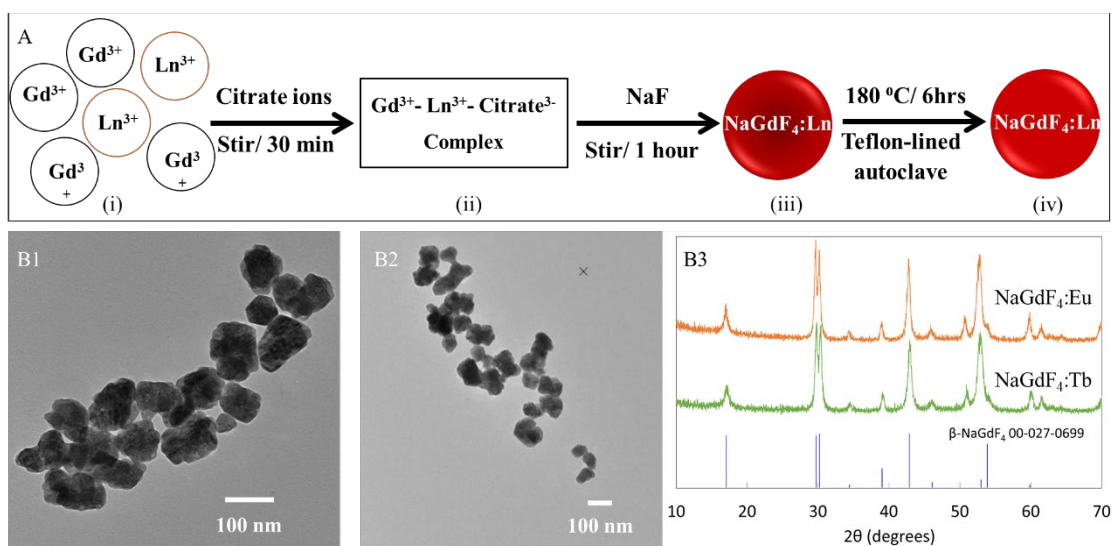


**Figure 3. 4: (A) Schematic illustration of nanophosphors synthesis according to co-precipitate method. (i) Mixture of  $Gd(NO_3)_3$  and  $Eu(NO_3)_3$  or  $Tb(NO_3)_3$ , (ii)  $Ln^{3+}$ -citrate $^{3-}$  complex appears as a clear solution, (iii) formation of  $NaGdF_4:Ln^{3+}$  nanophosphors, (iv) hydrothermally treated  $NaGdF_4:Ln^{3+}$  nanophosphors. TEM images of hydrothermally treated (B1)  $NaGdF_4:Eu$  and (B2)  $NaGdF_4:Tb$  nanophosphors. (B3) Powder XRD pattern compared to PDF cards 27-0699 of  $NaGdF_4:Eu$  and  $NaGdF_4:Tb$ . Taken with permission of ref 1.**

TEM images and powder-XRD patterns of 0.1–100% Eu- and Tb-doped

$NaGdF_4$  are included in Figure 3.5.

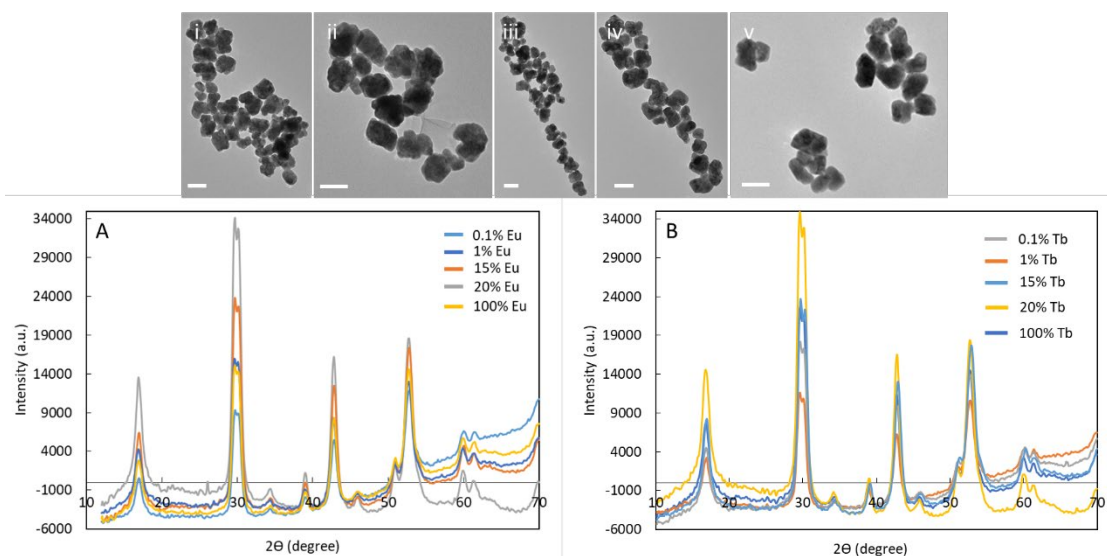


**Figure 3. 5: TEM images of  $NaGdF_4$  doped with (i) 0.1%, (ii) 1%, (iii) 15%, (iv) 20%, (v) 100% Eu synthesized using the hydrothermal method. Scale bar is equal to 100 nm. XRD patterns of (A) Eu- and (B) Tb-doped  $NaGdF_4$  (Gd: dopant molar ratio= 1: 0.1, 1, 15, 20, 100%). XRD data were collected using single-crystal XRD as an alternative of powder XRD. PDF card is 27-0699. Taken with permission of ref 1.**

Hydrothermally treated nanophosphors showed enhanced X-ray luminescence intensity by a factor of 2–2.5 compared to nanophosphors synthesized at room temperature. 15% Eu doped NaGdF<sub>4</sub> showed the highest intensity. However, 1% and 20% Eu doped NaGdF<sub>4</sub> showed high values close to the highest intensity ( Figure. 3.6A). The X-ray luminescence intensity of 15% Tb doped NaGdF<sub>4</sub> had the highest intensity, and 20% Tb doped NaGdF<sub>4</sub> showed an intensity close to the highest value (Figure. 3.6B).

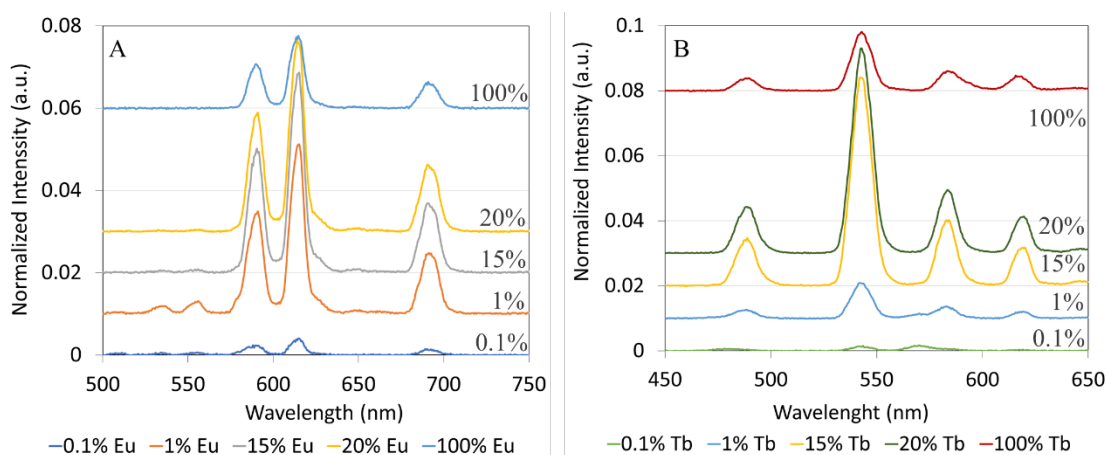


**Figure 3. 6: XEOL of hydrothermally treated (A) NaGdF<sub>4</sub>:Eu and (B) NaGdF<sub>4</sub>:Tb nanophosphor. Mol fraction of Eu and Tb dopant vs. Gd in regent mixture varied from 0.1% to 100%. X-ray luminescence intensities of nanophosphors were normalized to the height of 620 nm peak of commercial GOS:Eu and Tb microparticles. Spectra have been vertically displaced by adding a baseline for ease of comparison. Taken with permission of ref 1.**

#### 3.4.2. Inductive coupled plasma-optical emission spectroscopy (ICP-OES) metal analysis

ICP-OES analysis was performed for Gd, Eu and Tb to determine the Eu/Gd and Tb/Gd ratios of the synthesized nanophosphors, which determine X-ray luminescence intensity. All four types of samples (NaGdF<sub>4</sub>:Eu and NaGdF<sub>4</sub>:Tb synthesized by co-precipitate and hydrothermal methods) show an increased percent metal ratio as the fraction of dopant added increases. The amount of dopant in the final systems was

directly proportional to amount added to the reagent mix, with a slope of 1.2 for both the coprecipitated and hydrothermal NaGdF<sub>4</sub>:Eu (i.e., nanophosphors incorporated 20% more Eu than was added to the reagent mixture) and 1.3 for the NaGdF<sub>4</sub>:Tb (i.e., nanophosphors incorporated 30% more Eu than was added to the reagent mixture), suggesting increases in thermodynamic stability or kinetic reaction rates during synthesis.

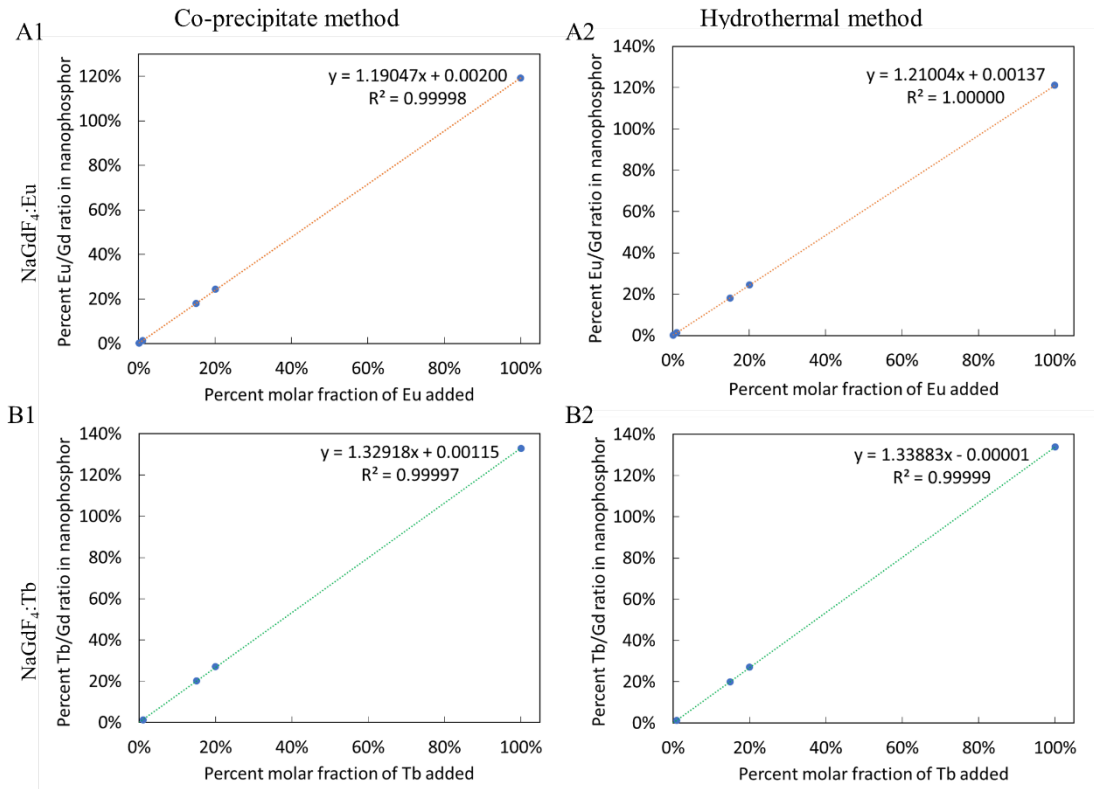


**Figure 3. 7: Metal composition of nanophosphors calculated using ICP-OES measurements. The graph of percent metal ratio of nanophosphor vs. percent molar fraction of dopant added of NaGdF<sub>4</sub>:Eu synthesized by (A1) co-precipitate and (A2) hydrothermal methods and NaGdF<sub>4</sub>:Tb synthesized by (B1) co-precipitate and (B2) hydrothermal methods. Note, the amount of Tb in NaGdF<sub>4</sub>:0.1%Tb was not calculated as it is lower than the limit of detection of the instrument. Take with permission of ref 1.**



### 3.4.3. Silica-coating NaGdF<sub>4</sub>:Eu and Tb nanophosphors

NaGdF<sub>4</sub>:Eu nanophosphors, synthesized at room temperature, were coated with silica before further experiments. The silica can protect nanophosphors from aggregation and facilitate functionalization for biological applications. Figure 3.8A presents the NaGdF<sub>4</sub> silica coating process. In electron microscopy images ( Figure 3.8B1) the silica coating appeared as a ~15 nm thick shell around the nanophosphors. The average diameter of NaGdF<sub>4</sub>:Eu@SiO<sub>2</sub> nanophosphors was about 120 nm ( Figure 3.8B2).

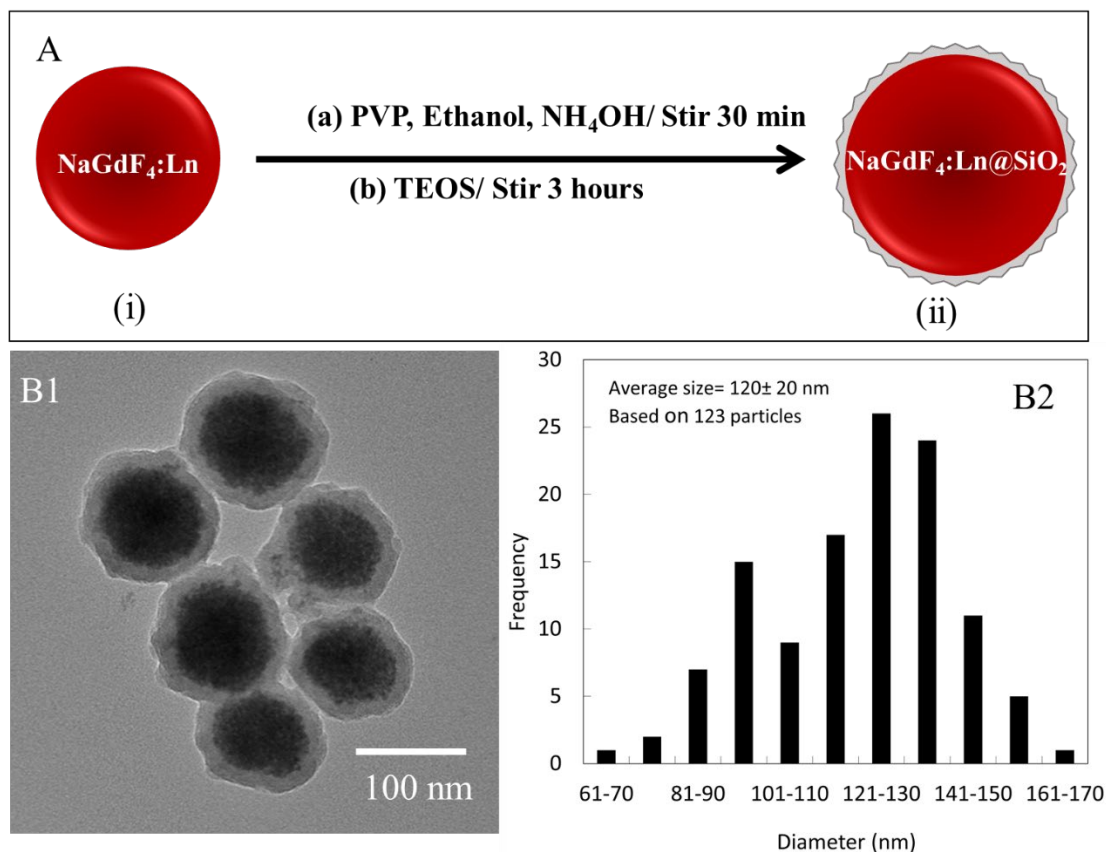


**Figure 3. 8:** (A) Schematic illustration of nanoparticle coating with silica. (i) NaGdF<sub>4</sub>:Ln<sup>3+</sup> nanophosphors, (ii) silica-coated NaGdF<sub>4</sub>:Ln<sup>3+</sup> nanoparticles. (B1) TEM images of silica-coated NaGdF<sub>4</sub> nanophosphors Eu-doped. (B2) Histograms of the diameter of silica-coated NaGdF<sub>4</sub>:Ln<sup>3+</sup> nanoparticles. (B1) TEM images of silica-coated NaGdF<sub>4</sub> nanophosphors Eu-doped. (B2) Histograms of the diameter of silica-coated NaGdF<sub>4</sub>:Eu. Take with permission of ref 1.



Both Tb-doped and Eu-doped nanophosphors showed reduced X-ray luminescence after coating with silica for the same mass of material. After coating, the NaGdF<sub>4</sub>:Eu nanophosphors reduced intensity by ~42% (Figure 3.9A). This is explained mainly by the additional silica, which increased the mass by 65% (based on particle diameter, coating thickness, and density of NaGdF<sub>4</sub> core and silica shell) while not providing any additional luminescent material.

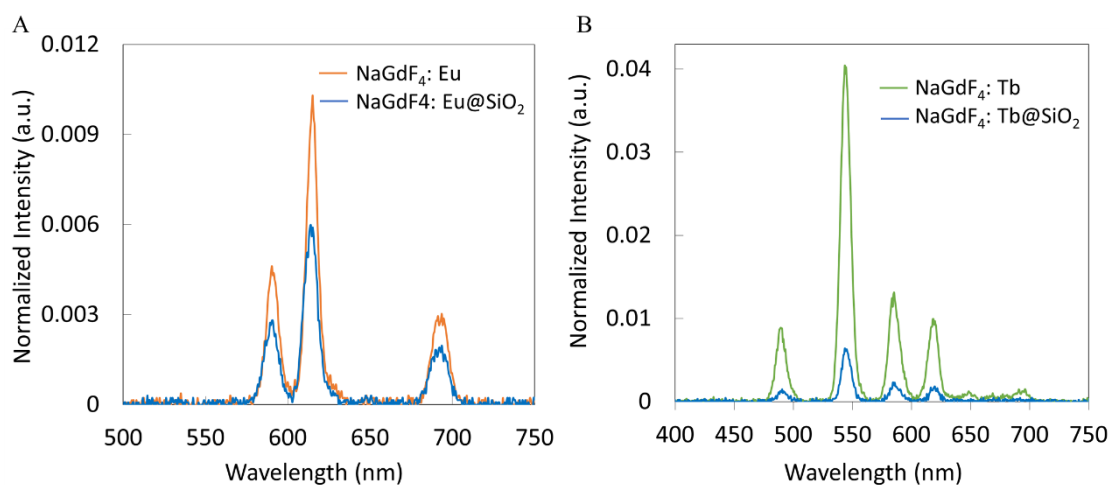


**Figure 3. 9: XEOL spectra of silica-coated (A) NaGdF<sub>4</sub>:Eu and (B) NaGdF<sub>4</sub>:Tb compared to NaGdF<sub>4</sub>:Eu and NaGdF<sub>4</sub>:Tb synthesized using co-precipitate method. Taken with permission of ref 1.**

#### 3.4.4. Thermal analysis

The stability of the nanophosphors towards heat was studied by thermal gravimetric analysis (TGA) and differential scanning calorimetry (DSC) thermograms as in Figure 3.10A and B. NaGdF<sub>4</sub>:Eu and NaGdF<sub>4</sub>:Tb synthesized using co-precipitate method showed total weight loss of 12.5% and 12.1% respectively. Their highest weight loss appeared at 62.5 °C is attributed to the loss of trapped H<sub>2</sub>O, and weight loss above 250 °C may cause by the decomposition of citrate. The nanophosphors synthesized using the

hydrothermal method indicated 3.10% (NaGdF<sub>4</sub>:Eu) and 5.17% (NaGdF<sub>4</sub>:Tb) total weight loss. The vaporization of trapped H<sub>2</sub>O causes no significant weight loss. Also, the weight loss above 250 °C is less intense than the weight loss of the co-precipitate method. Silica coated-NaGdF<sub>4</sub>:Eu has a total weight loss of 17.4%. Its weight loss at 65.5 °C is attributed to the loss of trapped H<sub>2</sub>O and ethanol.

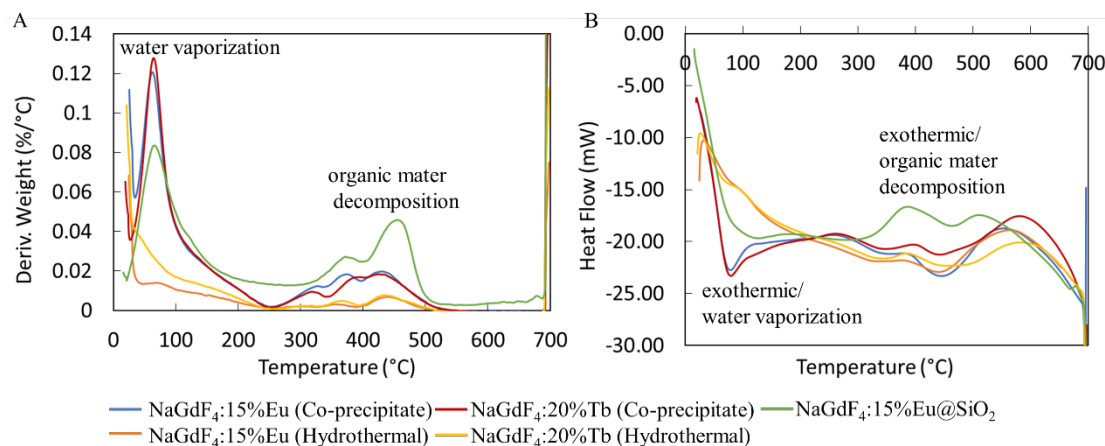


**Figure 3. 10:(A) TGA and (B) DSC of NaGdF<sub>4</sub>:Eu and NaGdF<sub>4</sub>:Tb nanophosphors synthesized using co-precipitate and hydrothermal methods and NaGdF<sub>4</sub>:Eu@SiO<sub>2</sub>. Taken with permission of ref 1.**

The peaks above 250 °C are more intense than for uncoated nanophosphors and likely caused by decomposition of citrate and PVP organic materials (Figure 3.11B and C).

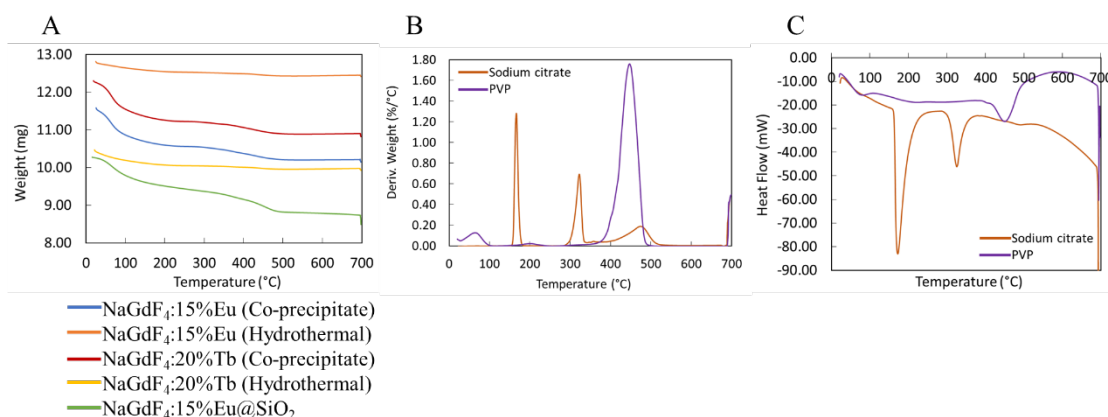


**Figure 3. 11: TGA thermograms showing (A) weight loss of synthesized nanophosphors, (B) derivative of weight loss (C) DSC of sodium citrate and PVP. Taken with permission of ref 1.**

Further, a DSC thermogram shows that vaporization and decomposition are exothermic processes. The TGA thermogram shows that nanophosphors synthesized by the hydrothermal method contain less trapped water and organic materials, which may result in high X-ray luminescence intensity.

#### 3.4.5. Annealing *NaGdF<sub>4</sub>:Eu* nanophosphors

Nanophosphors synthesized using the co-precipitate method and coated with silica have relatively low luminescence intensity, hindering most in vivo applications such as deep tissue imaging and implantable biosensors. High-temperature annealing could enhance luminescence by removing crystal defects, increasing crystal domain size, and removing trapped water and carbon dioxide.<sup>23,24</sup> Unfortunately, when we annealed our nanophosphors at temperatures above 700 °C, the particles sintered. For example, Figure 3.12 shows that after thermal annealing at 1000 °C, the *NaGdF<sub>4</sub>:Eu* nanophosphors aggregated and fused, making a structure too large for many biological applications.

However, the luminescence intensity was increased by a factor of  $\sim 7$  compared to nanophosphors synthesized by the co-precipitate method.

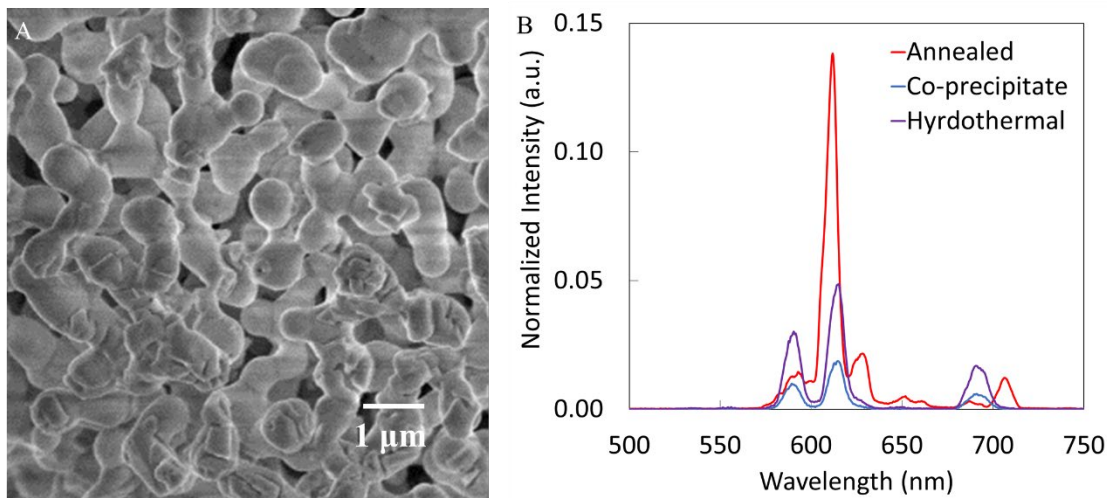


**Figure 3. 12: (A) SEM image and (B) XEOL of NaGdF<sub>4</sub>:Eu annealed at 1000 °C for 6 h compared to NaGdF<sub>4</sub>:Eu nanophosphors synthesized using co-precipitate and hydrothermal methods. Taken with permission of ref 1.**

Silica coating can act as a protective layer, preventing particles from aggregating and fusing during the annealing process.<sup>24</sup> Annealed nanophosphors at 400 °C (Figure 3.13A) showed separate particles with a thin silica coating. Annealing at 600 °C (Figure 3.13B) showed single and separate nanophosphors with a silica shell and nanophosphor core, but the core had compressed, and some void space was apparent. Annealing at 1000 °C (Figure 3.13C) caused the nanophosphors to aggregate, although not to the extent of forming the large porous structures observed without coating (Figure 3.12A).

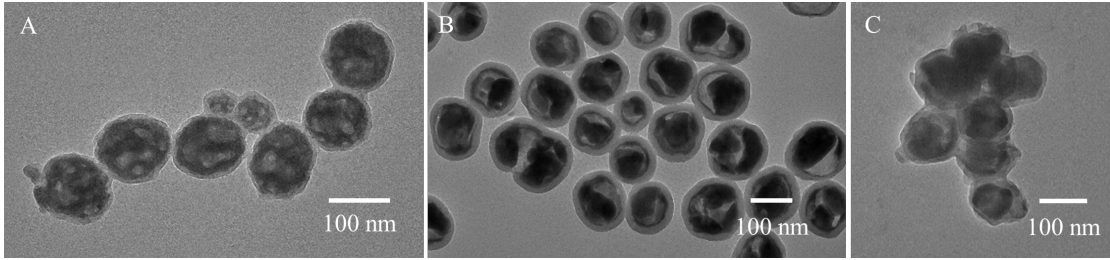


**Figure 3. 13: TEM images of NaGdF<sub>4</sub>:Eu@SiO<sub>2</sub> nanophosphors annealed at (A) 400 °C, (B) 600 °C (C) 1000 °C. Taken with permission of ref 1.**

Annealing at 400 °C and 1000 °C increased the luminescence intensity by a factor of  $\sim 1.5$  and  $\sim 3$  compared to unannealed silica-coated nanophosphors. Among the three annealing temperatures, 1000 °C showed the highest intensity ( Figure 3.14A).

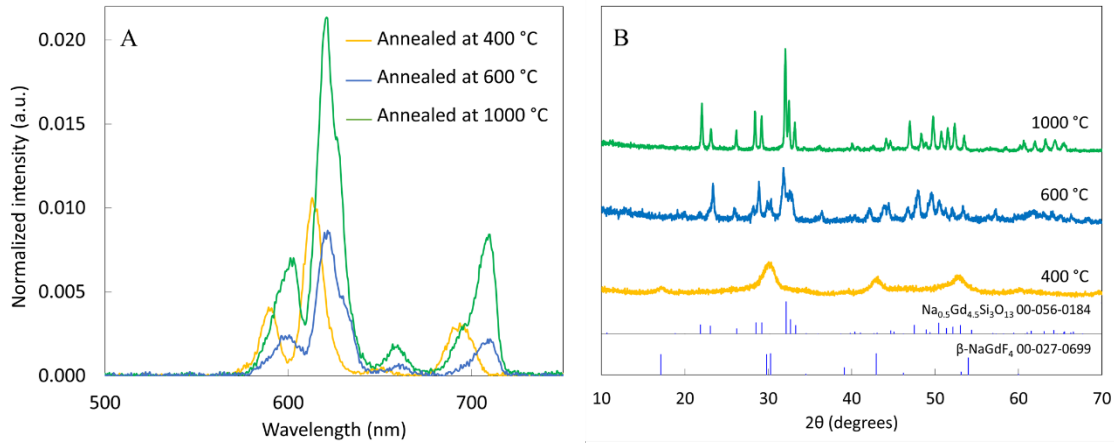


**Figure 3. 14: (A) XEOL of NaGdF<sub>4</sub>:Eu@SiO<sub>2</sub> annealed at 400 °C, 600 °C and 1000 °C for 6 h. (B) Powder XRD pattern of annealed NaGdF<sub>4</sub>:Eu@SiO<sub>2</sub> at 600 °C and 1000 °C compared to PDF cards 00-056-0184 and 00-027-0699 biotin functionalized NaGdF<sub>4</sub>:Eu@SiO<sub>2</sub>. Taken with permission of ref 1.**

We also observed that the XEOL spectrum red-shifted at high temperatures (600 °C and 1000 °C). This spectral shift could potentially be useful for generating nanophosphors with distinguishable spectra for multi-modal imaging and likely arises from changes in composition and crystal field. A potential future direction with spectrally distinguish

NaGdF<sub>4</sub>:Eu and Gd<sub>2</sub>O<sub>2</sub>S: Eu is explained in chapter 6. (XEOL graphs of synthesized, annealed, and silica-coated NPs are included in Figure 3.15 to compare).

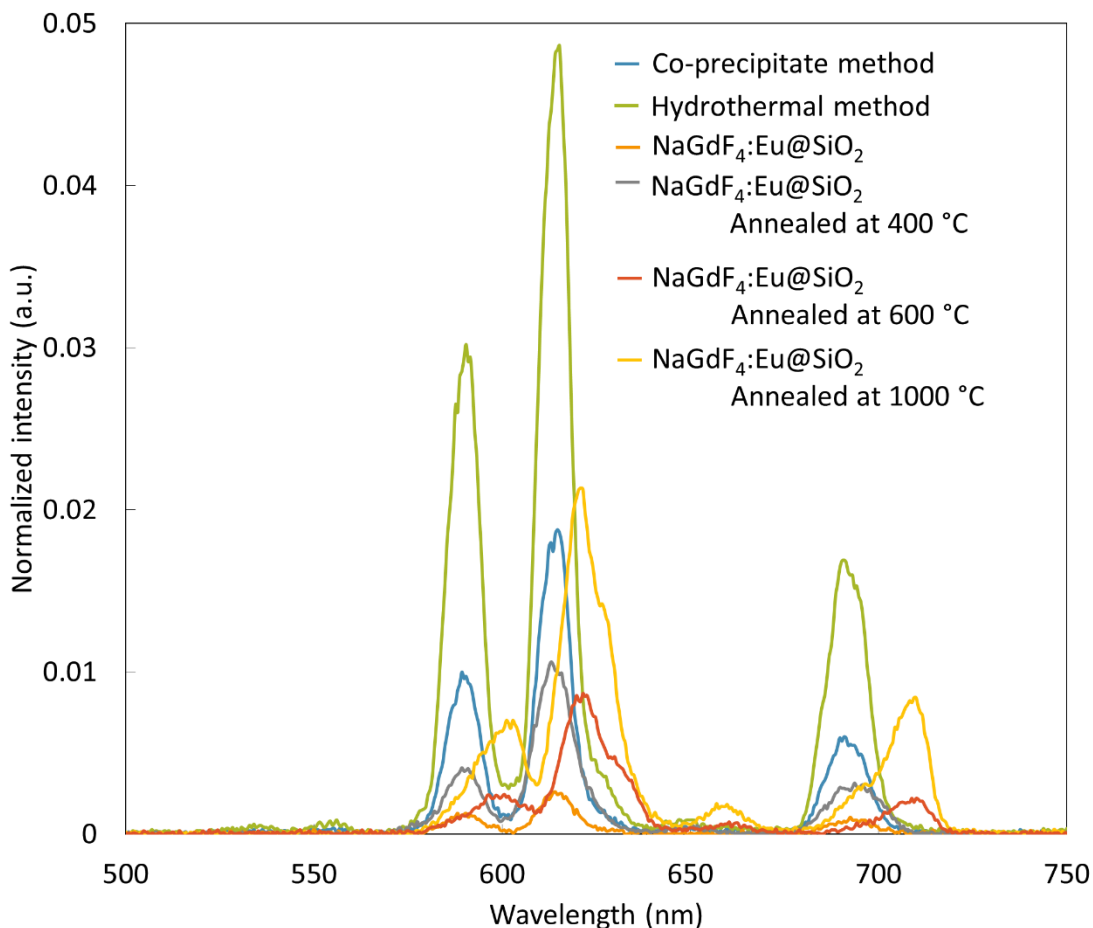


**Figure 3. 15:** X-ray excited optical luminescence (XEOL) spectra of bare synthesized, silica coated, and silica coated annealed Eu-doped NaGdF<sub>4</sub> NPs. Taken with permission of ref 1.

Indeed, powder-XRD data confirmed the formation of sodium gadolinium silicate compound by reacting with the silica layer: XRD spectra display the presence of NaGd<sub>9</sub>Si<sub>6</sub>O<sub>26</sub>:Eu (Figure 3.14B) indexed to the standard data (JCPDS 00-056-0184). Additionally, we observed that the 1000 °C annealed samples have sharper diffraction peaks indicating larger crystal domains, likely reducing quenching from the surface and

defects.<sup>10</sup> Also, at 1000 °C, the nanophosphors have started to aggregate. On balance, the 1000 °C annealing appeared to give the best performance, albeit with a spectral shift.

XEOL graphs of NaGdF<sub>4</sub>:15%Eu annealed at 150, 400, and 1000 °C for 12 h are included in Figure 3.16.

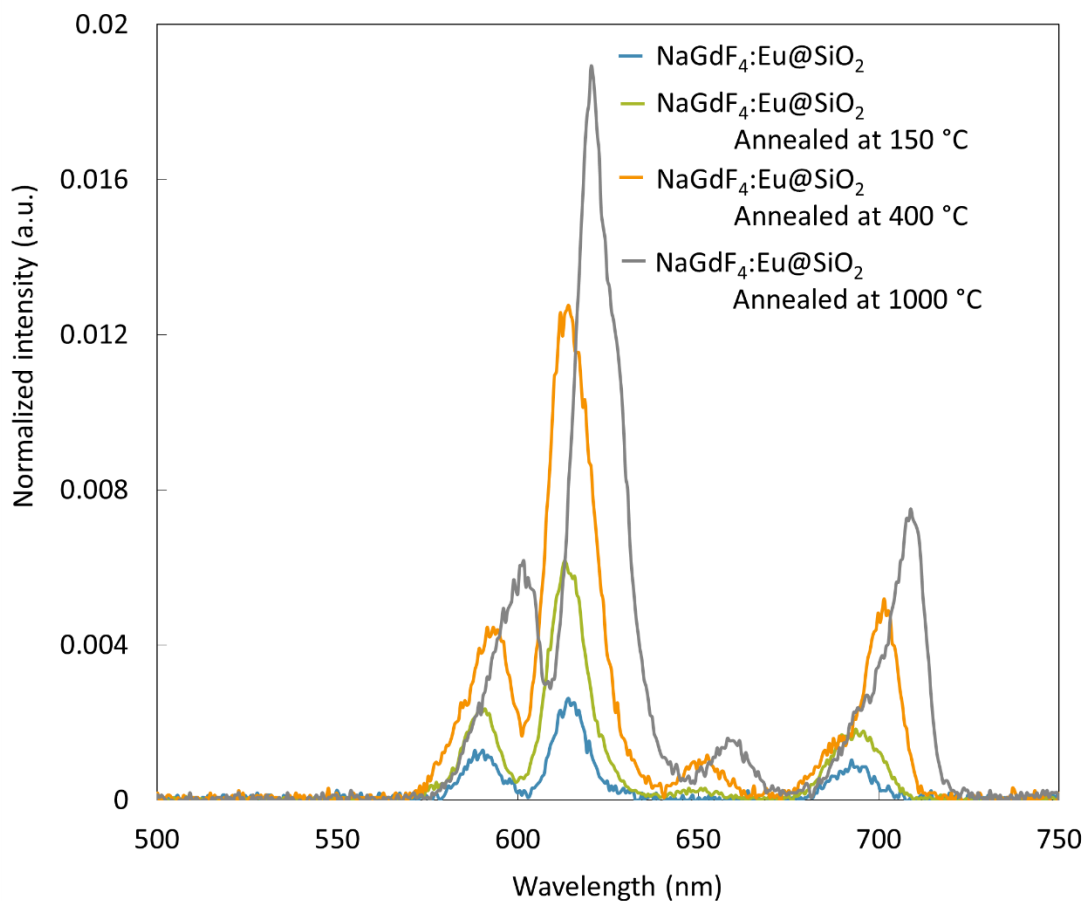


**Figure 3. 16: XEOL spectra of NaGdF<sub>4</sub>:Eu@SiO<sub>2</sub> unannealed and annealed at 150, 400, and 1000 °C for 12 hours. Taken with permission of ref 1.**

#### 3.4.6. Biotin functionalized NaGdF<sub>4</sub>:Eu@SiO<sub>2</sub>

Functionalizing rare-earth-doped nanophosphors is important *in vivo* labeling and imaging, biological assays, and sensor applications with specific targets such as proteins

and DNA.<sup>12,40,41</sup> We functionalized NaGdF<sub>4</sub>:Eu@SiO<sub>2</sub> nanophosphors (not annealed) with a mixture of PEG-phosphate and biotin-PEG. The PEG-phosphate was chosen to have good dispersion of surface-modified nanophosphors in water at physiological pH and high ionic strength (PBS buffer). The biotin-functionalization was demonstrated by attachment to streptavidin-functionalized buoyant silica microbubbles (Figure 3.17).

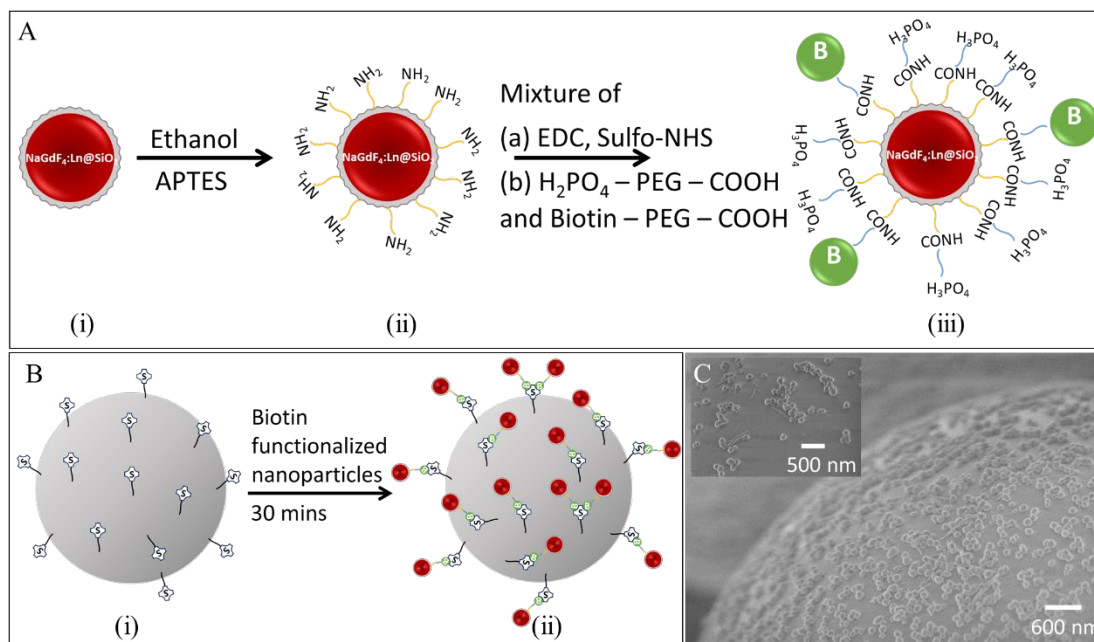


**Figure 3. 17: Schematic illustration of (A) silica coated nanophosphors functionalized with biotin (i) silica-coated NaGdF<sub>4</sub>:Eu nanophosphors, (ii) amine-functionalized nanophosphors, (iii) biotin-functionalized nanophosphors. Biotin is connected to amine-functionalized nanophosphors via sulfo-NHS groups, (B) biotin functionalized nanophosphors attach to streptavidin coated silica microbubbles. (i) streptavidin-coated silica microbubbles, (ii) biotin-functionalized nanophosphors attached to streptavidin-coated silica microbubbles. (C) SEM image showing biotin-functionalized nanophosphors attached to streptavidin-coated microbubbles. Taken with permission of ref 1.**

#### 3.4.7. X-ray excited optical luminescence spectroscopy and imaging of capillaries filled with NaGdF<sub>4</sub>:Eu through tissue

XEOL spectroscopy and imaging were performed to demonstrate the ability to excite the nanophosphors through tissue and show that the luminescence could be generated in specific regions using a focused X-ray source. We chose 5 mm of chicken



breast because 5 mm is sufficient for many applications in a mouse model where the “radius” is <1 cm, and we used chicken breast because it is a common tissue material that scatters light. Optical scattering in chicken breast is highly anisotropic and has larger transport mean free path (the length over which the direction of photon propagation is randomized) than scattering mean free path.<sup>42</sup>

XEOL spectroscopy of colloidal NaGdF<sub>4</sub>:Eu nanophosphors in capillaries was measured with and without being sandwiched between two 4 mm porcine tissue. Figures 3.18A1 and B1 show a schematic illustration of the experimental setup. The glass slide carrying capillaries (1 mm diameter) filled with a nanoparticle solution (0, 50, 100 mg mL<sup>-1</sup>) is placed on the microscope stage. The light generated in X-ray irradiated nanophosphors was collected through a microscope lens and sent to a spectrograph. Spectra generated without tissue (Figure 3.18A2) shows intensity higher than capillaries sandwiched between porcine tissues (Figure 3.18B2). Also, as the concentration of nanophosphors increases, the capillary intensity increases in both scenarios.

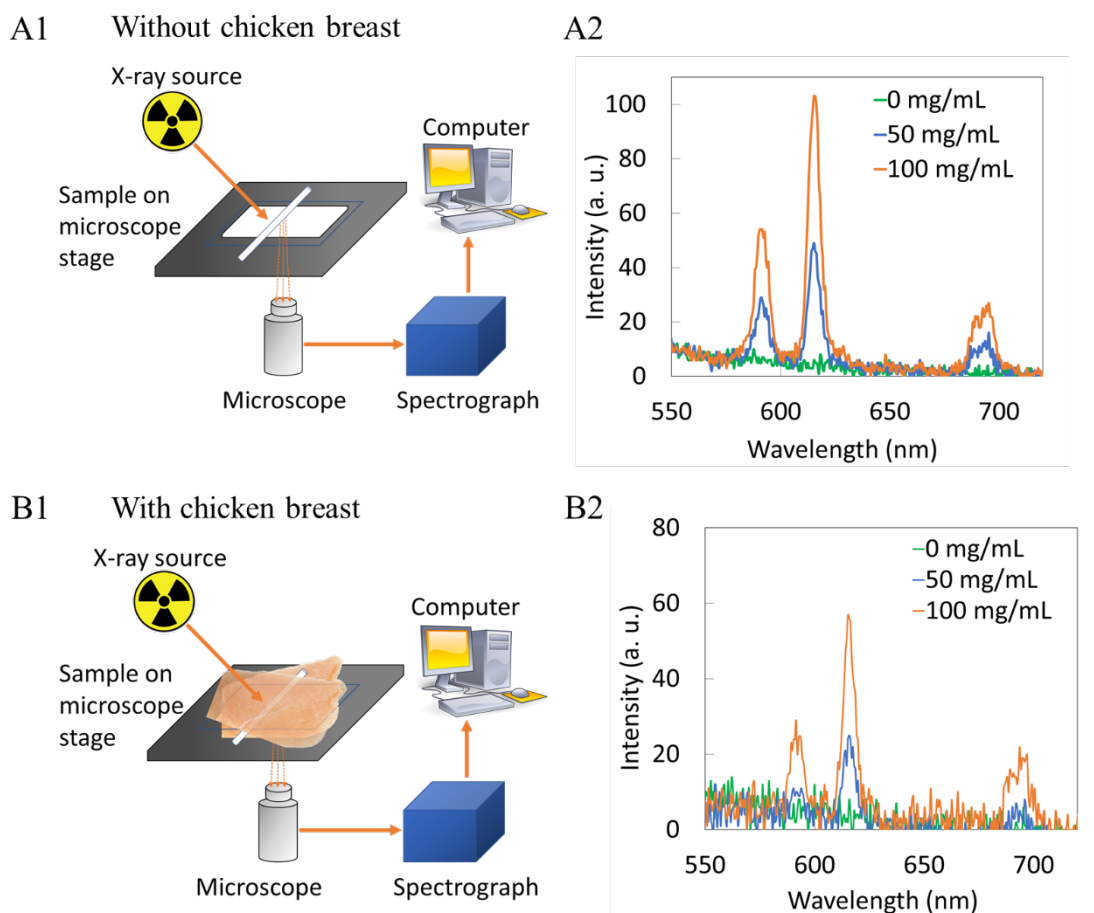
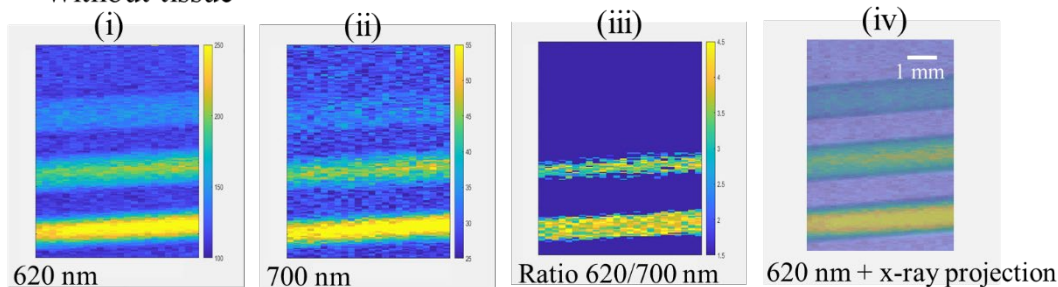


**Figure 3. 18: Schematic illustration of measuring XEOL of NaGdF<sub>4</sub>:Eu filled in capillaries (A1) without tissue (B1) sandwiched with two 5 mm porcine tissues. XEOL of NaGdF<sub>4</sub>:Eu filled in capillaries (A2) without tissue (B2) sandwiched with two 5 mm porcine tissues. Exposure time was 10 s without tissue and 60 s through tissue. Taken with permission of ref 1.**

To demonstrate focused X-ray excited light generation and collection through tissue, we loaded 1 mm diameter glass capillaries with NaGdF<sub>4</sub>:Eu nanophosphor dispersions and placed the capillaries beneath 5 mm porcine tissue for imaging (Figure 3.19). Three capillaries were used, with NaGdF<sub>4</sub> concentrations of 0, 50, and 100 mg mL<sup>-1</sup>, respectively. Our 0.75" diameter collection optics and coupled acrylic light guide collected light from a large field of view (~1"), but the focused X-ray beam irradiated

only a small region ( $\sim 250 \mu\text{m}$  spot size). We found a relatively sharp image showing luminescence only from the filled region of the capillaries and excellent agreement with the X-ray transmission image.

**A Without tissue**



**B With tissue**

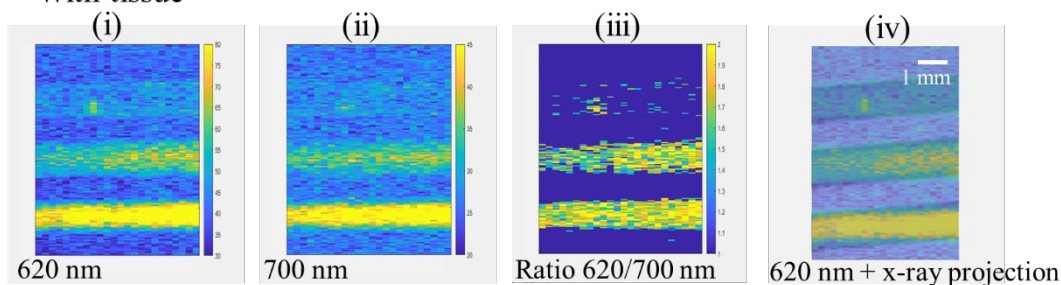


**Figure 3. 19: XELCI images of NaGdF<sub>4</sub>:Eu dispersion in capillaries (A) XELCI images without tissue (i) image of 620 nm intensity (counts) vs. position. (ii) Image of 700 nm intensity (counts) vs. position (iii) XELCI ratio image (intensity ratio of 620 nm and 700 nm). (B) XELCI images of the same capillaries sandwiched between two 5 mm porcine tissue slices (i) 620 nm image (ii) 700 nm image (iii) XELCI ratio image. (iv) Superimposed 620 nm image and X-ray transmittance images. Current was 200  $\mu\text{A}$  without tissue and 600  $\mu\text{A}$  through tissue. 1 mm scale bar is same for all images. Taken with permission of ref 1.**

The capillary with DI water ( $0 \text{ mg mL}^{-1}$ ) produced dim luminescence, as glass displays a weak X-ray luminescence signal<sup>43</sup> with a broad spectrum roughly peaking at 430 nm (Figure 3.20).

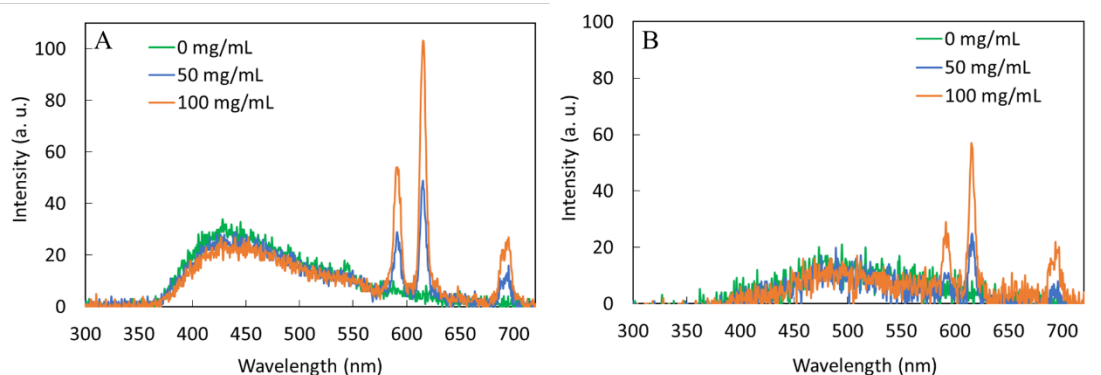


**Figure 3. 20: Full-scale XEOL of NaGdF<sub>4</sub>: Eu in capillaries A) without tissue B) sandwiched between 5 mm slices of porcine tissue. Taken with permission of ref 1.**

The signal at 50 mg mL<sup>-1</sup> and 100 mg mL<sup>-1</sup> are much larger and increase proportionally to concentration. Importantly, although the signal through tissue was 9.6 times weaker than with no tissue (mainly due to optical attenuation and partly from X-ray attenuation), the observed spatial resolution was very similar, demonstrating local radioluminescence excitation through tissue.

#### 3.4.8. MR imaging of NaGdF<sub>4</sub>:Eu and Tb

NaGdF<sub>4</sub>:Eu and Tb may also potentially be T<sub>1</sub> and T<sub>2</sub> weighted MRI contrast agents as previously reported.<sup>44,45</sup> To demonstrate this, varying concentrations of NaGdF<sub>4</sub>:Eu and Tb were prepared in DI water and imaged using a 3T Siemens MAGNATOM Prisma MRI (Figure 3.21A and B). As expected, T<sub>1</sub> weighted images became brighter, and T<sub>2</sub> weighted images became darker as [Gd] increased up to 0.4 mM. Figure 3.21C and D show longitudinal and transverse 1H relaxation rates, r<sub>1</sub> and r<sub>2</sub>, measured at 20 °C plotted against concentration of the nanoparticle

suspensions. Relaxivities were calculated by linear regression of this data. The longitudinal relaxivities for NaGdF<sub>4</sub>:Eu and NaGdF<sub>4</sub>:Tb were  $4.0 \pm 0.15$  and  $2.7 \pm 0.16$  mM<sup>-1</sup> s<sup>-1</sup>, and the transverse relaxivities were  $58 \pm 1.0$  and  $110 \pm 10$  mM<sup>-1</sup> s<sup>-1</sup>, respectively. The observed differences between Tb and Eu doped particles, especially at high concentrations, are likely from variation in sample preparation since Tb and Eu doping is at a low concentration compared to the Gd in the host crystal. The values are in the range of prior literature, and the relaxivities provide clear contrast.<sup>44</sup> The reported relaxivity values 0.27 (minimum r<sub>1</sub>) and 160 (maximum r<sub>2</sub>) mM<sup>-1</sup> s<sup>-1</sup> depends on field strength,<sup>44,46</sup> size and morphology<sup>44,46</sup> and coating.<sup>47</sup> MRI imaging would allow for deep tissue imaging and would be complementary to X-ray luminescence imaging and stimulation, allowing for non-invasive localization of nanophosphors in vivo.

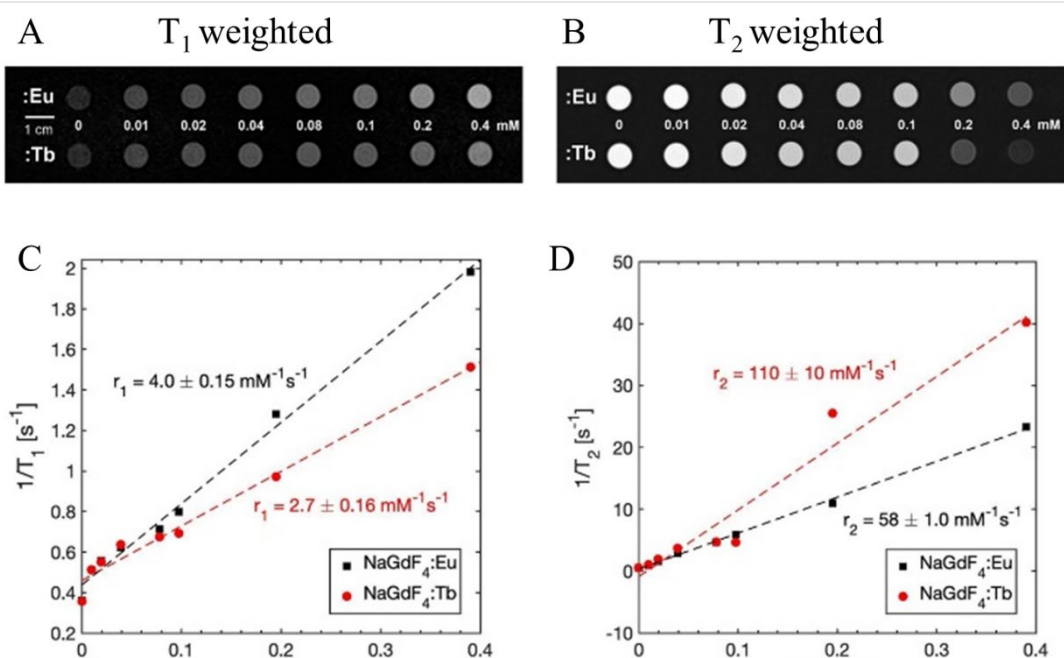


**Figure 3. 21: Magnetic resonance images (MRI) of NaGdF<sub>4</sub>:Eu and NaGdF<sub>4</sub>:Tb nanoparticle suspensions in water. (A) T1 weighted and (B) T2 weighted images with various nanoparticle concentrations. 0 mM = DI water. 1 cm scale bar is for both T1 and T2 weighted images. (C) Longitudinal relaxation rate vs. concentration for nanoparticle suspensions. (D) Transverse relaxation rate vs. concentration. Dashed lines are linear fits to data. Taken with permission of ref 1.**

### 3.5. Conclusions

We described two methods to synthesize Eu- and Tb doped NaGdF<sub>4</sub> X-ray luminescence nanophosphors. The co-precipitation method is a simple method that synthesizes spherical-shaped nanoparticles at room temperature. The hydrothermal method generated irregular particles that yielded higher X-ray excited luminescence intensity. Our investigation of annealing nanoparticles revealed that nanoparticles without a silica coating resulted in high luminescence intensity yet aggregated particles. The silica coating act as a protection layer to prevent aggregation and increase X-ray luminescence during the annealing process. However, at high temperature, it transformed NaGdF<sub>4</sub>:Eu into sodium gadolinium silicate, which also shows X-ray luminescence. Then, we functionalized NaGdF<sub>4</sub>:Eu@SiO<sub>2</sub> nanophosphors with biotin and confirmed attaching to streptavidin in vitro. Importantly, we selectively excited scintillator nanophosphors using a focused X-ray source to generate light and collect them through the tissue to generate XELCI images and XEOL was measured through tissue. We also showed that the particles could serve as MRI contrast agents. Future work will investigate the spectral shift by changing host materials for multi-analyte imaging through tissue.

### 3.6. Acknowledgments

This work was funded by NSF Track II EPSCoR OIA-1632881 for the synthesis by the NIH NIBIB R01EB026646 for the X-ray luminescence imaging and P30 GM131959 for the electron microscopy. Electron microscopy images were acquired in the Electron Microscope Facility, Clemson University, Clemson Research Park, AMRL building. MR

images were taken in the Civitan International Neuroimaging Laboratory, the University of Alabama at Birmingham. We would like to acknowledge Dr. Sriparna Bhattacharya for helping acquire some of the TEM images and Dr. Rakesh Sachdeva for helping us run the ICP-OES and TGA/DSC instruments.

### 3.7. References

- (1) Ranasinghe, M.; Arifuzzaman, M.; Rajamanthrilage, A. C.; Dickey, A.; Kolis, J. W.; Bolding, M.; Anker, J. X-Ray Excited Luminescence Spectroscopy and Imaging with NaGdF<sub>4</sub>:Eu and Tb. 2020. *RSC Adv.*, **2021**, *11*, 31717-31726. <https://doi.org/10.1039/D1RA05451A>.
- (2) Lecoq, P. Scintillation Detectors for Charged Particles and Photons. In *Detectors for Particles and Radiation. Part 1: Principles and Methods*; Fabjan, C. W., Schopper, H., Eds.; Martienssen, W., Series Ed.; Landolt-Börnstein - Group I Elementary Particles, Nuclei and Atoms; Springer Berlin Heidelberg: Berlin, Heidelberg, 2011; Vol. 21B1, pp 45–71. [https://doi.org/10.1007/978-3-642-03606-4\\_3](https://doi.org/10.1007/978-3-642-03606-4_3), Rodnyi, P. A. *Physical Processes in Inorganic Scintillators*; CRC Press, 1997.
- (3) Birowosuto, M. D.; Dorenbos, P.; van Eijk, C. W. E.; Krämer, K. W.; Güdel, H. U. High-Light-Output Scintillator for Photodiode Readout: LuI<sub>3</sub>:Ce<sup>3+</sup>. *Journal of Applied Physics* **2006**, *99* (12), 123520. <https://doi.org/10.1063/1.2207689>.
- (4) *Radiation Detectors for Medical Applications*; Tavernier, S., North Atlantic Treaty Organization, Eds.; NATO security through science series; Springer: Dordrecht, 2006.

- (5) Chen, H.; Moore, T.; Qi, B.; Colvin, D. C.; Jelen, E. K.; Hitchcock, D. A.; He, J.; Mefford, O. T.; Gore, J. C.; Alexis, F.; Anker, J. N. Monitoring PH-Triggered Drug Release from Radioluminescent Nanocapsules with X-Ray Excited Optical Luminescence. *ACS Nano* **2013**, 7 (2), 1178–1187.  
<https://doi.org/10.1021/nn304369m>.
- (6) Chen, H.; Qi, B.; Moore, T.; Colvin, D. C.; Crawford, T.; Gore, J. C.; Alexis, F.; Mefford, O. T.; Anker, J. N. Synthesis of Brightly PEGylated Luminescent Magnetic Upconversion Nanophosphors for Deep Tissue and Dual MRI Imaging. *Small* **2014**, 10 (1), 160–168. <https://doi.org/10.1002/sml.201300828>.
- (7) Development of NIR-Emitting Scintillators Based on Rare-Earth-Doped Garnet Crystals – Part 1. *Sensors and Materials* **2017**, 1407.  
<https://doi.org/10.18494/SAM.2017.1620>.
- (8) Zhou, J.; Liu, Z.; Li, F. Upconversion Nanophosphors for Small-Animal Imaging. *Chem. Soc. Rev.* **2012**, 41 (3), 1323–1349. <https://doi.org/10.1039/C1CS15187H>.
- (9) Pratz, G.; Carpenter, C. M.; Sun, C.; Xing, L. X-Ray Luminescence Computed Tomography via Selective Excitation: A Feasibility Study. *IEEE Transactions on Medical Imaging* **2010**, 29 (12), 1992–1999.  
<https://doi.org/10.1109/TMI.2010.2055883>.
- (10) Chen, H.; Wang, F.; Moore, T. L.; Qi, B.; Sulejmanovic, D.; Hwu, S.-J.; Mefford, O. T.; Alexis, F.; Anker, J. N. Bright X-Ray and up-Conversion Nanophosphors Annealed Using Encapsulated Sintering Agents for Bioimaging Applications. *J. Mater. Chem. B* **2017**, 5 (27), 5412–5424. <https://doi.org/10.1039/C7TB01289F>.



- (11) Lun, M. C.; Cong, W.; Arifuzzaman, M.; Ranasinghe, M.; Bhattacharya, S.; Anker, J.; Wang, G.; Li, C. X-Ray Luminescence Imaging for Small Animals. In *Optics and Ionizing Radiation*; International Society for Optics and Photonics, 2020; Vol. 11224, p 112240F. <https://doi.org/10.1117/12.2544601>.
- (12) Wang, F.; Banerjee, D.; Liu, Y.; Chen, X.; Liu, X. Upconversion Nanoparticles in Biological Labeling, Imaging, and Therapy. *Analyst* **2010**, *135* (8), 1839–1854. <https://doi.org/10.1039/C0AN00144A>.
- (13) Berry, R.; Getzin, M.; Gjestebj, L.; Wang, G. X-Optogenetics and U-Optogenetics: Feasibility and Possibilities. *Photonics* **2015**, *2* (1), 23–39. <https://doi.org/10.3390/photonics2010023>.
- (14) Sudheendra, L.; Das, G. K.; Li, C.; Stark, D.; Cena, J.; Cherry, S. R.; Kennedy, I. M. NaGdF<sub>4</sub>: Eu<sup>3+</sup> Nanoparticles for Enhanced X-Ray Excited Optical Imaging. *Chem. Mater.* **2014**, *26* (5), 1881–1888. <https://doi.org/10.1021/cm404044n>.
- (15) F, H.; P, Y.; D, W.; N, N.; S, G.; X, L. Self-Assembled  $\beta$ -NaGdF<sub>4</sub> Microcrystals: Hydrothermal Synthesis, Morphology Evolution, and Luminescence Properties. *Inorg Chem* **2011**, *50* (9), 4116–4124. <https://doi.org/10.1021/ic200155q>.
- (16) Ren, Y.; Winter, H.; Rosch, J. G.; Jung, K.; Duross, A. N.; Landry, M. R.; Pratz, G.; Sun, C. PEGylated  $\beta$ -NaGdF<sub>4</sub>/Tb@CaF<sub>2</sub> Core/Shell Nanophosphors for Enhanced Radioluminescence and Folate Receptor Targeting. *ACS Appl. Nano Mater.* **2019**, *2* (6), 3718–3727. <https://doi.org/10.1021/acsanm.9b00629>.
- (17) Yanagida, T. Study of Rare-Earth-Doped Scintillators. *Optical Materials* **2013**, *35* (11), 1987–1992. <https://doi.org/10.1016/j.optmat.2012.11.002>.

- (18) Guan, H.; Liu, G.; Wang, J.; Dong, X.; Yu, W. Multicolor Tunable Luminescence and Paramagnetic Properties of NaGdF<sub>4</sub>:Tb<sup>3+</sup>/Sm<sup>3+</sup> Multifunctional Nanomaterials. *Dalton Trans.* **2014**, 43 (28), 10801–10808.  
<https://doi.org/10.1039/C4DT00158C>.
- (19) Mitragotri, S.; Lahann, J. Physical Approaches to Biomaterial Design. *Nature Mater* **2009**, 8 (1), 15–23. <https://doi.org/10.1038/nmat2344>.
- (20) Stendahl, J. C.; Sinusas, A. J. Nanoparticles for Cardiovascular Imaging and Therapeutic Delivery, Part 1: Compositions and Features. *Journal of Nuclear Medicine* **2015**, 56 (10), 1469–1475. <https://doi.org/10.2967/jnumed.115.160994>.
- (21) Liu, D.; Mori, A.; Huang, L. Role of Liposome Size and RES Blockade in Controlling Biodistribution and Tumor Uptake of GM1-Containing Liposomes. *Biochimica et Biophysica Acta (BBA) - Biomembranes* **1992**, 1104 (1), 95–101.  
[https://doi.org/10.1016/0005-2736\(92\)90136-A](https://doi.org/10.1016/0005-2736(92)90136-A).
- (22) Rejman, J.; Oberle, V.; Zuhorn, I. S.; Hoekstra, D. Size-Dependent Internalization of Particles via the Pathways of Clathrin- and Caveolae-Mediated Endocytosis. *Biochem J* **2004**, 377 (Pt 1), 159–169. <https://doi.org/10.1042/BJ20031253>.
- (23) Li, Y.; Li, Y.; Wang, R.; Xu, Y.; Zheng, W. Enhancing Upconversion Luminescence by Annealing Processes and the High-Temperature Sensing of ZnO:Yb/Tm Nanoparticles. *New J. Chem.* **2017**, 41 (15), 7116–7122.  
<https://doi.org/10.1039/C7NJ01358B>.
- (24) Sagaydachnaya, E. A.; Kochubey, V. I.; Konyukhova, J. G. Influence of Annealing Temperature on the Upconversion Luminescence Properties of NaYF<sub>4</sub>:Er,Yb@SiO

2 Particles. *J. Phys.: Conf. Ser.* **2017**, *917*, 032006. <https://doi.org/10.1088/1742-6596/917/3/032006>.

- (25) Avci, P.; Gupta, A.; Sadasivam, M.; Vecchio, D.; Pam, Z.; Pam, N.; Hamblin, M. R. Low-Level Laser (Light) Therapy (LLLT) in Skin: Stimulating, Healing, Restoring. *Semin Cutan Med Surg* **2013**, *32* (1), 41–52.
- (26) Ash, C.; Dubec, M.; Donne, K.; Bashford, T. Effect of Wavelength and Beam Width on Penetration in Light-Tissue Interaction Using Computational Methods. *Lasers Med Sci* **2017**, *32* (8), 1909–1918. <https://doi.org/10.1007/s10103-017-2317-4>.
- (27) Li, J.; Hao, Z.; Zhang, X.; Luo, Y.; Zhao, J.; Lü, S.; Cao, J.; Zhang, J. Hydrothermal Synthesis and Upconversion Luminescence Properties of  $\beta$ -NaGdF<sub>4</sub>:Yb<sup>3+</sup>/Tm<sup>3+</sup> and  $\beta$ -NaGdF<sub>4</sub>:Yb<sup>3+</sup>/Ho<sup>3+</sup> Submicron Crystals with Regular Morphologies. *J Colloid Interface Sci* **2013**, *392*, 206–212. <https://doi.org/10.1016/j.jcis.2012.09.076>.
- (28) Chen, H.; Qi, B.; Moore, T.; Wang, F.; Colvin, D. C.; Sanjeeva, L. D.; Gore, J. C.; Hwu, S.-J.; Mefford, O. T.; Alexis, F.; Anker, J. N. Multifunctional Yolk-in-Shell Nanoparticles for PH-Triggered Drug Release and Imaging. *Small* **2014**, *10* (16), 3364–3370. <https://doi.org/10.1002/smll.201303769>.
- (29) Chen, H.; Sulejmanovic, D.; Moore, T.; Colvin, D. C.; Qi, B.; Mefford, O. T.; Gore, J. C.; Alexis, F.; Hwu, S.-J.; Anker, J. N. Iron-Loaded Magnetic Nanocapsules for PH-Triggered Drug Release and MRI Imaging. *Chem Mater* **2014**, *26* (6), 2105–2112. <https://doi.org/10.1021/cm404168a>.

- (30) Gai, S.; Yang, P.; Li, C.; Wang, W.; Dai, Y.; Niu, N.; Lin, J. Synthesis of Magnetic, Up-Conversion Luminescent, and Mesoporous Core–Shell-Structured Nanocomposites as Drug Carriers. *Advanced Functional Materials* **2010**, *20* (7), 1166–1172. <https://doi.org/10.1002/adfm.200902274>.
- (31) Liu, Y.; Tu, D.; Zhu, H.; Ma, E.; Chen, X. Lanthanide-Doped Luminescent Nano-Bioprobes: From Fundamentals to Biodetection. *Nanoscale* **2013**, *5* (4), 1369–1384. <https://doi.org/10.1039/C2NR33239F>.
- (32) Asakura, R.; Isobe, T.; Kurokawa, K.; Aizawa, H.; Ohkubo, M. Tagging of Avidin Immobilized Beads with Biotinylated YAG:Ce<sup>3+</sup> Nanocrystal Phosphor. *Anal Bioanal Chem* **2006**, *386* (6), 1641–1647. <https://doi.org/10.1007/s00216-006-0814-6>.
- (33) Barral, J. K.; Gudmundson, E.; Stikov, N.; Etezadi-Amoli, M.; Stoica, P.; Nishimura, D. G. A Robust Methodology for in Vivo T1 Mapping. *Magnetic Resonance in Medicine* **2010**, *64* (4), 1057–1067. <https://doi.org/10.1002/mrm.22497>.
- (34) Karakuzu, A.; Boudreau, M.; Duval, T.; Boshkovski, T.; Leppert, I. R.; Cabana, J.-F.; Gagnon, I.; Beliveau, P.; Pike, G. B.; Cohen-Adad, J.; Stikov, N. QMRLab: Quantitative MRI Analysis, under One Umbrella. *Journal of Open Source Software* **2020**, *5* (53), 2343. <https://doi.org/10.21105/joss.02343>.
- (35) Sedlmeier, A.; Gorris, H. H. Surface Modification and Characterization of Photon-Upconverting Nanoparticles for Bioanalytical Applications. *Chem. Soc. Rev.* **2015**, *44* (6), 1526–1560. <https://doi.org/10.1039/C4CS00186A>.

- (36) Bhagavannarayana, G.; Kushwaha, S. K.; Parthiban, S.; Meenakshisundaram, S. The Influence of Mn-Doping on the Nonlinear Optical Properties and Crystalline Perfection of Tris(Thiourea)Zinc(II) Sulphate Crystals: Concentration Effects. *Journal of Crystal Growth* **2009**, *311* (3), 960–965.  
<https://doi.org/10.1016/j.jcrysgro.2008.09.116>.
- (37) Li, X.; Xue, Z.; Jiang, M.; Li, Y.; Zeng, S.; Liu, H. Soft X-Ray Activated NaYF<sub>4</sub>:Gd/Tb Scintillating Nanorods for in Vivo Dual-Modal X-Ray/X-Ray-Induced Optical Bioimaging. *Nanoscale* **2017**, *10* (1), 342–350.  
<https://doi.org/10.1039/C7NR02926H>.
- (38) Zhang, W.; Shen, Y.; Liu, M.; Gao, P.; Pu, H.; Fan, L.; Jiang, R.; Liu, Z.; Shi, F.; Lu, H. Sub-10 Nm Water-Dispersible  $\beta$ -NaGdF<sub>4</sub>:  $X\%$  Eu<sup>3+</sup> Nanoparticles with Enhanced Biocompatibility for in Vivo X-Ray Luminescence Computed Tomography. *ACS Appl. Mater. Interfaces* **2017**, *9* (46), 39985–39993.  
<https://doi.org/10.1021/acsami.7b11295>.
- (39) Fu, Z.; Liu, B. Solution Combustion Synthesis, Photoluminescence and X-Ray Luminescence of Eu<sup>3+</sup>-Doped LaAlO<sub>3</sub> Nanophosphors. *Ceramics International* **2016**, *42* (2, Part A), 2357–2363. <https://doi.org/10.1016/j.ceramint.2015.10.032>.
- (40) Wang, M.; Abbineni, G.; Clevenger, A.; Mao, C.; Xu, S. Upconversion Nanoparticles: Synthesis, Surface Modification and Biological Applications. *Nanomedicine: Nanotechnology, Biology and Medicine* **2011**, *7* (6), 710–729.  
<https://doi.org/10.1016/j.nano.2011.02.013>.

- (41) Bouzigues, C.; Gacoin, T.; Alexandrou, A. Biological Applications of Rare-Earth Based Nanoparticles. *ACS Nano* **2011**, *5* (11), 8488–8505.  
<https://doi.org/10.1021/nn202378b>.
- (42) Matthews, T. E.; Medina, M.; Maher, J. R.; Levinson, H.; Brown, W. J.; Wax, A. Deep Tissue Imaging Using Spectroscopic Analysis of Multiply Scattered Light. *Optica* **2014**, *1* (2), 105. <https://doi.org/10.1364/OPTICA.1.000105>.
- (43) Alonso, P. J.; Halliburton, L. E.; Kohnke, E. E.; Bossoli, R. B. X-ray-induced Luminescence in Crystalline SiO<sub>2</sub>. *Journal of Applied Physics* **1983**, *54* (9), 5369–5375. <https://doi.org/10.1063/1.332715>.
- (44) Lu, Z. Size-Tunable NaGdF<sub>4</sub> Nanoparticles as T<sub>2</sub> Contrast Agents for High-Field Magnetic Resonance Imaging. *RSC Advances* **2017**, *7*.
- (45) Lu, W.; Liao, Y.; Jiang, C.; Wang, R.; Shan, X.; Chen, Q.; Sun, G.; Liu, J. Polydopamine-Coated NaGdF<sub>4</sub>:Dy for  $T_1 / T_2$  -Weighted MRI/CT Multimodal Imaging-Guided Photothermal Therapy. *New J. Chem.* **2019**, *43* (19), 7371–7378.  
<https://doi.org/10.1039/C9NJ00561G>.
- (46) Wang, M.; Zhang, Y.; Yao, Q.; Ng, M.; Lin, M.; Li, X.; Bhakoo, K. K.; Chang, A. Y.; Rosei, F.; Vetrone, F. Morphology Control of Lanthanide Doped NaGdF<sub>4</sub> Nanocrystals via One-Step Thermolysis. *Chem. Mater.* **2019**, *31* (14), 5160–5171.  
<https://doi.org/10.1021/acs.chemmater.9b01155>.
- (47) Okubo, K.; Takeda, R.; Murayama, S.; Umezawa, M.; Kamimura, M.; Osada, K.; Aoki, I.; Soga, K. Size-Controlled Bimodal *in Vivo* Nanoprobes as near-Infrared Phosphors and Positive Contrast Agents for Magnetic Resonance Imaging. *Science*

*and Technology of Advanced Materials* **2021**, 22 (1), 160–172.

<https://doi.org/10.1080/14686996.2021.1887712>.

## CHAPTER FOUR

### FUNCTIONALIZING RADIODENSE PARTICLES AND DEVELOPING IMMUNOASSAYS TO DETECT SARS-CoV-2 ANTIBODIES

#### 4.1. Abstract

As discussed in chapters one, two, and three, plasmonic and X-ray luminescence nanoparticles have interesting optical properties depending on their size, shape, crystal structure, etc. Another important property of these nanoparticles is their surface area which can be functionalized with biomolecules and target specific biomolecules and components to detect and quantify them. Therefore, these nanoparticles are used in developing biosensors/ immunosensors. In this chapter, plasmonic and X-ray luminescence nanoparticles were used to develop two immunoassays (a lateral flow assay and an implantable immunoassay).

Lateral flow assays are the most common point-of-care device available to confirm the presence or absence of an analyte. Many LFAs are available to detect COVID -19 antibodies (human anti-spike IgG and IgM) in human blood or serum. However, there is no available LFA to detect COVID- 19 antibodies (human anti-spike IgG and IgA) in human saliva. Therefore, we are developing a lateral flow assay (LFA) to detect SARS-CoV-2 antibodies in human saliva. Our preliminary studies show the proof of concept of the designed LFA. Further, we have demonstrated the proof of concept of an immunoassay using RBD functionalized AuNPs, and anti-spike IgG functionalized x-ray luminescence microparticles (Gadolinium oxysulfide). When AuNPs are attached to Gadolinium oxysulfide microparticles, the x-ray luminescence is



decreased. This approach can be used to develop an implantable immune assay that can quantify biomarkers *in vivo* locally and continuously.

## 4.2. Introduction

This chapter describes the development of two immunosensors that use light scattering and absorption properties of gold nanoparticles and X-ray excited optical luminescence of X-ray scintillators. As discussed in chapter one, the surface of a nanoparticle can be functionalized with biomolecules such as proteins (antibodies, antigens, enzymes, etc.) and nucleotides (single-strand DNA, RNA) for *in vivo* imaging and diagnostics<sup>1</sup>. By functionalizing nanoparticles with antibodies, it can target and specifically binds to antigens. The optical properties of the functionalized particles are used to detect and quantify the specific antigens. The size of gold nanoparticles and X-ray luminescence microparticles we used in this section is ~20 nm and 2.5  $\mu\text{m}$ , respectively. The typical length of an antibody is 10 nm.<sup>2</sup> The biomolecule functionalized gold nanoparticles, and X-ray luminescence microparticles are used to detect SARS-CoV-2 antibodies.

Coronavirus disease 2019 (COVID-19) is the current outbreak of coronavirus caused by the SARS-CoV-2 virus, and it is still playing a vital role around the world. By January 2022, more than 300 million confirmed cases, 5 million related deaths<sup>1a</sup>, and 12 virus variants<sup>1b</sup> have been reported worldwide. There are several FDA-approved vaccines<sup>1c</sup> and public health strategies (social distancing and wearing masks) to slow down and control the pandemic. However, reopening businesses and easing restrictions

on human mobility and interactions will depend on accurate estimates of population-level infection and markers of immunity<sup>4,5</sup>.

RT-qPCR and the rapid antigen test (RAT) are the most common diagnostic tests for COVID-19. However, both these tests can diagnose current infections only. It cannot diagnose most recent or previous COVID-19 infections. Therefore, to identify past infection, confirm vaccine trials are working, and make sure a specific community is at herd-immunity level, SARS-CoV-2 antibody detection assays are required.

Enzyme-linked immunosorbent assay (ELISA) and Lateral flow assay (LFA) are the common immunoassays available for detecting SARS-CoV-2 antibodies. ELISA is a laboratory-based quantitative method that is expensive and time-consuming. On the other hand, LFAs are point-of-care assays and produce qualitative results in minutes. In April 2020, Food and Drug Administration (FDA) approved the 1<sup>st</sup> serological LFA (<https://www.fda.gov/media/136625/download>). So far, there are several EUA authorized LFAs available in the market to test antibodies in blood and serum<sup>6</sup>. However, there are limitations associated with current LFAs. Most of these test kits give high specificity and sensitivity in clinical trials. Still, real-world performance is uncertain, giving false-positive results due to cross-neutralization between SARS-CoV and SARS-CoV-2<sup>7</sup>, less accurate in early stages of infection and IgM and IgG combined assay shows better performance.

This chapter will discuss developing an LFA to detect SARS-CoV-2 antibodies (IgG and IgA) in human saliva and an implantable immunoassay to detect SARS-CoV-2 antibodies (IgG) in blood/serum. Even though many LFAs detect COVID-19 antibodies

in blood and serum, there are no available LFAs to detect antibodies in saliva. The previous COVID-19 antibody tests (IgG and IgA) done using ELISA have shown 84.0% sensitivity and 90.6% specificity with whole saliva samples collected from the general symptomatic population. Sensitivity was improved by pelleting mucus and treating saliva with TBS-Tween and 5% BSA. However, it comes at a cost to the specificity<sup>8</sup>. The optimum data were collected by removing mucus, concentrating the samples, and blocking non-specific binding, giving 84.2% sensitivity and 100% specificity. These values can go up to 100% sensitivity and specificity in serum.

Here we describe the implantable immunoassay to detect SARS-CoV-2 antibodies (IgG). However, this is only a proof of concept to show that x-ray luminescence nanoparticles can be used to develop implantable immunoassays that can measure biomarkers in deep tissues, synovial fluid, and cerebrospinal fluid locally and continuously in the future.

### 4.3. Methods

#### 4.3.1. *Designing and developing an LFA to detect SARS-CoV-2 antibodies (Proof of concept)*

Universal lateral flow assay kits (ab270537) were purchased from Abcam, USA. The assay kit protocol was used to develop the proof-of-concept sandwich lateral flow immunoassays to detect SARS-CoV-2 antibodies with slight modifications<sup>9</sup>.

**$\alpha$ -human IgG and IgA antibody conjugated ulfa-tag.**  $\alpha$ -human IgG and IgA (1mg/mL, 10  $\mu$ L) were separately mixed with the modifier reagent (1  $\mu$ L) given in the

test kit. The above mixtures were added to given ulfa-tag vials and resuspended gently by pipetting. The two vials were kept at room temperature overnight. LL-quencher (1  $\mu$ L) was added to the ulfa-tag vials and held 30 minutes before use.

**Spike proteins (RBD and trimeric) functionalized AuNPs.** RBD and spike proteins (1 mg/mL) were diluted to 0.1 mg/mL using provided gold-antibody-diluent. Spike proteins (12  $\mu$ L) were added to the reaction buffer (42  $\mu$ L) and 45  $\mu$ L of this mixture was added to vials containing freeze-dried AuNPs (40 nm). The reaction was kept 15 minutes at room temperature before adding the gold quencher (5  $\mu$ L). Then, spike proteins conjugated AuNPs were washed with 10 times diluted gold-antibody-diluent and stored in the same solution containing 0.5% BSA. The final solutions contain spike proteins conjugated AuNPs (OD=20, 50  $\mu$ L).

**LFA test procedure.** Universal running buffer (10x) was diluted to 1x using DI water, and the final buffer solution contains 0.1% BSA. Ulfa-Tag conjugated  $\alpha$ -human IgG and Ulfa-Tag conjugated  $\alpha$ -human IgA were diluted (1x) to prepare 50 mg/mL solutions, and gold-spike protein conjugates were diluted to obtain 6 OD using the universal running buffer.

Gold-biotin (40 nm, OD= 10) was diluted to 1 OD using universal running buffer to use in the control line. The analyte (human anti-spike IgG) was diluted to prepare 10 and 100 ng/mL solutions using universal running buffer. Each test was duplicated, and for a single strip, diluted capture Ulfa-tag-conjugated  $\alpha$ -human IgG or IgA (5  $\mu$ L), gold spike protein conjugate (5  $\mu$ L), gold-biotin conjugate (5  $\mu$ L) and human anti-spike IgG (75  $\mu$ L) were added to each well of low protein binding 96-well plate and incubated at

room temperature for 30 minutes. Test stripes were added and read after 20 minutes. Negative control was run without analyte (human anti-spike IgG), just adding running buffer (75  $\mu$ L).

#### *4.3.2. Functionalizing gold NPs with SARS-CoV-2 receptor-binding domain (RBD) protein*

Gold nanoparticles (AuNPs, 20 nm spheres) were purchased from CytoDiagnostics Inc, Canada. The AuNPs were first coated with polyethylene glycol (PEG) and then functionalized with RBD protein using EDC/ Sulfo-NHS coupling.

**PEG-coated AuNPs.** Thiol-PEG-carboxylic (SH-PEG<sub>5k</sub>-COOH, 60 mg/mL, 1 mL) and thiol-methyl PEG (SH-mPEG<sub>5k</sub>, 60 mg/mL, 100  $\mu$ L) were prepared in 50% ETOH and transferred to a round bottom flask which contains 50 mL of DI water. The mixture was stirred for 15 minutes before adding AuNPs (10 OD, 500  $\mu$ L). After adding AuNPs, the reaction mixture was continued to stir for another 15 minutes before keeping at 4 °C overnight. Then, the PEG-coated AuNPs (Au@PEG) were washed three times and collected by centrifuging at 5000g (RCF) for ½ hour. Au@PEG were dispersed in DI water (10 mL) and kept at 4 °C.

**SARS-CoV-2 RBD protein functionalized AuNPs.** Au@PEG (four portions of 1 mL) was centrifuged and collected. Au@PEG were redispersed in three different buffers at 5.0 mM, 5.0 pH (HEPES, MOPS, and MES), and DI water ( $p^H \sim 6.5$ ). Then EDC ((1-ethyl-3-(3-dimethylaminopropyl) carbodiimide hydrochloride), 1 mg/mL, 25  $\mu$ L) and Sulfo-NHS (N-hydroxysulfosuccinimide, 1 mg/mL, 40  $\mu$ L) were added and it was reacted for 40 minutes. Nanoparticles were washed and collected by centrifuging,

and RBD protein (50  $\mu\text{g/mL}$ ) in 1.0 mL HEPES buffer (10 mM, pH= 7.4) were added to the EDC/Sulfo-NHS treated Au@PEG nanoparticles. It was reacted for 2 hours at room temperature before keeping at 4  $^{\circ}\text{C}$  overnight. The RBD protein functionalized AuNPs (Au@PEG:RBD) were collected by centrifuging at 5000g for  $\frac{1}{2}$  hour. Then, Au@PEG:RBD were redispersed in 10.0 mM, 7.4 pH HEPES containing 1.0 mM ethanolamine and 0.1% BSA and kept at room temperature 5 minutes. Finally, Au@PEG:RBD were washed, collected and redispersed in 10.0 mM HEPES containing 0.1% BSA.

Uv-vis extinction spectra of AuNPs, Au@PEG, and Au@PEG:RBD were collected using a Uv-vis spectrophotometer (Shimadzu corp., Uv 3600 plus, Uv-Vis-NIR spectrophotometer).

#### *4.3.3. Functionalizing Eu doped gadolinium oxysulfide ( $\text{Gd}_2\text{O}_2\text{S:Eu}$ / GOS:Eu, 2.5 $\mu\text{m}$ ) microparticles with human anti-spike IgG antibodies*

**PEG-coated GOS:Eu microparticles.** Silane-PEG-carboxylic ( $\text{SiO}_2\text{-PEG}_{5\text{k}}\text{-COOH}$ , 60 mg/mL, 1 mL) and Silane-methyl PEG ( $\text{SiO}_2\text{-mPEG}_{5\text{k}}$ , 60 mg/mL, 100  $\mu\text{L}$ ) were prepared in 90% ETOH and transferred to a Teflon tube which contains 10.0 mL of 90 %ETOH. The mixture was mixed using a rotator for 15 minutes before adding GOS:Eu microparticles (20 mg) dispersed in 1 mL 90% ETOH. After adding GOS:Eu microparticles, the reaction mixture continued to rotate for another 30 minutes before keeping at 4  $^{\circ}\text{C}$  overnight. Then, the PEG-coated AuNPs (GOS:Eu@PEG) were washed three times and collected by centrifuging at 500g (RCF) for 5 minutes. GOS:Eu@PEG were dispersed in DI water (2 mL) and kept at 4  $^{\circ}\text{C}$ .

**Human anti-spike IgG antibodies functionalized AuNPs.** GOS:Eu@PEG (1 mL) was centrifuged and collected. GOS:Eu@PEG were redispersed in HEPES buffers (5.0 mM, 5.0 pH). Then EDC (100  $\mu$ L, 1 mg/mL) and Sulfo-NHS (150  $\mu$ L, 1 mg/mL) were added, and it was reacted for 40 minutes. Microparticles were washed and collected by centrifuging, and Human anti-spike IgG antibodies (75  $\mu$ g/mL) in 1 mL HEPES buffer (10 mM, pH= 7.4) were added to the EDC/Sulfo-NHS treated GOS:Eu@PEG nanoparticles. It was reacted for 2 hours at room temperature before keeping at 4 °C overnight. The Human anti-spike IgG antibodies functionalized GOS:Eu microparticles (GOS:Eu@PEG:IgG) were collected by centrifuging at 500g for 5 minutes. Then, GOS:Eu@PEG:IgG were redispersed in 10.0 mM, 7.4 pH HEPES containing 1.0 mM ethanolamine and 0.1% BSA and kept at room temperature 5 minutes. Finally, GOS:Eu@PEG:IgG were washed, collected and redispersed in 10 mM HEPES containing 0.1% BSA.

To attach AuNPs onto GOS:Eu microparticles, 200  $\mu$ L of Au@PEG:RBD in HEPES were added to GOS:Eu@PEG:IgG in HEPES (200  $\mu$ L), and the mixture was inverted a couple of times to mix. Photographic images were taken under UV light (395 nm). Transmission electron microscope images were taken from Hitachi HT7800 operating at 20–120 keV and 8  $\mu$ A. PEG coated AuNPs and GOS:Eu@PEG:IgG were mixed to obtain negative control.

#### *4.3.4. ray excited optical luminescence (XEOL) spectroscopy*

X-ray luminescence of control and sample were measured by irradiating with an X-ray beam. 200  $\mu$ L of both samples were placed on the stage of an inverted microscope

and irradiated with an X-ray beam generated using a Mini-X (Ag) X-ray source (Amptek, Bedford, MA) set at 40 kV and 99  $\mu$ A. The emission of nanoparticles was collected by 5x objective and focused on a spectrograph (DNS 300, DeltaNu, Laramie, WY, USA), equipped with a cooled CCD camera (iDUS-420BV, Andor, South Windsor, CT, United States) with 30 s exposure time.

#### **4.4. Results and Discussion**

##### *4.4.1. Designing and developing an LFA to detect SARS-CoV-2 antibodies (Proof of concept)*

The LFA to detect SARS-CoV-2 antibodies in human saliva was designed by considering the current availability and needs in the market. The currently available LFAs to detect SARS-CoV-2 antibodies use serum or blood, and draining blood is painful for the patient, and separating serum from blood is required. Therefore, using saliva is simple and easy. IgA is mainly found in mucus, and the IgG amount in saliva/mucus is correlated with the serum IgG in serum<sup>10</sup>. Furthermore, the previous studies using ELISA show the ability to use IgG, IgA, and IgM to detect SARS-CoV-2 antibodies in serum<sup>11</sup> and saliva<sup>8,12</sup>. By considering these factors, the designed LFA is illustrated in figure 4.1.



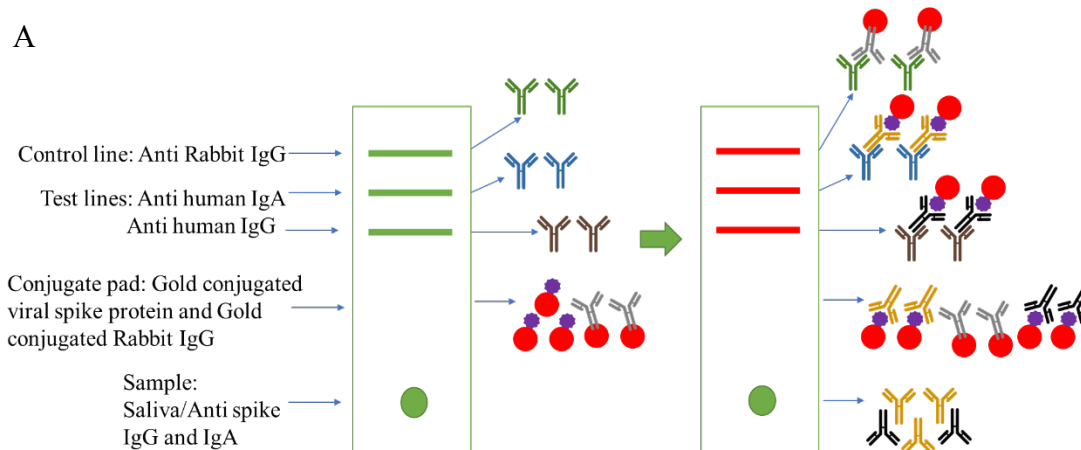


**Figure 4. 1: Design of new lateral flow assay to test anti-spike IgG and IgA in human saliva.**

After designing the LFA, proof of concept experiments was carried out using a universal LFA kit. Figures 4.2A and B show the experimental steps and results. 1<sup>st</sup> RBD or trimeric conjugated AuNPs and anti-human IgG or IgA conjugated Ulfa tags were prepared. Next, they were mixed with human anti-spike IgG antibodies to form an antibody-antigen complex. Then, the test strip was dipped in the solution, which contains the above complex and biotin-conjugated AuNPs. Ulfa tag binds with the anti-ulfa tag on the test line, and if the Ulfa tag contains the antibody-antigen complex, the test line shows up in red color. The control line has streptavidin biotinylated AuNPs bound to it and shows red color. According to the results, both RBD and trimeric showed positive results for anti-spike IgG. However, we could not test for anti-spike IgA instead of anti-spike IgG on IgA conjugated Ulfa tag. The result was negative and confirmed there's no cross-reaction between the anti-spike IgA and anti-human IgG.

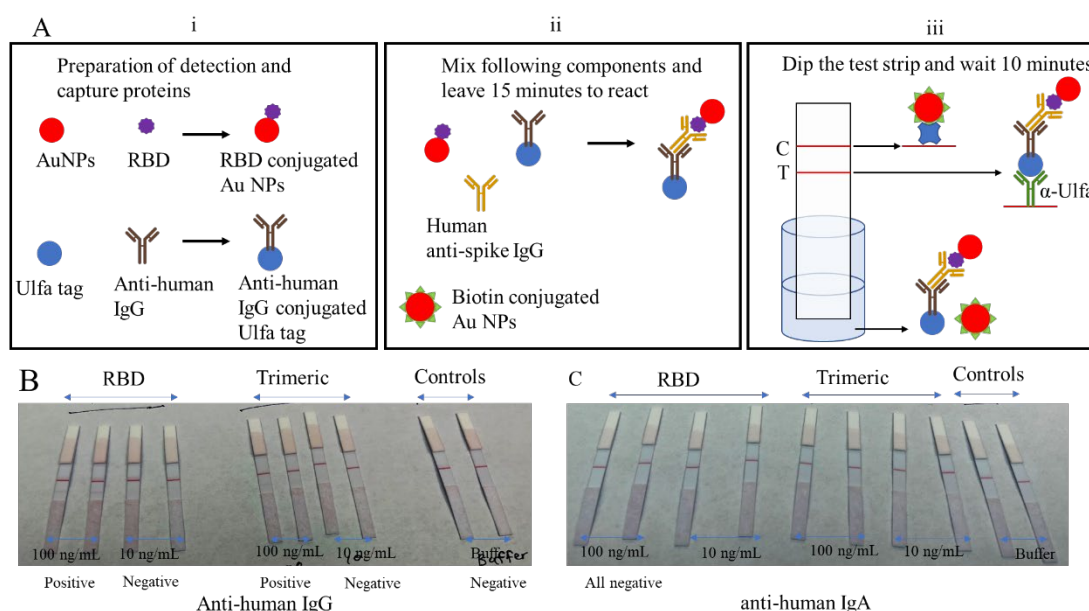


**Figure 4. 2: Schematic illustration of (i) preparing RBD conjugated AuNPs and anti-human IgG conjugated Ulfa tag, (ii) combining RBD conjugated AuNPs, human IgG conjugated Ulfa tag, and biotin-conjugated AuNPs, (iii) dipping the LFA test strip. Images of LFA test strips after running (B) human anti-spike IgG and (C) human anti-spike IgA.**

AuNPs were coated with PEG (SH-PEG<sub>5k</sub>-COOH and SH-mPEG<sub>5k</sub>) using previously described methods with slight modifications<sup>13,14</sup>. According to Ron *et al.*, thiol may react with the oxidative gold surface via an oxidation-reduction reaction. AuNPs surface is reduced, and thiol adsorbs onto Au surface followed by chemisorption, which includes breaking the S-H bond and forming Au-S bond. Breaking of S-H bond is favorable in slightly basic media; however, to the best of our knowledge, the effect of pH is not yet well studied<sup>15</sup>. Then the RBD proteins were covalently bound to the carboxylic acid group using EDC/Sulfo-NHS coupling. The optimum reaction condition for most EDC/Sulfo-NHS reactions is acidic (pH ~4.5-6.0)<sup>16,17</sup>. However, some protocols are optimized to work in neutral and slightly basic media (pH ~4.5-7.2)<sup>18,19</sup>. In this experiment, 5.0 pH was selected considering pK<sub>a</sub> of most carboxylic acid groups (~4-5

e.g.,  $pK_a$  value of acetic acid = 4.74 and butanoic acid = 4.82<sup>20</sup>), the stability of Au@PEG in the medium. After EDC/Sulfo-NHS coupling, AuNPs were washed, and the pH value was brought to 7.4 by adding HEPES (10 mM). As the isoelectric point of RBD ( $pI$  = 7.36–9.85, spike protein  $pI$  = 5.9, 6.24)<sup>21</sup> and human anti-spike IgG ( $pI$  = 6.6–7.2)<sup>22,23</sup> are around at neutral  $pH$ , the bioconjugation was done at 7.4. However, the  $pI$  of SARS-CoV-2 proteins was estimated using computational methods, and the actual values may be lower than the calculated values<sup>24</sup>.

#### *4.4.2. Functionalizing gold NPs with SARS-CoV-2 receptor-binding domain (RBD) protein*

Using UV-Vis spectroscopy, the PEGylation of AuNPs and protein binding to carboxylic acid were monitored (Figure 4.3). The wavelength that gives the maximum extinction ( $\lambda_{max}$ ) of AuNPs is 520 nm, and upon addition of PEG coating  $\lambda_{max}$  value is shifted to the red side and shows up at 523 nm. This value is consistent with the previous studies done with 10–50 nm AuNPs coated with PEG (5 and 6 kDa)<sup>25,26</sup>. When protein is attached to the carboxylic acid group  $\lambda_{max}$  value further shifts to red (526 nm), showing an increase in size. Absorption peaks of peptide bonds and free proteins were observed at 210 and 280 nm, respectively<sup>27,28</sup>.

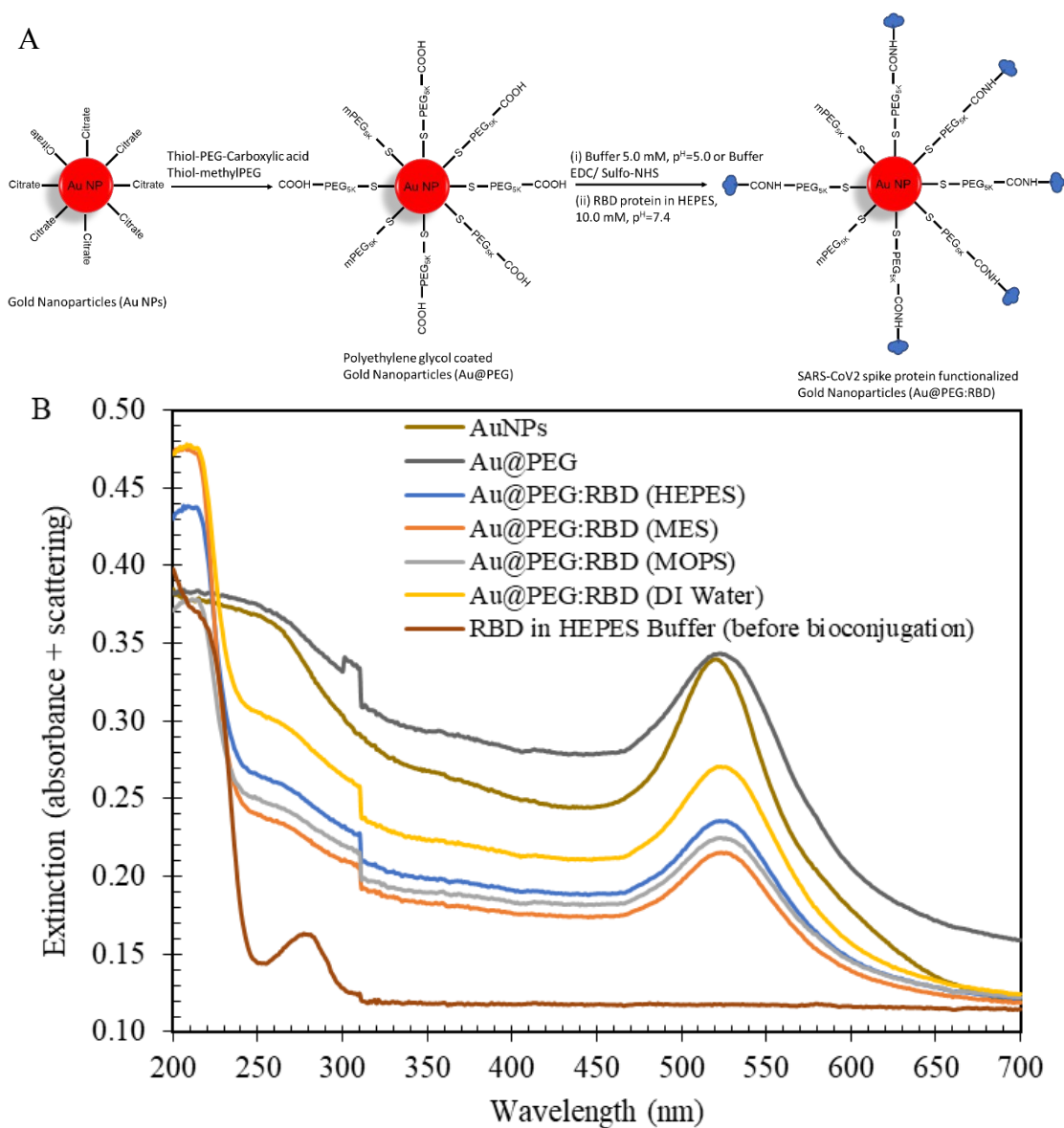


**Figure 4. 3: (A) Schematic illustration of functionalizing route of RBD functionalized AuNPs. (B) UV-Vis spectra showing  $\lambda_{max}$  of bare AuNPs, Au@PEG, Au@PEG:RBD and RBD protein in different buffer solutions.**

#### *4.4.3. Developing an x-ray luminescence immunoassay to detect SARS-CoV-2 antibodies (Proof of concept)*

Our previous studies with 50 nm GOS:Eu show around 90% reduction in x-ray luminescence intensity when attaching to 30 nm AuNPs. The positively charged PEG-NH<sub>3</sub><sup>+</sup> functionalized AuNPs were attached to GOS:Eu by adsorption (electrostatic interaction)<sup>29</sup>. Our current study showed that RBD functionalized AuNPs binding to anti-spike IgG functionalized GOS:Eu microparticles via antibody-antigen interaction. GOS:Eu were excited under UV light and imaged the light reduction in figure 4.4B. The sample clearly shows the decrease of emitted light compared to the control, containing PEG-coated AuNPs and GOS:Eu microparticles. Further, this observation was confirmed by X-ray excited optical luminescence spectra. The light reduction of AuNPs attached GOS:Eu microparticles is a factor of 1.81 compared to control (Figure 4.4D). With these results, we will be able to develop this immunoassay to detect and quantify biomarkers in vivo locally and continuously. The future direction is to use a GOS:Eu microparticles or a thin film and gold nanoparticles functionalized with biomolecules (e.g., antibodies) and covered with a semipermeable membrane. The molecules of interest (e.g., antigen) can pass through the membrane and make an antibody-antigen complex, resulting in low X-ray luminescence intensity. As the control region, unfunctionalized microparticles or a thin film and gold nanoparticles without functionalizing. In overall design includes two areas, the control region which use as the spectral reference and the sample region.

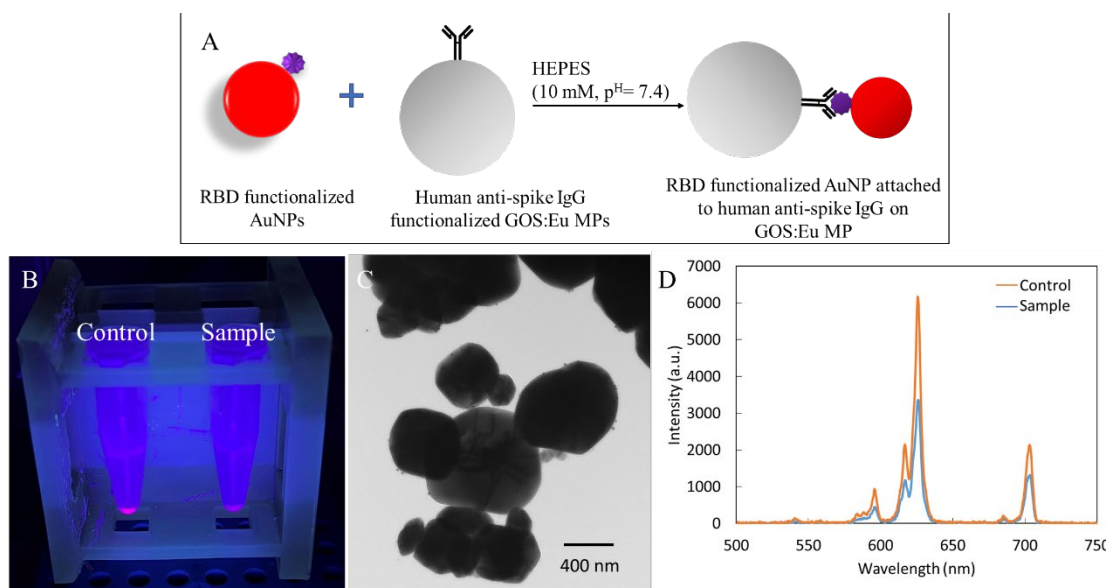


**Figure 4. 4: (A) Schematic illustration of RBD functionalized AuNPs binding to anti-spike IgG GOS:Eu microparticles. (B) Image showing control and the sample under UV light irradiation. (C) TEM image of RBD functionalized AuNPs bound to anti-spike IgG GOS:Eu microparticles. (D) X-ray excited optical luminescence of control and the sample.**

#### 4.5. Conclusions

Here, plasmonic and X-ray luminescence nanoparticles were used to develop two immunoassays (a lateral flow assay and an implantable immunoassay). The visible light scattering and absorption of gold nanoparticles and X-ray luminescence emitted by X-ray scintillators (GOS:Eu) are used to detect SARS-CoV-2 antibodies. To target the SARS-CoV-2 antibodies specifically, gold nanoparticles were functionalized with antigens. In summary, AuNPs were coated using PEG and functionalized with SARS-CoV-2 spike proteins using EDC/ Sulfo NHS coupling. Also, we have functionalized GOS:Eu microparticles with anti-spike antibodies using a similar approach. Using these particles, we have shown the capability of developing an x-ray luminescence immunoassay to detect SARS-CoV-2 antibodies. The significance of this proof of concept is it can be

developed as an implantable immunoassay in the future. Further, the designed LFA can also be developed as commercial LFA to detect SARS-CoV-2 antibodies.

#### 4.6. Acknowledgments

This work was funded by the South Carolina COVID Fund and NIH NIBIB R01EB026646 for the X-ray luminescence imaging. We would like to thank Dr. Delphine Dean and Dr. Congyue Peng from the Department of bioengineering, and IIT Ctr Medical Devices/Sensor, Clemson University for their collaboration.

#### 4.7. References

- (1) Sapsford, K. E.; Algar, W. R.; Berti, L.; Gemmill, K. B.; Casey, B. J.; Oh, E.; Stewart, M. H.; Medintz, I. L. Functionalizing Nanoparticles with Biological Molecules: Developing Chemistries That Facilitate Nanotechnology. *Chem. Rev.* **2013**, *113* (3), 1904–2074. <https://doi.org/10.1021/cr300143v>.
- (2) Reth, M. Matching Cellular Dimensions with Molecular Sizes. *Nat Immunol* **2013**, *14* (8), 765–767. <https://doi.org/10.1038/ni.2621>.
- (3) a. COVID Live - Coronavirus Statistics - Worldometer <https://www.worldometers.info/coronavirus/> (accessed 2022 -01 -08)., b. CDC. Coronavirus Disease 2019 (COVID-19) <https://www.cdc.gov/coronavirus/2019-ncov/variants/variant-classifications.html> (accessed 2022 -01 -05)., c. Commissioner, O. of the. COVID-19 Vaccines. *FDA* **2022**.

- (4) Weitz, J. S.; Beckett, S. J.; Coenen, A. R.; Demory, D.; Dominguez-Mirazo, M.; Dushoff, J.; Leung, C.-Y.; Li, G.; Măgălie, A.; Park, S. W.; Rodriguez-Gonzalez, R.; Shivam, S.; Zhao, C. Y. Modeling Shield Immunity to Reduce COVID-19 Epidemic Spread. *Nat Med* **2020**, *26* (6), 849–854. <https://doi.org/10.1038/s41591-020-0895-3>.
- (5) Lee, W.; Straube, S.; Sincic, R.; Noble, J. A.; Montoy, J. C.; Kornblith, A. E.; Prakash, A.; Wang, R.; Bainton, R. J.; Kurien, P. A. *Clinical Evaluation of a COVID-19 Antibody Lateral Flow Assay Using Point of Care Samples*; preprint; Infectious Diseases (except HIV/AIDS), 2020. <https://doi.org/10.1101/2020.12.02.20242750>.
- (6) Health, C. for D. and R. EUA Authorized Serology Test Performance. *FDA* **2021**.
- (7) Chvatal-Medina, M.; Mendez-Cortina, Y.; Patiño, P. J.; Velilla, P. A.; Rugeles, M. T. Antibody Responses in COVID-19: A Review. *Frontiers in Immunology* **2021**, *12*, 1208. <https://doi.org/10.3389/fimmu.2021.633184>.
- (8) MacMullan, M. A.; Ibrayeva, A.; Trettner, K.; Deming, L.; Das, S.; Tran, F.; Moreno, J. R.; Casian, J. G.; Chellamuthu, P.; Kraft, J.; Kozak, K.; Turner, F. E.; Slepnev, V. I.; Le Page, L. M. ELISA Detection of SARS-CoV-2 Antibodies in Saliva. *Sci Rep* **2020**, *10* (1), 20818. <https://doi.org/10.1038/s41598-020-77555-4>.
- (9) Universal Lateral Flow Assay Kit (ab270537) | Abcam <https://www.abcam.com/universal-lateral-flow-assay-kit-ab270537.html> (accessed 2022 -02 -28).



- (10) Isho, B.; Abe, K. T.; Zuo, M.; Jamal, A. J.; Rathod, B.; Wang, J. H.; Li, Z.; Chao, G.; Rojas, O. L.; Bang, Y. M.; Pu, A.; Christie-Holmes, N.; Gervais, C.; Ceccarelli, D.; Samavarchi-Tehrani, P.; Guvenc, F.; Budykowski, P.; Li, A.; Paterson, A.; Yun, Y. F.; Marin, L. M.; Caldwell, L.; Wrana, J. L.; Colwill, K.; Sicheri, F.; Mubareka, S.; Gray-Owen, S. D.; Drews, S. J.; Siqueira, W. L.; Barrios-Rodiles, M.; Ostrowski, M.; Rini, J. M.; Durocher, Y.; McGeer, A. J.; Gommerman, J. L.; Gingras, A.-C. Persistence of Serum and Saliva Antibody Responses to SARS-CoV-2 Spike Antigens in Patients with COVID-19. *Sci. Immunol.* **2020**, *5* (52), eabe5511. <https://doi.org/10.1126/sciimmunol.abe5511>.
- (11) Tré-Hardy, M.; Wilmet, A.; Beukinga, I.; Favresse, J.; Dogné, J.-M.; Douxfils, J.; Blairon, L. Analytical and Clinical Validation of an ELISA for Specific SARS-CoV-2 IgG, IgA, and IgM Antibodies. *Journal of Medical Virology* **2021**, *93* (2), 803–811. <https://doi.org/10.1002/jmv.26303>.
- (12) Heinzl, C.; Pinilla, Y. T.; Elsner, K.; Friessinger, E.; Mordmüller, B.; Kremsner, P. G.; Held, J.; Fendel, R.; Kreidenweiss, A. Non-Invasive Antibody Assessment in Saliva to Determine SARS-CoV-2 Exposure in Young Children. *Frontiers in Immunology* **2021**, *12*.
- (13) Khutale, G. V.; Casey, A. Synthesis and Characterization of a Multifunctional Gold-Doxorubicin Nanoparticle System for PH Triggered Intracellular Anticancer Drug Release. *European Journal of Pharmaceutics and Biopharmaceutics* **2017**, *119*, 372–380. <https://doi.org/10.1016/j.ejpb.2017.07.009>.

- (14) Gao, J.; Huang, X.; Liu, H.; Zan, F.; Ren, J. Colloidal Stability of Gold Nanoparticles Modified with Thiol Compounds: Bioconjugation and Application in Cancer Cell Imaging. *Langmuir* **2012**, *28* (9), 4464–4471.  
<https://doi.org/10.1021/la204289k>.
- (15) Xue, Y.; Li, X.; Li, H.; Zhang, W. Quantifying Thiol–Gold Interactions towards the Efficient Strength Control. *Nat Commun* **2014**, *5* (1), 4348.  
<https://doi.org/10.1038/ncomms5348>.
- (16) Carbodiimide Crosslinker Chemistry - US  
[//www.thermofisher.com/us/en/home/life-science/protein-biology/protein-biology-learning-center/protein-biology-resource-library/pierce-protein-methods/carbodiimide-crosslinker-chemistry.html](http://www.thermofisher.com/us/en/home/life-science/protein-biology/protein-biology-learning-center/protein-biology-resource-library/pierce-protein-methods/carbodiimide-crosslinker-chemistry.html) (accessed 2022 -02 -28).
- (17) Figueroa, E. R.; Lin, A. Y.; Yan, J.; Luo, L.; Foster, A. E.; Drezek, R. A. Optimization of PAMAM-Gold Nanoparticle Conjugation for Gene Therapy. *Biomaterials* **2014**, *35* (5), 1725–1734.  
<https://doi.org/10.1016/j.biomaterials.2013.11.026>.
- (18) Wickramathilaka, M. P.; Tao, B. Y. Characterization of Covalent Crosslinking Strategies for Synthesizing DNA-Based Bioconjugates. *Journal of Biological Engineering* **2019**, *13* (1), 63. <https://doi.org/10.1186/s13036-019-0191-2>.
- (19) Bartczak, D.; Kanaras, A. G. Preparation of Peptide-Functionalized Gold Nanoparticles Using One Pot EDC/Sulfo-NHS Coupling. *Langmuir* **2011**, *27* (16), 10119–10123. <https://doi.org/10.1021/la2022177>.

(20) Acidity of Carboxylic Acids

[https://chem.libretexts.org/Bookshelves/Organic\\_Chemistry/Supplemental\\_Modules\\_\(Organic\\_Chemistry\)/Carboxylic\\_Acids/Properties\\_of\\_Carboxylic\\_Acids/Physical\\_Properties\\_of\\_Carboxylic\\_Acids/Acidity\\_of\\_Carboxylic\\_Acids](https://chem.libretexts.org/Bookshelves/Organic_Chemistry/Supplemental_Modules_(Organic_Chemistry)/Carboxylic_Acids/Properties_of_Carboxylic_Acids/Physical_Properties_of_Carboxylic_Acids/Acidity_of_Carboxylic_Acids) (accessed 2022 -02 -18).

(21) Areo, O.; Joshi, P. U.; Obrenovich, M.; Tayahi, M.; Heldt, C. L. Single-Particle Characterization of SARS-CoV-2 Isoelectric Point and Comparison to Variants of Interest. *Microorganisms* **2021**, 9 (8), 1606.

<https://doi.org/10.3390/microorganisms9081606>.

(22) Molecular weight and isoelectric point of various immunoglobulins

<https://www.agrisera.com/en/info/molecular-weight-and-isoelectric-point-of-various-immunoglobulins.html> (accessed 2022 -02 -18).

(23) Krebs, F.; Scheller, C.; Grove-Heike, K.; Pohl, L.; Wätzig, H. Isoelectric Point Determination by Imaged CIEF of Commercially Available SARS-CoV-2 Proteins and the HACE2 Receptor. *ELECTROPHORESIS* **2021**, 42 (6), 687–692.

<https://doi.org/10.1002/elps.202100015>.

(24) Computational prediction of the effect of amino acid changes on the binding affinity between SARS-CoV-2 spike RBD and human ACE2

<https://www.pnas.org/doi/abs/10.1073/pnas.2106480118> (accessed 2022 -02 -28).

(25) Zhang, H.; Wang, W.; Akinc, M.; Mallapragada, S.; Travesset, A.; Vaknin, D. Assembling and Ordering Polymer-Grafted Nanoparticles in Three Dimensions.

*Nanoscale* **2017**, 9 (25), 8710–8715. <https://doi.org/10.1039/C7NR00787F>.

- (26) Nicoară, R.; Ilieș, M.; Uifălean, A.; Iuga, C. A.; Loghin, F. Quantification of the PEGylated Gold Nanoparticles Protein Corona. Influence on Nanoparticle Size and Surface Chemistry. *Applied Sciences* **2019**, *9* (22), 4789.  
<https://doi.org/10.3390/app9224789>.
- (27) Sardari, R. R. R.; Zarchi, S. R.; Hajihosseini, S.; Aghili, Z.; Rasoolzadeh, R.; Imani, S.; Borna, H.; Zand, A. M.; Nejadmoghadam, A.; Ghalavand, M.; Panahi, Y. Identification of an Independent Measurement Method for Denaturation Studies of Cytochrome C. *Int. J. Electrochem. Sci.* **2013**, *8*, 10.
- (28) Lin, L.; Jiang, W.; Xu, L.; Liu, L.; Song, S.; Kuang, H. Development of IC-ELISA and Immunochromatographic Strip Assay for the Detection of Flunixin Meglumine in Milk. *Food and Agricultural Immunology* **2018**, *29* (1), 193–203.  
<https://doi.org/10.1080/09540105.2017.1364710>.
- (29) Chen, H.; E. Longfield, D.; S. Varahagiri, V.; T. Nguyen, K.; L. Patrick, A.; Qian, H.; G. VanDerveer, D.; N. Anker, J. Optical Imaging in Tissue with X-Ray Excited Luminescent Sensors. *Analyst* **2011**, *136* (17), 3438–3445.  
<https://doi.org/10.1039/C0AN00931H>.

## CHAPTER FIVE

### X-RAY STIMULATED EGG EJECTION OF *C. ELEGANS*

*The material in this chapter was published as a pre-print article and submitted for peer-reviewed publication: Cannon, K. E.; Ranasinghe, M.; Do, A.; Pierce, H. M.; Millhouse, P. W.; Roychowdhury, A.; Foulger, S.; Dobrunz, L.; Anker, J. N.; Bolding, M. LITE-1 Dependent X-Ray Sensitivity in *C. elegans*. bioRxiv 2019, 766568. <https://doi.org/10.1101/766568>.*

*The experiments in the paper were initiated and carried out with the collaboration of the University of Alabama at Birmingham (Kelli Cannon, Dr. Mark Bolding). This chapter includes only the experiments conducted alone by the author.*

#### **5.1. Abstract**

In the previous chapters, the dissertation discussed on optical properties of plasmonic and X-ray luminescence nanoparticles and functionalizing them to develop immunosensors. This chapter focuses on a somewhat different concept related to optogenetics, which uses visible light to stimulate genetically modified neurons and control animal behavior. Specifically, this chapter discusses the discovery of X-ray-induced behavior of *C. elegans*, like X-ray luminescence nanoparticles use X-ray to produce visible light, X-ray is used to stimulate the LITE-1 photoreceptor of *C. elegans*.

Many research groups explore alternative light sources to use in optogenetics. Several research groups are researching to use of visible light generated from X-ray luminescence nanoparticles to stimulate neurons. One of the main objectives of

synthesizing bright X-ray luminescence nanoparticles (described in chapter 3) is to use them in neuron stimulating studies in *C. elegans*. The initial concept is to synthesize and functionalize X-ray nanoparticles to attach to genetically modified *C. elegans* neurons and control their behavior with the visible light exposed to X-ray. However, When the control study was performed, we observed that *C. elegans* (wild-type) avoid X-ray beams (without nanophosphors). Here, we describe a study that monitors *C. elegans* behavior when exposed to X-rays. In the study, two strains of *C. elegans* (wild type N2, transgenic *Pmyo-3::lite-1*) were exposed to an X-ray beam with 0 (no X-ray) and 1 Gy/s radiation doses to study their locomotory and ovulation behavior, respectively. At 1 Gy/s radiation dose, wild-type N2 moved away from the X-ray beam spot with increased locomotory movement. *Pmyo-3::lite-1*, which was transgenically expressed LITE-1 photoreceptor in X-ray insensitive body wall muscles, showed ovulation when exposed to X-ray. These findings may be vital for understanding the mechanism of LITE-1 signaling, how organisms respond to radiation, and, more importantly, developing optogenetics tools to stimulate transgenically modified neurons in deep tissue using X-rays.

## **5.2. Introduction**

In previous chapters (1-4), the optical properties of plasmonic and X-ray luminescence nanoparticles were discussed. Chapter two studied light scattering due to LSPR of plasmonic nanoparticles by developing a mechanical approach to preparing the size/ shape tuning of localized surface plasmon resonance and spatial patterns. Like chapter two, chapter three discussed several methods to enhance the X-ray excited optical

luminescence intensity of X-ray luminescence nanoparticles and used in high-resolution imaging through tissue. In chapter four, both types of particles were brought together to develop two immunosensors that use the advantage of surface area to functionalize with biomolecules and optical properties to detect biomarkers. This chapter discusses a different concept but related to X-ray sensing and change in animal (*C. elegans*) behavior due to X-ray stimulation. *C. elegans* are widely used in optogenetic studies, and also, they are sensitive to light (UV, blue light) even without optogenetic manipulations. Like in chapters three and four, here, an X-ray is used; however, it is used to stimulate neurons in this scenario. Also, recently scientists have been researching to use X-ray luminescence nanoparticles in optogenetic studies as a light source to stimulate neurons. This is discussed further in the next paragraph. However, this chapter includes a research project that was carried out to discover the X-ray stimulated behavior of *C. elegans*.

Optogenetics uses light to activate light-sensitive photoreceptors (opsins) located in the plasma membrane of neurons that permit spatial and temporal control of neuronal activities<sup>1</sup>. Since its discovery in 2005, optogenetics has become a vital tool that has led to many discoveries (E.g., identifying the connection between dopamine behavior related to pain and fear<sup>2</sup>, treating chronic pain<sup>3</sup>) and has been extensively developed and adapted. However, there are many limitations associated with the light source. The most common light sources used in optogenetics are fiber optics, implantable light sources (LED light), and cranial windows are used to guide light through the skull<sup>4</sup>. Therefore, applying optogenetics has many limitations, such as invasive, limited fields of view, and light scattering and absorption through tissue.

Consequently, researchers worldwide are investigating alternative light sources such as near-infrared (NIR), X-ray, and injectable light sources (radioluminescence nanoparticles). Recently, several groups have been exploring a technique called X-ray optogenetics (x-genetics)<sup>5-7</sup>, which uses radioluminescence particles (RLPs) to inject and locate close to the neurons. These particles can generate visible range light by X-ray attenuation and activate transgenically expressed photoreceptors. However, the major limitation here is to produce enough light to activate neurons. Therefore, we are investigating highly sensitive photoreceptors (E.g., G-protein coupled receptors) that can overcome the activation barrier using fewer photons. We came across LITE-1, an unusual UV-sensitive G-protein coupled receptors (GPCR) photoreceptor protein found in *C. elegans* that has been shown to absorb photons orders of magnitude more efficiently than several common opsins<sup>8</sup>.

*C. elegans* is a tiny, free-living, transparent nematode (roundworm) that lives in a soil environment. The length of an adult worm is about 1-1.5mm. They are easy to grow on a petri dish seeded with *Escherichia coli* as the food source. Also, they are fast-growing animals with a short life cycle (3 days). It is difficult to see them with the naked eye because of their small size (~1 mm) and transparency. However, we can use dissecting microscopes to visualize their movements, eating habits, developments, and laying eggs; confocal microscopes can be used to see cell development and function at a single-cell resolution. Further, proteins and other cell components can be visualized by fluorescence staining. *C. elegans* is a powerful model for eukaryotic genetic studies.



They are the only animal for which the complete atlas of synaptic connectivity has been mapped and the first multicellular organism with a complete genome sequence<sup>9,10</sup>.

In 2005, *C. elegans* neurons were excited with optogenetic manipulations for the first time<sup>1</sup>. Since then, researchers have been using *C. elegans* to develop and test new opsins. Even without optogenetic manipulations, *C. elegans* is sensitive to light. It activates the GPCR photoreceptor and accelerates their locomotory rhythms as a response to UV or blue light.

We report the discovery of a LITE-1 dependent behavioral response to X-radiation descriptively in the paper (1<sup>st</sup> author Kelli Cannon, University of Alabama at Birmingham)<sup>11</sup>. In summary, to demonstrate the X-ray sensitivity of wild-type *C. elegans*, we observed worm activity before (10 s) and after (10 s) exposure to X-rays. The activity was measured in body area per minute using CeleST tracking software. After X-ray exposure, the worms showed a robust increase in activity (locomotory rhythm) and moved away from the X-ray beam spot. The X-ray dose-response was also monitored by increasing the X-ray dose (0-1 Gy/s), which increased the worm activity as we increased the X-ray dose. These results are similar to the response seen in wild-type *C. elegans* to UV stimulation<sup>12</sup>. Then, to identify the photoreceptor (LITE-1 and, or GUR-3) responsible for the behavior three mutant strains (dysfunctional LITE-1 (*lite-1(ce314)* X), GUR-3 (*gur-3(ok2245)* X) and both LITE-1 and GUR-3 (*lite-1(ce314)* X *gur-3(ok2245)* X)) were used with wild-type *C. elegans* and exposed to 1 Gy/s X-ray. GUR-3 muted showed a significant increase in response to X-ray stimulation similar to the wild-type strain. LITE-1-muted strains showed a negligible increase in X-ray stimulation

suggesting LITE-1 photoreceptor is responsible for X-ray stimulated behavior of *C. elegans*.

Further, we show that LITE-1 can confer X-ray sensitivity when transgenically expressed in otherwise X-ray insensitive cells. To determine LITE-1 can confer X-ray sensitivity to X-ray insensitive cells *pmyo-3::lite-1 C. elegans*, which transgenically express LITE-1 in myocytes, were used. The paralysis and egg ejection study using *pmyo-3::lite-1* showed induced paralysis and egg ejection. When exposed to X-ray, induced paralysis and egg ejection were not observed in wild-type *C. elegans*. The previous UV radiation studies show similar results in LITE-1 mediated muscle contraction in *pmyo-3::lite-1*<sup>8,12</sup>.

Our study is the first demonstration of X-ray mediated modulation of cellular electrical activity that has similar functionality to optogenetics but with the advantage of not delivering light via invasive optic fiber implants or RLPs. Here, we describe X-ray stimulated egg ejection (ovulation) of *C. elegans* with transgenically expressed LITE-1 photoreceptor in X-ray insensitive body wall muscles (motor cells).

### **5.3. Methods**

#### *5.3.1. Growing, maintaining, and preparing C. elegans plates in the laboratory*

*C. elegans* were grown on nematode growth media agar (NGM) plates. NGM agar plates were prepared using commercially available NGM agar powder (Sigma-Aldrich) NGM agar powder (5.75 g) was dispersed in 250 mL DI water. The mixture was heated to dissolve completely and turned into a clear solution. Then, it was autoclaved at 121 °C

(15 psi) for 20 mins. After autoclaving, it was kept to cool down to around 50 °C and previously prepared (autoclaved), biological grade  $\text{MgCl}_2$  (1M, 250 M) and  $\text{CaSO}_4$  (1M, 250 M) were added. Then, Nystatin (5 mg/mL in ETOH, 500 uL), fungicide was added to the prepared agar solution at around 37 °C and immediately poured into sterilized Petri dishes.

After solidifying and cooling down to room temperature, OP50 *E. coli* were inoculated using the spread plate method and incubated at 37 °C for overnight. *E. coli* containing Petri plates were cooled down to room temperature to transfer *C. elegans*. Then the worms were transferred using the “chuncking” technique wherein a sterilized scalpel or spatula is used to move a chunk of agar (1 cm x 1 cm) from an old plate to a fresh plate, as shown in Figure 5.1. (Worms were purchased from Carolina Biological Supply and given by University of Alabama at Birmingham.)

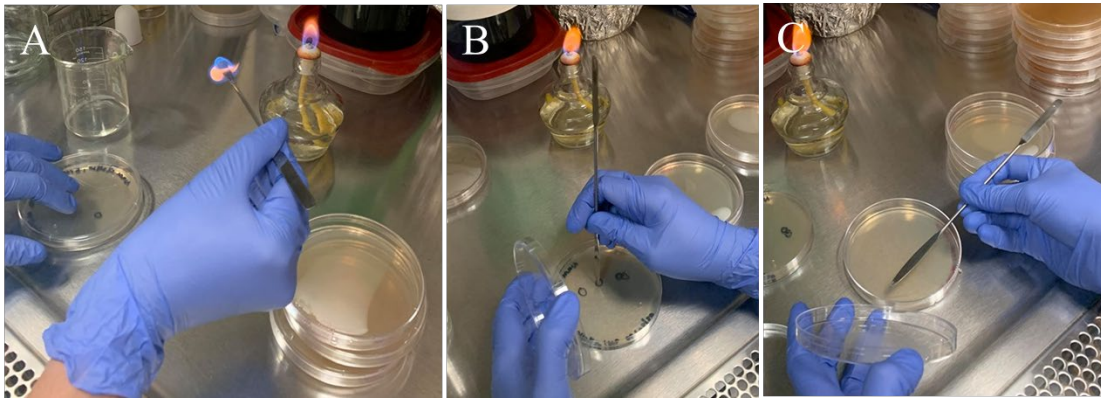


**Figure 5. 1: (A) Sterilizing a spatula by dipping in 70%ETOH and flaming. (B) Taking a 1 cm x 1 cm agar chunk from a NGM agar plate containing *C. elegans*. (C) transferring agar chunk into a fresh plate with an *E. coli* lawn.**

### 5.3.2. *Experiment setup*

**X-ray stimulation:** X-rays were generated by a iMOXS-MFR W-target X-ray unit with polycapillary optics (XOS) to focus the X-ray beam to a diameter of around 0.85 mm at the level of the agar surface, located approximately 5 cm from the tip of the capillary attachment. The unit was operated at 50 kV, and the current was varied from 0 to 600  $\mu$ A to achieve different stimulation intensities. A radiation dose of 1 Gy/s was approximated at the highest intensity using RADSticker dosimeter stickers (JP Laboratories, Inc.). An internal X-ray shutter was used to control the timing of the X-ray stimulation.

**Imaging Setup:** A custom imaging setup was used to record worm egg ejection responses to X-ray stimulation. Video data were recorded using an Amscope MU1003 10MP CMOS camera with a 0.7X-180X magnification lens. A white LED source provided backlighting with a diffuser. The X-ray unit was mounted above the stage. The stage was positioned using a motorized x-y translator controlled by the joystick of an Xbox controller (Microsoft, Redmond WA). The entire imaging setup was enclosed in a steel box with no detectable external X-ray leakage during use.

The irradiation zone was visualized using a piece of radiochromic film (Gafchromic, XR-QA2) placed on the agar surface (see Figure 5.2 inset). The camera recording software (Amscope 3.7) was used to annotate the video monitor with a circle outlining the irradiation zone as visualized with the Gafchromic film for targeting purposes.

### 5.3.3. Egg ejection experiments

**Experimental model:** *C. elegans* roundworms (wild type N2 and *Pmyo-3::lite-1* strains) were used to study X-ray stimulated positive regulation of locomotory and ovulation behavior. They were maintained at 22°C on nematode growth medium (NGM) agar plates seeded with OP50 *E. coli* lawns (Brenner, 1974). The wild-type N2 strain was used as a negative control. N2 nematodes were obtained from the Caehabditiris Genetics Center, which is funded by the NIH Office of Research Infrastructure Programs (P40 OD010440). *The lab of Dr. Shawn Xu generously provided Pmyo-3::lite-1 worms.*

**Experimental design:** All experiments were conducted on OP50-lawned 100 mm NGM plates inoculated with approximately 20-50 worms 72 hours prior. Looking at one worm per trial, 40 trials were conducted on worms from 8 different plates, targeting 3 to 7 individual worms from each plate. As described above, for the avoidance experiments, a piece of Gafchromic film was used to calibrate the location of the X-ray beam on the agar surface. An adult hermaphrodite was selected, and the stage was moved to position the worm in the center of the calibrated X-ray spot. Each trial began with 10 s during which baseline behavior was recorded with the X-ray shutter closed. Then, the shutter was opened to deliver a 15 s X-ray pulse. The responses of wild type and *pmyo-3::lite-1* transgenic nematodes were tested at 0 and 1 Gy/s by applying 0 and 600  $\mu$ A currents, respectively, to the X-ray tube at a voltage of 50 kV. Ten trials at each of the two intensities were conducted for each strain for 40 trials.

## 5.4. Results and discussion

X-ray stimulated ovulation experiments were carried out in an in-house built experiment set up (Figure 5.2). LED light source was used to illuminate the *C. elegans* containing NGM agar plates. The plates are placed on the sample holder connected to a motorized stage controlled by a joystick. The ovulation was video recorded using a camera located under the sample holder and visualized using AmScope software on the computer simultaneously. Prior to the X-ray exposure of *C. elegans* a Gafchromic film was exposed. The spot size and the location were marked using AmScope software to facilitate targeting the worms.

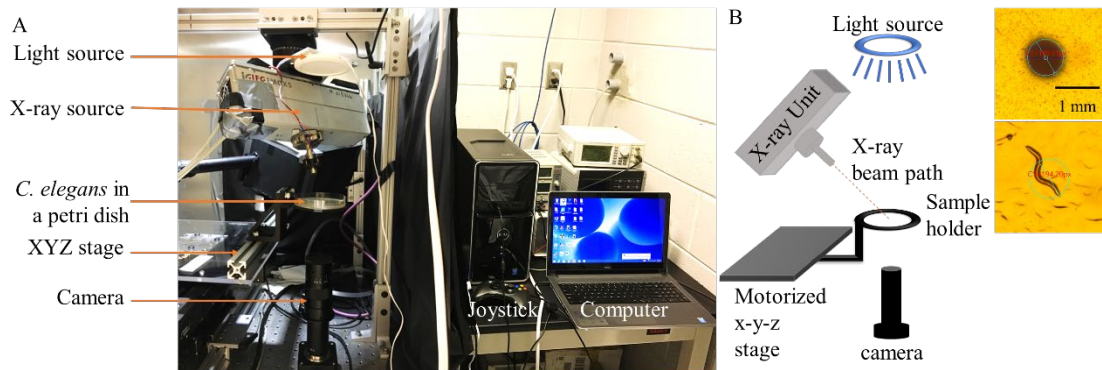


**Figure 5. 2: (A) A Photograph (B)schematic diagram of the experimental setup. The schematic diagram's right shows an X-ray spot visualized on a Grafchromic film and a worm targeted to X-ray exposure.**

Twenty worms from each strain (N2 and *Pmyo-3::lite-1*) were used in this experiment. Figure 5.3 shows the MATLAB generated images of *Pmyo-3::lite-1* and N2 strains 10s (A) before and (B) after the X-ray on. Before x-ray on worms showed no or fewer movements, and the purple region in Figures 5.3A1 and B1 shows the total movement during this period. After X-ray on, they show X-ray avoidance behavior in

figure 5.3A2 and B2. *Pmyo-3::lite-1* shows spastic motion/ less travel distance after X-ray compared to N2.

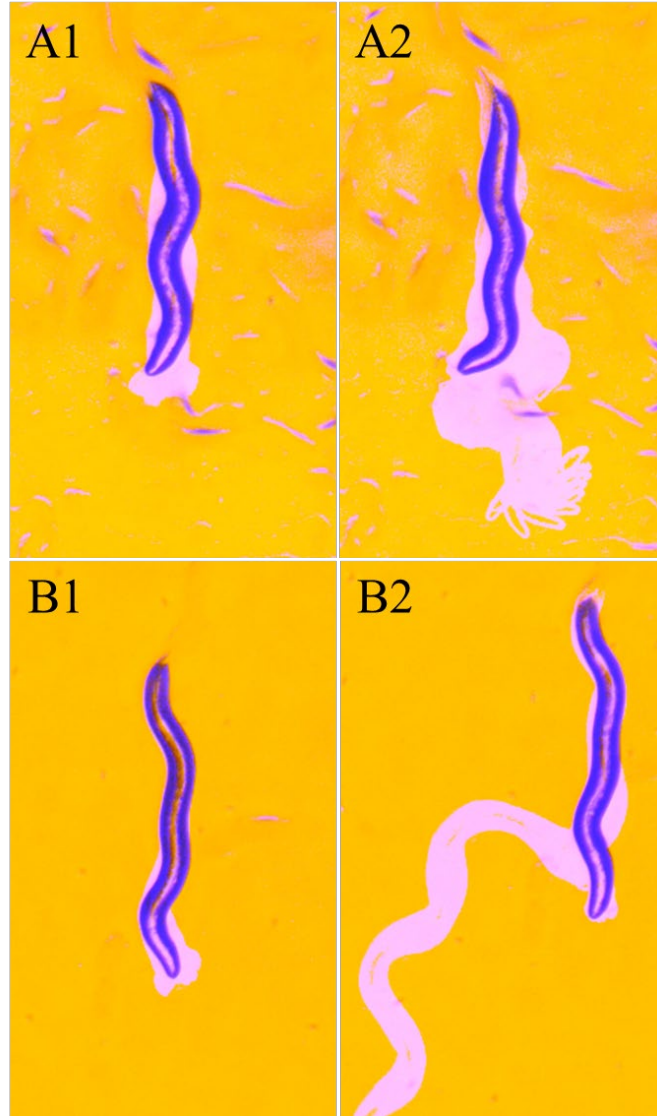


**Figure 5. 3: The behavior of *Pmyo-3::lite-1* (A1) before X-ray on and (A2) after X-ray on. The behavior of N2 (B1) before X-ray on and (B2) after X-ray on. The purple region corresponds to the worm movement during 10s before or 10s after the X-ray on. Worm shape and location are equivalent to the initial frame before or after the X-ray on.**

Further, 50% (5 out of 10 worms) of *Pmyo-3::lite-1* ejected eggs after X-ray on. They started ejecting eggs in 3-5s after x-ray on and usually ejected 1-4 eggs during 15s

exposure. Also, one worm ejected an egg immediately after the X-ray switched off (not included in 50%). Figure 5.4 shows MATLAB generated images 1s before (Figure 5.4A) and after (Figure 5.4B) ejecting an egg. The control N2 strain did not eject eggs when exposed to X-ray. These results suggest that LITE-1 can function as an X-ray sensitive receptor protein. It plays a critical role in the transduction of X-ray signals into ionic currents and neural activity to produce behavioral responses.

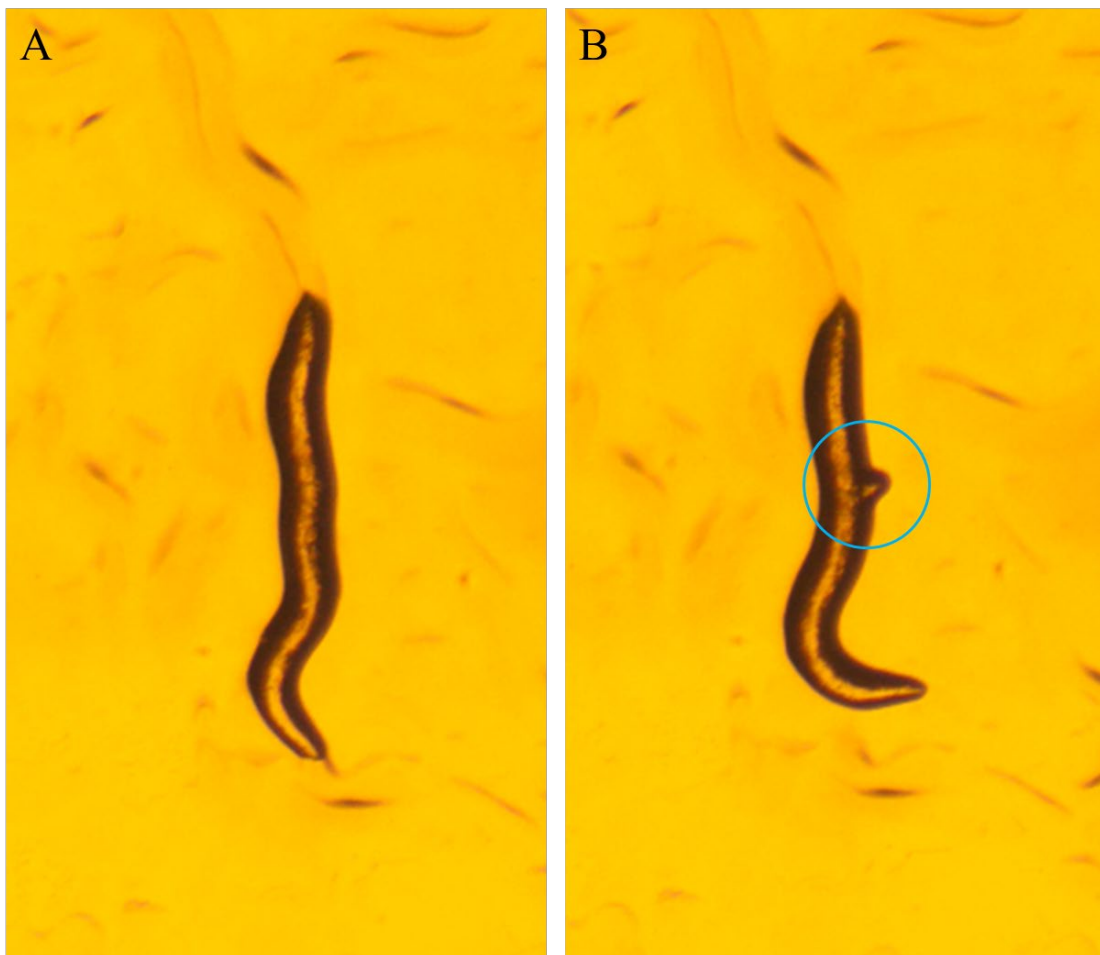


**Figure 5. 4:** MATLAB generated an image of *Pmyo-3::lite-1* 1s before and after ejecting an egg. The blue circle shows the ejected egg.



Figure 5.5. shows the number of ejected eggs by each worm after an X-ray on. The average number of ejected eggs is 1.10, and the standard deviation is 1.37. The standard deviation is higher than the average number of ejected eggs as we consider 0-4 as the number of ejected eggs and used 10 worms for the experiment. Further, the N2 strain (more than 10 worms) did not eject eggs when exposed to X-ray.

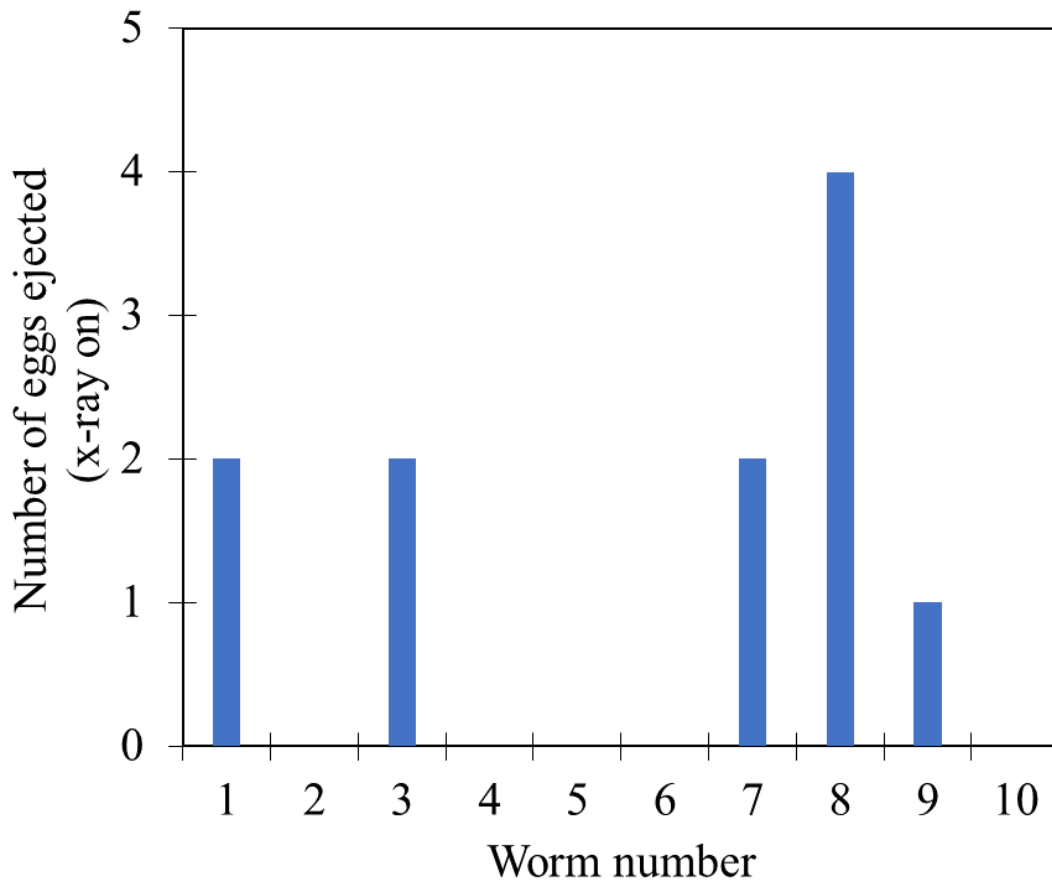


**Figure 5. 5:** A graph of the number of eggs ejected after X-ray on vs. worm number (*Pmyo-3::lite-1*).

The mechanisms by which X-ray activation of LITE-1 causes behavioral responses are not yet known. Given the similarity between UV- and X-ray-induced behaviors, it is reasonable to assume that the cellular and molecular pathways

downstream of LITE-1 activation are the same, regardless of which type of radiation is used to activate the receptor proteins.

## 5.5. Conclusions

In conclusion, we show that Wild type N2 nematodes avoid x-ray and *pmyo-3::lite-1* transgenic nematodes respond to X-ray. *pmyo-3::lite-1* transgenic nematodes, providing strong evidence that LITE-1 can function as an X-ray sensitive receptor in *C. elegans*. This is the first demonstration of X-genetic control of cellular electrical activity in intact, behaving animals. Future studies will reveal whether LITE-1 can enable minimally invasive X-genetic neural control in mammalian animal models.

## 5.6. Acknowledgments

This work is funded by NSF Track II EPSCoR OIA-1632881. The experiments described in the introduction section (including the discovery of LITE-1 photoreceptor) were designed and planned by Kelli Cannon. We would like to thank Dr. Mark Bolding and Kelli Cannon for their collaboration.

## 5.7. Reference

- (1) Boyden, E. S.; Zhang, F.; Bamberg, E.; Nagel, G.; Deisseroth, K. Millisecond-Timescale, Genetically Targeted Optical Control of Neural Activity. *Nat Neurosci* **2005**, 8 (9), 1263–1268. <https://doi.org/10.1038/nn1525>.
- (2) Wenzel, J. M.; Oleson, E. B.; Gove, W. N.; Cole, A. B.; Gyawali, U.; Dantrassy, H. M.; Bluett, R. J.; Dryanovski, D. I.; Stuber, G. D.; Deisseroth, K.; Mathur, B. N.;

Patel, S.; Lupica, C. R.; Cheer, J. F. Phasic Dopamine Signals in the Nucleus Accumbens That Cause Active Avoidance Require Endocannabinoid Mobilization in the Midbrain. *Current Biology* **2018**, *28* (9), 1392-1404.e5.  
<https://doi.org/10.1016/j.cub.2018.03.037>.

- (3) Dhandapani, R.; Arokiaraj, C. M.; Taberner, F. J.; Pacifico, P.; Raja, S.; Nocchi, L.; Portulano, C.; Franciosa, F.; Maffei, M.; Hussain, A. F.; de Castro Reis, F.; Reymond, L.; Perlas, E.; Garcovich, S.; Barth, S.; Johnsson, K.; Lechner, S. G.; Heppenstall, P. A. Control of Mechanical Pain Hypersensitivity in Mice through Ligand-Targeted Photoablation of TrkB-Positive Sensory Neurons. *Nat Commun* **2018**, *9* (1), 1640. <https://doi.org/10.1038/s41467-018-04049-3>.
- (4) Aravanis, A. M.; Wang, L.-P.; Zhang, F.; Meltzer, L. A.; Mogri, M. Z.; Schneider, M. B.; Deisseroth, K. An Optical Neural Interface: In Vivo Control of Rodent Motor Cortex with Integrated Fiberoptic and Optogenetic Technology. *J Neural Eng* **2007**, *4* (3), S143-156. <https://doi.org/10.1088/1741-2560/4/3/S02>.
- (5) Bartley, A. F.; Abiraman, K.; Stewart, L. T.; Hossain, M. I.; Gahan, D. M.; Kamath, A. V.; Burdette, M. K.; Andrabe, S.; Foulger, S. H.; McMahon, L. L.; Dobrunz, L. E. LSO:Ce Inorganic Scintillators Are Biocompatible With Neuronal and Circuit Function. *Frontiers in Synaptic Neuroscience* **2019**, *11*, 24.  
<https://doi.org/10.3389/fnsyn.2019.00024>.
- (6) Berry, R.; Getzin, M.; Gjestebj, L.; Wang, G. X-Optogenetics and U-Optogenetics: Feasibility and Possibilities. *Photonics* **2015**, *2* (1), 23–39.  
<https://doi.org/10.3390/photonics2010023>.

- (7) Matsubara, T.; Yanagida, T.; Kawaguchi, N.; Nakano, T.; Yoshimoto, J.; Sezaki, M.; Takizawa, H.; Tsunoda, S. P.; Horigane, S.; Ueda, S.; Takemoto-Kimura, S.; Kandori, H.; Yamanaka, A.; Yamashita, T. *Remote Control of Neural Function by X-Ray-Induced Scintillation*; 2020; p 798702. <https://doi.org/10.1101/798702>.
- (8) Gong, J.; Yuan, Y.; Ward, A.; Kang, L.; Zhang, B.; Wu, Z.; Peng, J.; Feng, Z.; Liu, J.; Xu, X. Z. S. The C. Elegans Taste Receptor Homolog LITE-1 Is a Photoreceptor. *Cell* **2016**, *167* (5), 1252-1263.e10. <https://doi.org/10.1016/j.cell.2016.10.053>.
- (9) Corsi, A. K. A Transparent Window into Biology: A Primer on Caenorhabditis Elegans. *WormBook* **2015**, 1–31. <https://doi.org/10.1895/wormbook.1.177.1>.
- (10) Husson, S. J.; Gottschalk, A.; Leifer, A. M. Optogenetic Manipulation of Neural Activity in C. Elegans: From Synapse to Circuits and Behavior. 28.
- (11) Cannon, K. E.; Ranasinghe, M.; Do, A.; Pierce, H. M.; Millhouse, P. W.; Roychowdhury, A.; Foulger, S.; Dobrunz, L.; Anker, J. N.; Bolding, M. LITE-1 Dependent X-Ray Sensitivity in C. Elegans. *bioRxiv* **2019**, 766568. <https://doi.org/10.1101/766568>.
- (12) Edwards, S. L.; Charlie, N. K.; Milfort, M. C.; Brown, B. S.; Gravlin, C. N.; Knecht, J. E.; Miller, K. G. A Novel Molecular Solution for Ultraviolet Light Detection in Caenorhabditis Elegans. *PLOS Biology* **2008**, *6* (8), e198. <https://doi.org/10.1371/journal.pbio.0060198>.

## CHAPTER SIX

### SUMMARY AND FUTURE WORK

#### 6.1. Introduction

This part of the dissertation summarizes the research projects discussed in chapters two, three, and four and their future directions. Materials with at least one dimension in the range of 1- 100 nm are considered to be nanoparticles, and they can have interesting optical, magnetic, chemical, biological, or other properties compared to their atomic levels and bulk materials. Also, compared to fluorescence dyes, they have a large surface area where biomolecules can be attached and target biomarkers *in vitro* and *in vivo* for bioimaging and sensing applications. Here, we are interested in studying the optical properties of plasmonic and X-ray luminescence nanoparticles and their applications in bioimaging and sensing.

In chapter two, light scattering due to LSPR of plasmonic nanoparticles was studied. The size and shape of plasmonic nanoparticles (Au and Ag) were changed using a mechanical force from ~90 nm to 180 nm and nanospheres to nanodiscs. The change in the size/shape of plasmonic nanoparticles resulted in a red-shift in scattering spectra compared to nanospheres. Another method was developed to prepare nanoparticle arrays with shape tunned nanoparticles, and these nanoparticle patterns are visible under a dark field microscope and to the naked eye. These nanoparticle arrays can be used in multi-diagnostic platforms in the future. Like plasmonic nanoparticles, the optical properties of X-ray luminescence nanoparticles were studied in chapter 3. X-ray luminescence nanoparticles (~ 90-100 nm) were synthesized, and methods to enhance their optical

luminescence were studied in terms of the concentration of dopants and decreasing crystal defects. Further, nanoparticles were used to obtain high-resolution optical images through tissue. Finally, plasmonic and X-ray luminescence nanoparticles were used to develop immunoassays, (1) a lateral flow assay to detect COVID-19 antibodies in human saliva using AuNPs, and (2) a proof of concept to develop an implantable immunoassay using combined optical properties of AuNPs and X-ray luminescence microparticles.

Chapter five includes a different research project. However, it is related to the main theme as it uses X-rays and discusses sensing X-ray radiation. It is the discovery of the LITE-1 photoreceptor of *C. elegans* sensitivity towards X-ray radiation. The X-ray stimulated behavior of *C. elegans* shows X-ray avoidance behavior of wild-type N2 and egg ejection of *pmyo-3::lite-1* transgenic nematodes when exposed to X-ray.

The following sections (6.2-6.5) summary and future work of each chapter are discussed.

## **6.2. Impressively printing patterns of gold and silver nanoparticles**

In summary, chapter two presents the development of nanoimprint lithography techniques that can be used to fabricate devices in biosensors, nanophotonic, etc. This simple and robust technique uses a mechanical approach to change the shape of plasmonic nanoparticles from nanospheres to nanodiscs and patterns them by placing stamps. A glass rolling pin attached to a force gauge was rolled over plasmonic nanoparticles coated glass slide to convert nanospheres to nanodiscs. A metal stamp or a glucose deposit was placed on NPs before rolling to pattern them. The resulting

nanoparticle shape change induces a red-shift in the localized surface plasmon resonance, while regions untouched by the stamp remain unchanged. Further, it shows a simple technique to transfer these patterns to a thin polymer film.

Nanorolls are produced using a slightly different approach (Figure 6.1B) described in chapter two as a future direction. A glass slide attached to a force gauge was slid on gold nanoparticles for this approach using shear to form “rolls” rather than simple compression, which formed flattened “pancakes.” However, the yield of nanorolls is meager; therefore, a more robust approach is required to increase the yield. During this process, nanoparticle fusion was also observed, which is vital in making thin films, studying nanoparticle growth mechanisms in synthesis, and optical properties during the fusion.

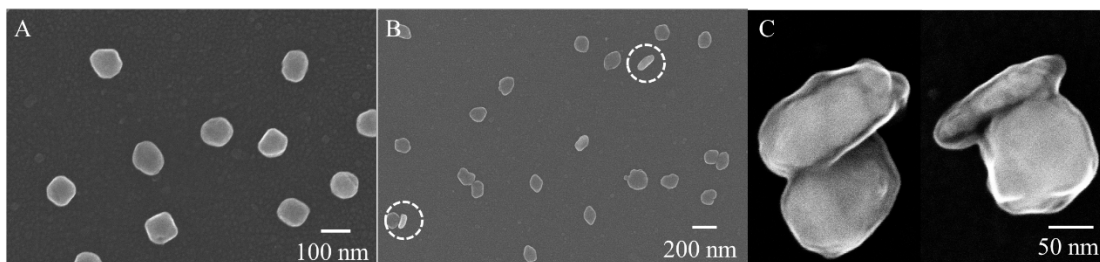


**Figure 6. 1: SEM images of Ag NPs (A) unrolled and (B) rolled AgNPs. (C) SEM image of fused NPs during the deformation process**

Although the research presented in this chapter shows a successful development of the nanoimprint lithography technique, the question remains in terms of possible applications. Our previous studies have proved an increase in surface area during the deformation process; therefore, carrying out an investigation to study the surface area increase by the crack formation, implementing catalytic/ enzymatic reactions, and developing bioassays can be possible applications. As a preliminary study, color

reduction of methyl orange was used in the presence of different sizes and concentrations of AgNPs (Figure 6.2). The results show the increase in reaction rate with small-sized particles due to the increase in the nanoparticle surface area.

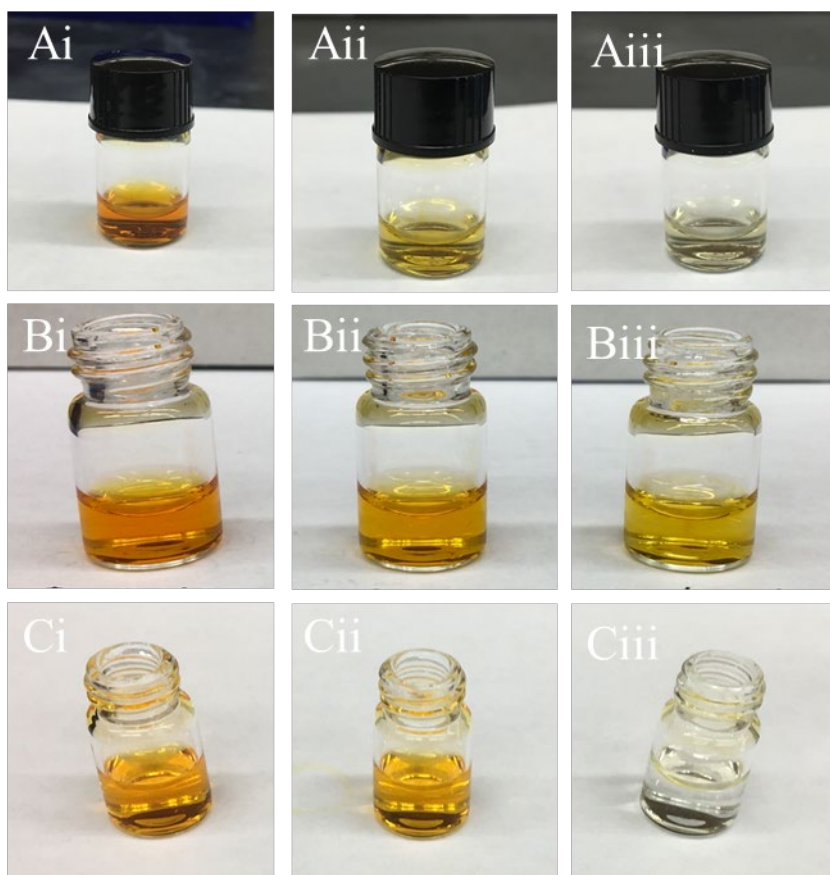


**Figure 6. 2: Methyl orange color reduction by  $\text{NaBH}_4$  using Ag NPs as a catalysts. (Ai-Ci) Negative controls. (Aii) 10 minutes and (Aiii) 15 minutes after adding 200  $\mu\text{L}$  of 1% (v/v) AgNPs. Five minutes after adding (Bii) 200  $\mu\text{L}$  and (Biii) 400  $\mu\text{L}$  of 1% (v/v) AgNPs. Five minutes after adding 100  $\mu\text{L}$  of (Cii) 100 nm and (Biii) 50 nm of 1% (v/v) AgNPs.**



### **6.3. X-ray excited luminescence spectroscopy and imaging with NaGdF<sub>4</sub>:Eu and Tb**

Chapter three explains a study to synthesize, functionalize and characterize X-ray luminescence nanoparticles. Also, a study was carried out to enhance the X-ray luminescence intensity. The nanoparticles synthesized using the hydrothermal method gave the highest luminescence intensity. Importantly, we selectively excited scintillator nanophosphors using a focused X-ray source to generate light and collect them through the tissue to generate high-resolution images, and XEOL was measured through tissue. We also showed that the particles could serve as MRI contrast agents.

Another characteristic feature of these materials is that the elements in the luminescence centers generate distinct spectra, and changing the host matrices creates a small yet clear spectral shift. (Figure 6.3) The fine structure changes due to different elements in the luminescence centers and host matrices can be observed under high-resolution gratings. The spectral distinction is important in detecting, quantifying, and imaging multiple biomarkers *in vivo*. Each type of nanoparticle can be functionalized with a unique biomolecule to target multiple biomarkers. This also allows imaging the distribution of target biomarkers locally using a focus X-ray beam.

Figures 6.3 A and B show the spectral differences between NaGdF<sub>4</sub>: Eu (10 mg) and Gd<sub>2</sub>O<sub>2</sub>S: Eu (GOS:Eu, 1 mg). To show that we could distinguish each type of particle in a mixture, we added NaGdF<sub>4</sub> particles (10 mg) synthesized by the hydrothermal method in chapter three in the presence of 1 mg of commercial 2.5  $\mu$ m GOS:Eu particles (UKL63/N-R1, Phosphor Technologies, Stevenage, England) and the X-ray luminescence spectra were taken. We used a higher mass of NaGdF<sub>4</sub> because it was less

bright than GOS:Eu. X-ray excited optical luminescence intensity was collected according to the procedure explained in chapter 3, section 3.3.9.

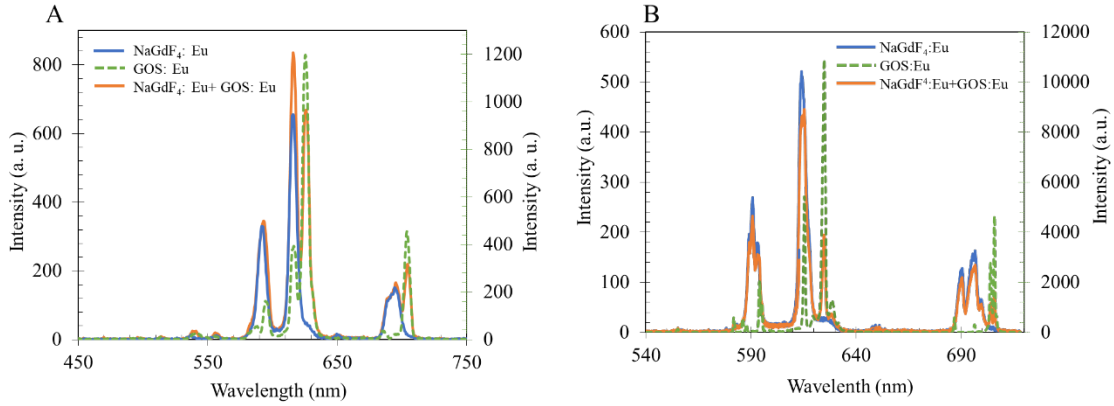


**Figure 6. 3: (A) Low resolution and (B) High-resolution XEOL spectra from NaGdF<sub>4</sub>:Eu, Gd<sub>2</sub>O<sub>2</sub>S:Eu and a mixture of both with spectrally distinct peaks.**

From the spectra, we calculated the limit of detection (LOD) and quantification (LOQ) of NaGdF<sub>4</sub>:Eu in the presence of Gd<sub>2</sub>O<sub>2</sub>S:Eu (1 mg) and vice versa (10 mg of NaGdF<sub>4</sub>:Eu in Gd<sub>2</sub>O<sub>2</sub>S:Eu). To calculate the LOD and LOQ of NaGdF<sub>4</sub>:Eu (for both simulation and experiment), X-ray luminescence spectra of Gd<sub>2</sub>O<sub>2</sub>S:Eu (1 mg) were obtained 10 times, and the standard deviation (SD) of intensity ratios at 616/626 (wavelength) and 695/703 (wavelength) was calculated. (LOD= 3\*SD/m, LOQ= 10\*SD/m, where m is the slope of the calibration curve). To calculate the LOD and LOQ of Gd<sub>2</sub>O<sub>2</sub>S:Eu (for both simulation and experiment), X-ray luminescence spectra of NaGdF<sub>4</sub>:Eu (10 mg) were obtained 10 times, and the standard deviation (SD) of intensity ratio at 626/616 (wavelength) and 703/695 (wavelength) was calculated. We note that these calculations apply only to the experimental conditions tested, and that changes in dose, optical collection efficiency and spectral resolution as well trial to trial sample

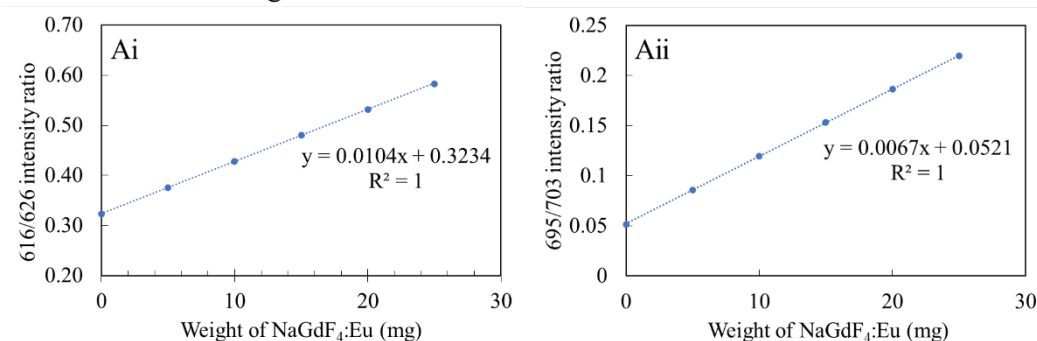
preparation will affect the values. Nonetheless, the studies do show that we can distinguish and quantify low concentrations of one scintillator type in the presence of a second scintillator, and the LOD provide estimates of where the signals become significant compared to noise from the samples with only one particle type.

To set expectations, the spectra were simulated using experimental XEOL of pure substances, NaGdF<sub>4</sub>: Eu (10 mg) and Gd<sub>2</sub>O<sub>2</sub>S: Eu (1mg). The intensity was calculated at different weights (for NaGdF<sub>4</sub>:Eu: 0- 30 mg and GOS:Eu: 0- 0.256 mg) for each substance. Then, the intensity ratio vs. weight graph was plotted (Figures 6.4 and 6.5, Ai and Aii) to determine the effect of the linear combination of pure substances. The noise was calculated as the standard division of pure substances and expected LOD and LOQ were calculated as explained above. According to the simulated data (Figure 6.4 Ai and Aii), the limit of detection of NaGdF<sub>4</sub>:Eu is 0.56 mg at 616/626 (wavelength) intensity ratio and 0.70 mg at 695/703 (wavelength) intensity. The limit of quantification is 1.88 mg and 2.34 mg at 616/626 and 695/703 (wavelength) intensity ratio.

Figures 6.4 Bi and Bii plot the experimental spectra from varying amounts of NaGdF<sub>4</sub>:Eu (0, 0.01, 0.04, 0.16, 0.64, 2.56 mg) added to a constant amount of GOS:Eu (1 mg). X-ray luminescence intensities were measured as explained in chapter 3, section 3.3.9. The experimental LOD of NaGdF<sub>4</sub>:Eu is 1.44 mg at 616/626 (wavelength) intensity ratio and 1.42 mg at 695/703 (wavelength) intensity. The LOQ is 4.80 mg and 4.75 mg at 616/626 and 695/703 (wavelength) intensity ratio. The LODs at two wavelength ratios are similar, and LOQs at two wavelength ratios are also similar. The slope and the intercept values show reasonable concurrence between simulated and experiment data.

The variation in LOD and LOQ in experimental and simulation data is mainly due to variation in noise. It is due to variation in the weight range (simulated data 0-25 mg, experimental data 0- 2.56 mg), sample preparation, and data collection.

Calibration curve using simulated data



Calibration curve using experimented data

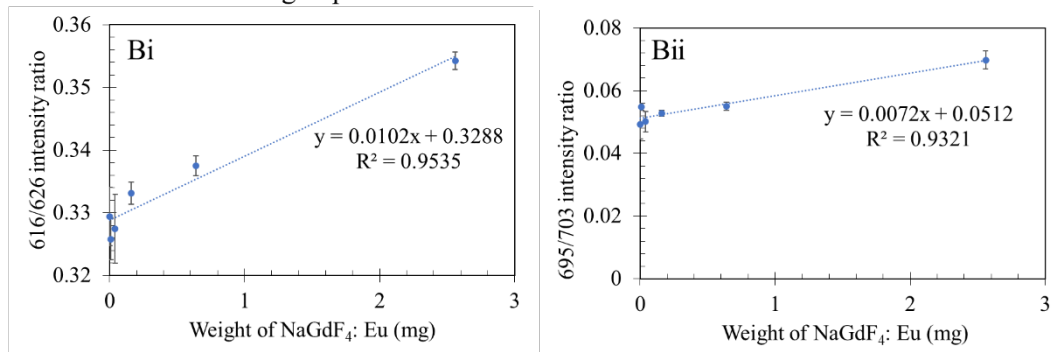


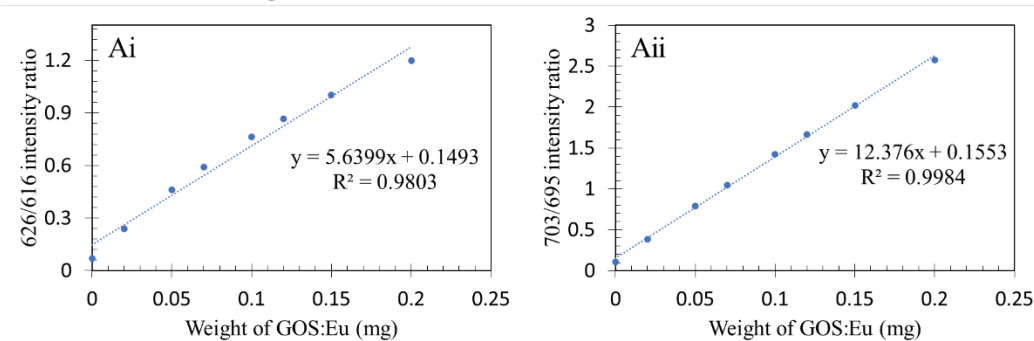
**Figure 6. 4: Calibration curve of (Ai) 616/626 nm intensity ratio and (Aii) 695/703 intensity ratio vs weight of NaGdF<sub>4</sub>:Eu (mg) of simulated data. Calibration curve of (Bi) 616/626 nm intensity ratio and (Bii) 695/703 intensity ratio vs weight of NaGdF<sub>4</sub>:Eu (mg) of experimented data.**

Also, we calculated the LOD and LOQ of GOS:Eu in the presence of NaGdF<sub>4</sub>:Eu (10 mg). first, the data were simulated using experimental XEOL of NaGdF<sub>4</sub>: Eu (10 mg), and the rest of the measurements and calculations were carried out as explained above. According to the simulated data (Figure 6.5 Ai and Aii), the limit of detection of GOS:Eu was 0.002 mg at 626/616 and 703/695 (wavelength) intensity ratios. The limit of

quantification is 0.006 mg and 0.007 mg at 626/616 and 703/695 (wavelength) intensity ratios.

To plot experimental data (Figures 6.5 Bi and Bii), varying amounts of GOS:Eu (0, 0.01, 0.02, 0.04, 0.08, 0.16, 0.32, 0.64 mg) were added to a fixed amount of NaGdF<sub>4</sub>:Eu (10 mg) and X-ray luminescence intensities and associated ratios were measured as explained in chapter 3 section 3.3.9. The experimental LOD of GOS:Eu is 0.002 mg at 626/616 (wavelength) intensity ratio and 0.003 mg at 703/965 (wavelength) intensity. The LOQ is 0.009 mg and 0.01 mg at 626/616 and 703/965 (wavelength) intensity ratios. The experimental LOD and LOQ of NaGdF<sub>4</sub>:Eu is higher than GOS:Eu by a factor of 700 and 500, respectively, because GOS:Eu is brighter than NaGdF<sub>4</sub>:Eu. For both NaGdF<sub>4</sub>:Eu and GOS:Eu, simulated LOD and LOQ are lower (better) than the experimental values, the slopes were similar, and the worse experimental LODs and LOQs were thus from more variation in experimental ratios at low GOS concentrations.

Calibration curve using simulated data



Calibration curve using experimented data

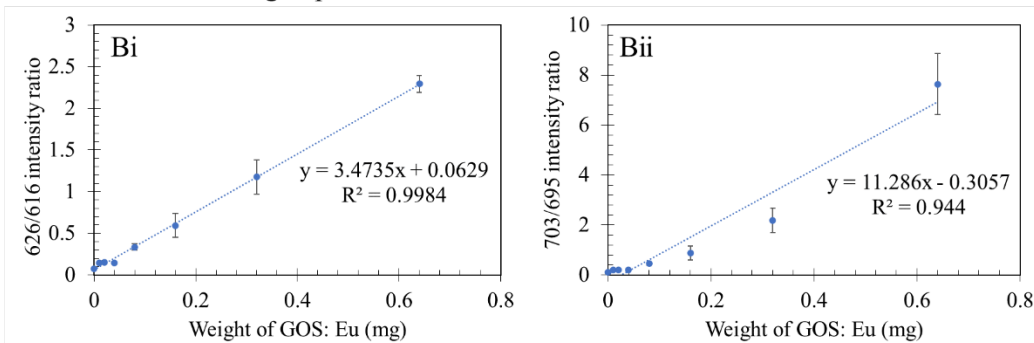


**Figure 6. 5: Calibration curve of (Ai) 626/616 intensity ratio and (Aii) 703/695 intensity ratio vs. weight of NaGdF<sub>4</sub>:Eu (mg) of simulated data. Calibration curve of (Ai) 626/616 intensity ratio and (Aii) 703/695 intensity ratio vs. weight of GOS:Eu (mg) of experimented data.**

This preliminary study shows that the GOS:Eu and NaGdF<sub>4</sub>:Eu are spectrally distinguished and potentially used in quantification applications. Further, GOS:Eu can be detected at low concentrations (0.002-0.003 mg) against a large background of NaGdF<sub>4</sub>:Eu (10 mg). Also, both the 620 and 700 nm peaks can be used with similar LOD. Generally, the 620 peaks are brighter, but the 700 nm peaks penetrate through thicker tissue. However, these results were only bulk spectral measurements, and further studies are required before use in imaging applications.

#### 6.4. Functionalizing radiodense particles and developing immunoassays to detect SARS-CoV-2 antibodies

In summary, chapter four discusses the development of two immunoassays. The 1<sup>st</sup> one is to develop an LFA using AuNPs to detect SARS-CoV-2 antibodies in human saliva. The second is to build an implantable immunoassay using AuNPs and X-ray luminescence microparticles. AuNPs and GOS:Eu microparticles were functionalized with SARS-CoV-2 spike proteins and human anti-spike IgG. This chapter shows the proof of concept of constructing both immunoassays. However, both immunoassays require further development and statistical analysis regarding the limit of detection, quantification, sensitivity, and specificity. Figure 6.6 shows the preliminary results of the RBD protein depletion assay to confirm the protein binding to AuNPs further. However, the assay was carried out in PBS buffer, resulting in the AuNPs flocculating and protein attaching to the low protein binding vial wall. Therefore, this experiment needs to be repeated in a different buffer like HEPES.

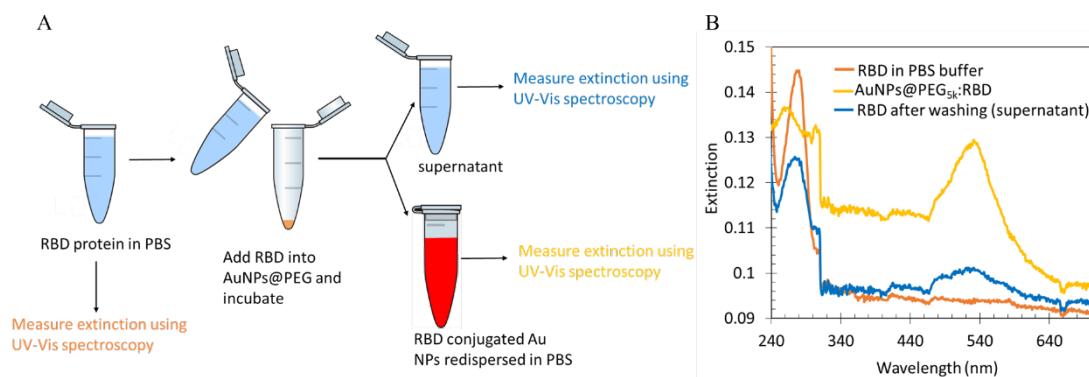


**Figure 6. 6: (A) Schematic illustration of protein depletion assay. (B) UV-Vis spectra show  $\lambda_{\max}$  of AuNPs after bioconjugation, RBD before, and after bioconjugation.**

## **6.5. X-ray stimulated egg ejection of *C. elegans***

Chapter five is related to the main theme as it uses X-rays and discusses sensing of X-ray radiation by photoreceptors. It includes the discovery of the LITE-1 photoreceptor of *C. elegans* sensitivity towards X-ray radiation. When X-ray radiation is focused onto wild-type N2, they avoid the X-ray beam, and *pmyo-3::lite-1* transgenic *C. elegans* eject eggs. As mentioned in chapter 5, *C. elegans* also show similar behavior with UV and blue light. Therefore, in the future, we will study their behavior by inserting X-ray luminescence nanoparticles into *C. elegans* and expect enhancement in their response (Ex. fast movements and egg ejection compared to only X-ray stimulation). It will also be interesting to distinguish the effect of increased X-ray absorption and photo-generated light by using luminescent particles with and without activator dopants to vary light intensity without affecting X-ray absorption.

## **6.6. Conclusion**

Nanomaterials are widely used in biomedical and other industries due to their interesting optical and surface area that can be functionalized with biomolecules to target biomarkers. This dissertation includes research work carried out to understand the fundamental properties and biomedical applications of plasmonic and X-ray luminescence nanoparticles. The research carried out to develop a mechanical method to pattern nanoparticle arrays will open up new avenues to study the fundamental properties of nanoparticle arrays with different shapes of nanoparticles. It also addresses one of the limitations to transferring these nanoparticle arrays onto thin films that currently use high



pressure and vacuum conditions. The X-ray luminescence nanoparticles synthesized using the hydrothermal method agree with the previous studies, resulting in high crystallinity and high X-ray luminescence. Further, thermal annealing can be used to enhance the X-ray luminescence intensity of a nanoparticle. It also opens up a new insight into changing the chemical structure of the lattice without changing the nanoparticle's shape by thermal annealing. Finally, these plasmonic and X-ray luminescence nanoparticles were used in developing immunoassays. The significance of X-ray luminescence nanoparticles and gold nanoparticles combined assay will open up new opportunities to build implantable immunoassays to detect analytes *in vivo* continuously and locally. X-ray stimulated behavior of *C. elegans* is the discovery of the sensitivity LITE-1 photoreceptor towards X-rays. Future studies will reveal whether LITE-1 can enable minimally invasive X-genetic neural control in mammalian animal models.

Overall, this dissertation shows the development of plasmonic and X-ray luminescence nanoparticles in bioimaging and sensing applications. Although these two nanoparticle systems have very different compositions and optical properties, they both have properties that depend upon nano-domain photophysics. Especially, plasmonic nanoparticles show LSPR when their size is large enough to free electron transport in the metal but relatively small compared to the incident visible or near infrared light; and bright X-ray luminescence nanoparticles can be achieved when domain size becomes large relative to energetic photoelectron and exciton diffusion lengths. By controlling nanoparticle size and or domain size, optical properties can be controlled and used for

many biological applications, which also have size and surface chemistry-dependent blood circulation and targeting properties. In the future, we hope to develop in vivo X-ray luminescence immunoassays and bioimaging agents using antibody-antigen interactions to coupling plasmonic and X-ray scintillating particles together with antigen dependent gold nanoparticle attachment and associated luminescence quenching. Overall, such nanomaterials have great promise for applications involving in situ sensing and high-resolution imaging through tissue.

## APPENDICES

### Appendix A

#### C. elegans x-ray avoidance behavior video analysis using MATLAB

```
cd('File location');
```

```
Ex: cd('D:\Research2\Spring 2020\C. elegans\N2 antioxidants\Control');
```

```
V1=VideoReader('Filename');
```

```
Ex: V1=VideoReader('N2C1.mp4');
```

```
numFrames = get(V1,'NumberOfFrames');
```

Number of frames, frame rate and other properties are located under “variables-V1”

```
I=read(V1,1);
```

1= 1<sup>st</sup> frame of the video

```
figure; imshow(I);
```

image of the 1<sup>st</sup> frame

```
Io01f1=read(V1,1);
```

```
Io01min(:,:)=Io01f1(:,:,3);
```

Minimum of the frame

```
Io01max(:,:)=Io01f1(:,:,3);
```

maximum of the frame

```
for i=1:260, Io01=read(V1,i); display(i);
```

```
Io01min(:,:)=min(Io01min,Io01(:,:,3));
```

```
Io01max(:,:)=max(Io01max ,Io01(:,:,3)); end;
```

```
I1colorb2=read(V1,1);
```

```
I1colorb2(:,:,3)=I1colorb2(:,:,3) + 10*(Io01max-Io01min);
```

adding max minus min in blue

```
figure; imshow(I1colorb2);
```

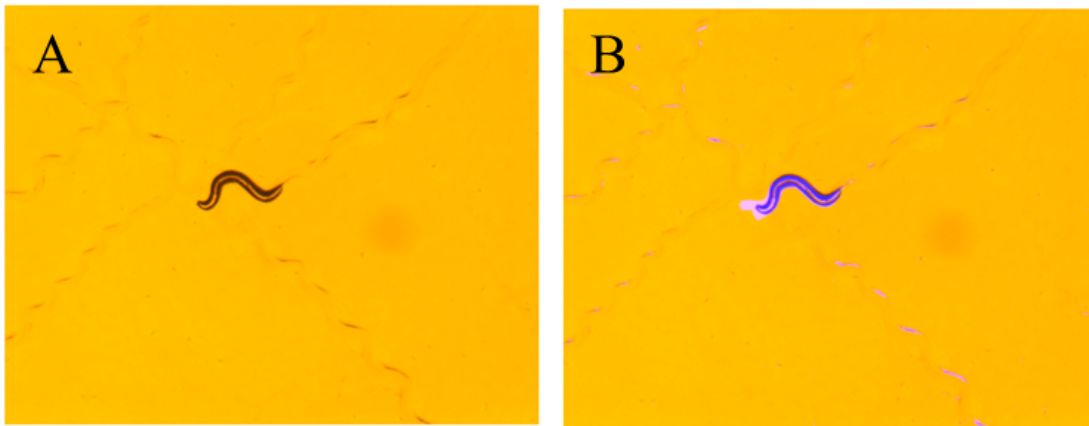


Figure A-1: MATLAB image generated from (A) frame number 1 and (B) frame number 260 subtracted by frame number 1.

```
I=read(V1,261);
```

```
figure; imshow(I);
```

```
Io01f1=read(V1,1);
```

```
Io01min(:,:,)=Io01f1(:,:,3);
```

```
Io01max(:,:,)=Io01f1(:,:,3);
```

```
for i=261:650, Io01=read(V1,i); display(i); Io01min(:,:,)=min(Io01min,Io01(:,:,3));
```

```
Io01max(:,:,)=max(Io01max ,Io01(:,:,3)); end;
```

```
I1colorb2=read(V1,261);
```

```
I1colorb2(:,:,3)=I1colorb2(:,:,3) + 10*(Io01max-Io01min);
```

```
figure; imshow(I1colorb2);
```

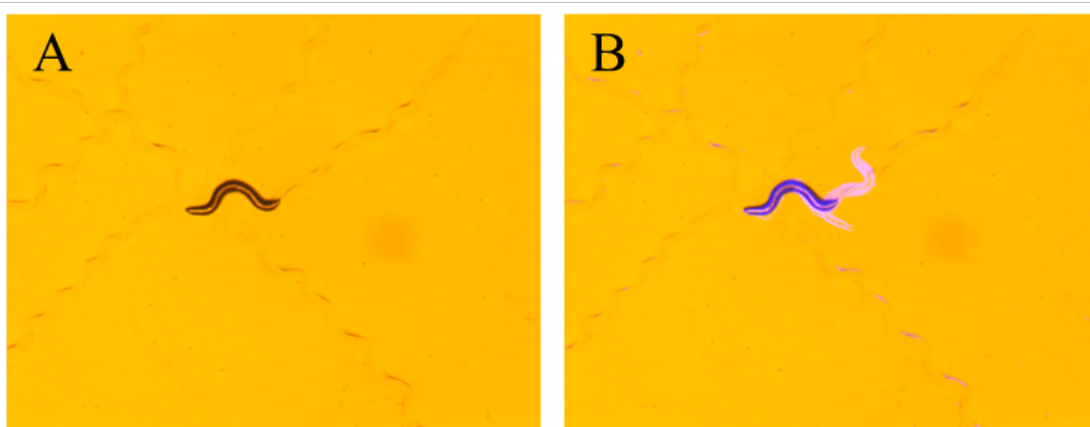


Figure A-2: MATLAB image generated from (A) frame number 261 and (B) frame number 650 subtracted by frame number 261

## Appendix B

### Copyrights

4/17/22, 3:04 PM

RightsLink Printable License

#### JOHN WILEY AND SONS LICENSE TERMS AND CONDITIONS

Apr 17, 2022

---

This Agreement between Meenakshi Ranasinghe ("You") and John Wiley and Sons ("John Wiley and Sons") consists of your license details and the terms and conditions provided by John Wiley and Sons and Copyright Clearance Center.

License  
Number 5291500236646

License date Apr 17, 2022

Licensed  
Content John Wiley and Sons  
Publisher

Licensed  
Content ChemPhysChem  
Publication

Licensed  
Content Title Synthesis and Optical Properties of Silver Nanoparticles and Arrays

Licensed  
Content George Chumanov, David D. Evanoff  
Author

Licensed  
Content Date Jul 1, 2005

Licensed  
Content 6  
Volume

Licensed  
Content 7  
Issue

<https://s100.copyright.com/AppDispatchServlet>

1/8



Home



Help ▾



Email Support



Sign in



Create Account

### Recent Advances in Optical Imaging with Anisotropic Plasmonic Nanoparticles



**Author:** Yinhe Peng, Bin Xiong, Lan Peng, et al

**Publication:** Analytical Chemistry

**Publisher:** American Chemical Society

**Date:** Jan 1, 2015

*Copyright © 2015, American Chemical Society*

#### PERMISSION/LICENSE IS GRANTED FOR YOUR ORDER AT NO CHARGE

This type of permission/license, instead of the standard Terms and Conditions, is sent to you because no fee is being charged for your order. Please note the following:

- Permission is granted for your request in both print and electronic formats, and translations.
- If figures and/or tables were requested, they may be adapted or used in part.
- Please print this page for your records and send a copy of it to your publisher/graduate school.
- Appropriate credit for the requested material should be given as follows: "Reprinted (adapted) with permission from {COMPLETE REFERENCE CITATION}, Copyright {YEAR} American Chemical Society." Insert appropriate information in place of the capitalized words.
- One-time permission is granted only for the use specified in your RightsLink request. No additional uses are granted (such as derivative works or other editions). For any uses, please submit a new request.

If credit is given to another source for the material you requested from RightsLink, permission must be obtained from that source.

[BACK](#)[CLOSE WINDOW](#)



### Impressively printing patterns of gold and silver nanoparticles

**Author:** Jeffrey N. Anker, Apparao M. Rao, George Chumanov, et al

**Publication:** NANOSELECT

**Publisher:** John Wiley and Sons

**Date:** May 12, 2021

© 2021 The Authors. Nano Select published by Wiley-VCH GmbH

#### Open Access Article

This is an open access article distributed under the terms of the [Creative Commons CC BY](#) license, which permits unrestricted use, distribution, and reproduction in any medium, provided the original work is properly cited.

You are not required to obtain permission to reuse this article.

For an understanding of what is meant by the terms of the Creative Commons License, please refer to [Wiley's Open Access Terms and Conditions](#).

Permission is not required for this type of reuse.

Wiley offers a professional reprint service for high quality reproduction of articles from over 1400 scientific and medical journals. Wiley's reprint service offers:

- Peer reviewed research or reviews
- Tailored collections of articles
- A professional high quality finish
- Glossy journal style color covers
- Company or brand customisation
- Language translations
- Prompt turnaround times and delivery directly to your office, warehouse or congress.

Please contact our Reprints department for a quotation. Email [corporatesaleseurope@wiley.com](mailto:corporatesaleseurope@wiley.com) or [corporatesalesusa@wiley.com](mailto:corporatesalesusa@wiley.com) or [corporatesalesDE@wiley.com](mailto:corporatesalesDE@wiley.com).





## X-ray excited luminescence spectroscopy and imaging with NaGdF<sub>4</sub>:Eu and Tb

M. Ranasinghe, Md. Arifuzzaman, A. C. Rajamanthrilage, W. R. Willoughby, A. Dickey, C. McMillen, J. W. Kolis, M. Bolding and J. N. Anker, *RSC Adv.*, 2021, **11**, 31717 **DOI:** 10.1039/D1RA05451A

This article is licensed under a [Creative Commons Attribution 3.0 Unported Licence](#). **You can use material from this article in other publications without requesting further permissions** from the RSC, provided that the correct acknowledgement is given.

Read more about [how to correctly acknowledge RSC content](#).